



University of  
Massachusetts  
Amherst

## Mid-Pliocene to Early Pleistocene Sea Surface and Land Temperature History of NW Australia Based on Organic Geochemical Proxies from Site U1463

Item Type	thesis
Authors	Smith, Rebecca
DOI	<a href="https://doi.org/10.7275/12417340">10.7275/12417340</a>
Download date	2025-01-31 17:18:33
Link to Item	<a href="https://hdl.handle.net/20.500.14394/33768">https://hdl.handle.net/20.500.14394/33768</a>

**MID-PLIOCENE TO EARLY PLEISTOCENE SEA SURFACE AND LAND  
TEMPERATURE HISTORY OF NW AUSTRALIA BASED ON ORGANIC  
GEOCHEMICAL PROXIES FROM SITE U1463**

A Thesis Presented

by

REBECCA A. SMITH

Submitted to the Graduate School of the  
University of Massachusetts Amherst in partial fulfillment  
of the requirements for the degree of

MASTER OF SCIENCE

September 2018

Department of Geosciences

© Copyright by Rebecca A. Smith 2018

All Rights Reserved

**MID-PLIOCENE TO EARLY PLEISTOCENE SEA SURFACE AND LAND  
TEMPERATURE HISTORY OF NW AUSTRALIA BASED ON ORGANIC  
GEOCHEMICAL PROXIES FROM SITE U1463**

A Thesis Presented

by

REBECCA A. SMITH

Approved as to style and content by:

---

Isla S. Castañeda, Chair

---

Julie Brigham-Grette, Member

---

R. Mark Leckie, Member

---

Julie Brigham-Grette, Department Head  
Department of Geosciences

## **DEDICATION**

To my Mom and Dad, for their unconditional love and support.

## ACKNOWLEDGEMENTS

First, I would like to thank my advisor, Dr. Isla Castañeda. She has become a significant role model in my life as a female scientist and educator, and has motivated me to develop skills in public speaking, scientific writing, and outreach. Her work ethic as a scientist and her dedication as a mentor are phenomenal. Thank you, Isla, for your patience, prompt feedback, and encouragement. Here's to many more years of research and collaboration (hopefully without falling off of any more pigs).

I extend a big thank you to Jeff Salacup, who trained me to work in the Biogeochemistry Lab at UMass during my first semester as a graduate student, who has kept the lab running smoothly, and who has provided useful feedback on my writing and presentations on numerous occasions. Kathryn Turner and Dr. Sivajini Gilchrist assisted with sample preparation and peak integrations, and their help has been critical to the success of this project. Thank you both. This research used samples provided by the International Ocean Discovery Program and was funded by a USSSP grant to Isla S. Castañeda (NSF prime award OCE-1450528).

I would like to thank both members of my Master's Thesis Committee, Dr. Julie Brigham-Grette and Dr. Mark Leckie. I first heard Julie present her research while attending the 2015 American Geophysical Union Fall Conference as an undergraduate at Bates College, and her expertise in paleoclimatology and public speaking helped inspire me to apply to UMass Amherst for graduate school. As head of the department, Julie has done a fantastic job coordinating social events and building community between graduate students and faculty. Despite her busy

schedule, she has taken the time to meet with me to discuss my research, and I hope to someday collaborate with her in order to analyze ocean gateway variability at both high and low latitudes. I had the opportunity to work with Dr. Mark Leckie and his research group in the spring of 2017 to produce a foraminifera reference book that would be later used on an IODP Expedition. With no prior experience looking at forams, Mark and his students patiently helped me to pronounce the names of countless taxa and learn how to distinguish them. I aspire to sail on an IODP cruise in the future, in part due to Mark's enthusiasm for and experience with the program.

I would additionally like to thank Dr. Ray Bradley for teaching me about paleoclimatology when I first arrived to UMass. Ray has explained important skills on how to communicate science to non-scientists, and has provided me with useful feedback on writing that has since been incorporated into this thesis. I also extend a big thank you to Rob DeConto, who has stopped what he was doing countless times to answer my questions and offer new ideas about how I could explore Pliocene climate.

Finally, I would like to thank my fellow graduate students in the department. To Helen, Dan, Benjamin, Boyang, Will, Greg and Thivanka: for showing me the ropes and creating a supportive and collaborative working environment.

To the amazing friends I have made in the department (you know who you are): you have made the past two years an adventure, and I am so blessed and grateful for your friendship.

## ABSTRACT

### **PLIOCENE TO EARLY PLEISTOCENE SEA SURFACE AND LAND TEMPERATURE HISTORY OF NW AUSTRALIA BASED ON ORGANIC GEOCHEMICAL PROXIES FROM SITE U1463**

SEPTEMBER 2018

REBECCA A. SMITH, B.S., BATES COLLEGE

M.S., UNIVERSITY OF MASSACHUSETTS AMHERST

Directed by: Professor Isla S. Castañeda

Ocean gateways facilitate water circulation between ocean basins, and therefore directly impact thermohaline circulation and global climate. In order to better predict the effects of future climate change, it is critical to constrain past changes in ocean gateway behavior, and corresponding changes in thermohaline circulation, particularly during analogue periods for modern climate change. The Indonesian Throughflow (ITF) is a primary ocean gateway and vital component of the global conveyor that transports water from the Pacific Ocean into the Indian Ocean, however due to a lack of long and continuous sedimentary records from locations under its influence, changes in ITF behavior remain poorly constrained. In this study organic geochemical biomarkers preserved in marine sediments are used to reconstruct both sea surface and continental air temperatures in Northwest (NW) Australia from sediments spanning the mid-Pliocene Warm Period (mPWP), a critical carbon dioxide (CO<sub>2</sub>) and temperature analogue period for modern climate change spanning 3.3-3.0 Ma. These sediments were collected during IODP Expedition 356 from Site U1463, located near the outlet of the ITF, and are therefore sensitive to changes in ITF behavior over time. Here, NW Australian air

temperatures were reconstructed from 1.5-3.5 Ma using the MBT'<sub>5ME</sub> proxy (Weijers et al., 2007a; De Jonge et al., 2014a), and offshore sea surface temperatures (SSTs) were reconstructed using both the TEX<sub>86</sub> proxy (Schouten et al., 2002; Tierney & Tingley, 2014) and the Long Chain Diol Index (LDI; Rampen et al., 2012). Global climate events, including Marine Isotope Stages (MIS) 55, 63, 64, 82, 84, 88, 92, G10, G18, G20, G22, and M2 (Lisiecki & Raymo, 2005) are apparent in all of our records. TEX<sub>86</sub> SSTs suggest a stronger cooling signal during MIS Stages G18, G20 and G22 relative to cooling during MIS M2, however LDI SSTs do not yield the same result. Overall, all three proxies indicate higher temperatures across the Pliocene and a cooling trend from ~1.7-1.5 Ma. Cooling occurs during an arid interval identified by Christensen et al. (2017), from 2.4-1.0 Ma, which suggests that offshore cooling contributed to shifts in NW Australian continental hydrology. Cooling from 3.5-1.5 Ma at Site U1463 was likely a reflection of 1) constriction of the ITF from 5-2 Ma and a switch from warm South Pacific to cool North Pacific source waters, and 2) an increase in meridional SST gradients at 1.8 Ma; the particularly strong cooling signal identified in all three records at 1.7 Ma is likely a direct response to the latter. This study helps elucidate ITF variability and shifts in thermohaline circulation across the Plio-Pleistocene and the mPWP, which will help modelers better predict the effects of future climate change.

# TABLE OF CONTENTS

	Page
ACKNOWLEDGEMENTS.....	v
ABSTRACT .....	vii
LIST OF FIGURES.....	xi
CHAPTER	
1. INTRODUCTION.....	1
1.1 Background.....	1
1.1.1 IODP Expedition 356.....	1
1.1.2 The ITF and the Plio-Pleistocene.....	1
1.1.3 Indian Ocean Surface and Subsurface Temperature Records.....	3
1.1.4 Pacific Ocean SSTs and Plio-Pleistocene SST Gradients.....	4
1.2 Research Objectives and Hypotheses .....	6
1.3 Biomarker Background.....	9
1.3.1 UK <sub>37</sub> SST Proxy.....	9
1.3.2 LDI SST Proxy .....	12
1.3.3 TEX <sub>86</sub> Surface/Subsurface Temperature Proxy.....	15
1.3.4 MBT <sub>5ME</sub> Mean Annual Air Temperature Proxy .....	20
2. METHODS.....	36
2.1 Sample Preparation.....	36
2.2 Alkenones .....	36
2.3 Long Chain Diols.....	37
2.4 Isoprenoid and Branched GDGTs.....	37
3. RESULTS .....	40
3.1 Alkenone Data .....	40
3.2 LDI Data.....	40
3.3 Isoprenoid GDGT Data.....	41
3.4 Branched GDGT Data .....	42
4. DISCUSSION .....	51

4.1 SST Proxy Comparison.....	51
4.2 Site U1463 vs. Nearby Sites .....	56
4.2.1 Indian Ocean Records .....	57
4.2.2 Pacific Ocean Records.....	58
4.3 Zonal and Meridional SST Gradients.....	58
4.4 Central American Seaway and Bering Strait Variability .....	60
4.5 Site U1463 vs. Global SST Records.....	63
4.5.1 Cooling at 1.7 Ma.....	63
4.5.2 MIS M2 and Pronounced Cooling During MIS G18, G20 and G22 .....	67
4.6 Continental Air Temperatures and Offshore Cooling.....	70
5. CONCLUSIONS AND FUTURE WORK.....	85
5.1 Summary of Interpretations.....	85
5.2 Extending the SST Record .....	86
5.3 Core-Top TEX <sub>86</sub> Calibration.....	87
5.4 Leaf Wax Isotope and Time Series Analysis .....	87
BIBLIOGRAPHY .....	88

## LIST OF FIGURES

Figure	Page
1.1 Drilling Sites U1458-U1464 of IODP Expedition 356 across NW Australia.....	24
1.2 Site U1463 analyzed in this study (black star), as well as Sites 763A, 214, and 806.....	25
1.3 Depth (meters) of islands within the ITF constituting what is referred to as the Maritime Continent.....	26
1.4 Geochemical records from Indian Ocean Sites ODP 214 and ODP 763A.....	27
1.5 The SST record from Site 806 (Wara et al., 2005).....	28
1.6 Global map of relevant SST records.....	29
1.7 The modeled extent of the equatorial warm pool in the Pliocene versus the Modern (edited from Brierley and Fedorov, 2010).....	30
1.8 Age vs. %K (Christensen et al., 2017) and $\delta^{18}O$ (Lisiecki and Raymo, 2005).....	31
1.9 Illustration of evolution of NW Australian hydrology from 7 Ma to the modern (Christensen et al., 2017).....	32
1.10 Structural changes in long chain alkenones associated with shifts in water temperature.....	33
1.11 Isoprenoid GDGT structures.....	34
1.12 Branched GDGT structures.....	35
3.1 The ratio of $C_{37}$ to $C_{38}$ LCAs measured at Site U1463 versus Age from 3.5-1.5 Ma.....	45
3.2 Fractional abundance of each long chain diol (%), averaged across the entire study interval from 3.5-1.5 Ma.....	45
3.3 Fractional abundance, reported in % of total long chain diol concentration, of each long chain diol plotted versus core depth in meters core composite depth below seafloor (m CCFS-A).....	46
3.4 Temperature records with calibration error from Site U1463 vs. Age from 3.5-1.5 Ma.....	47

3.5	Temperature records without calibration error from Site U1463 vs. Age from 3.5-1.5 Ma.....	48
3.6	Concentrations in ug/g sediment of brGDGTs (orange) and iGDGTs (blue) from Site U1463 vs. Age from 3.5-1.5 Ma.....	49
3.7	Average concentration in ug/g sediment of brGDGTs group 1-3 from 3.5-1.5 Ma.....	49
3.8	The #rings <sub>tetra</sub> index vs. Age from 3.5-1.5 Ma .....	50
3.9	BIT index values, plotted from 0-1, vs. Age from 3.5-1.5 (Ma).....	50
4.1	Modern Indo-Pacific SST map .....	73
4.2	Modern SSTs (red) relative to Site U1463 LDI (dark blue) and TEX <sub>86</sub> SST and subT paleodata (light blue and orange, respectively). .....	73
4.3	LDI SSTs (°C) versus the LR04 global benthic δ <sup>18</sup> O stack from a) 2.5-1.5 Ma and b) 3.5-2.5 Ma.....	74
4.4	TEX <sub>86</sub> SSTs (°C) versus the LR04 global benthic δ <sup>18</sup> O stack from a) 2.5-1.5 Ma and b) 3.5-2.5 Ma.....	75
4.5	Cross-plot of LDI SSTs (°C) versus BAYSPAR TEX <sub>86</sub> SSTs (°C). .....	76
4.6	% fractional abundance of the C <sub>30</sub> 1,15 diol (blue) and LDI-SST (°C)(black) from 3.5-1.5 Ma.....	76
4.7	Summary of ITF SST records .....	77
4.8	Comparison of ITF inflow and outflow SST records.....	78
4.9	Zonal SST gradients from Site U1463 to Site 806.....	79
4.10	Meridional SST gradients from Site U1463 to Site 722 .....	80
4.11	Global SST comparison from 3.5-1.5 Ma.....	81
4.12	Cross-plot of MBT' <sub>5ME</sub> MAATs (°C) vs. BAYSPAR TEX <sub>86</sub> SSTs (°C) .....	82
4.13	Cross-plot of MBT' <sub>5ME</sub> MAATs (°C) vs. LDI SSTs (°C).....	82
4.14	MBT' <sub>5ME</sub> (°C) versus the LR04 global benthic δ <sup>18</sup> O stack from a) 2.5-1.5 Ma and b) 3.5-2.5 Ma.....	83

4.15	Continental air temperature and humidity reconstructions from Site U1463 from 3.5-1.5 Ma.....	84
------	--------------------------------------------------------------------------------------------------	----

## **CHAPTER 1**

### **INTRODUCTION**

#### **1.1 Background**

##### **1.1.1 IODP Expedition 356**

In summer 2015, IODP Expedition 356 collected sediment cores from six borehole locations (U1459-U1464; Figure 1.1) across the coast of northwest (NW) Australia (Gallagher et al., 2017). Two main objectives of this expedition were to a) reconstruct NW Australian continental aridity, and b) constrain Indonesian Throughflow (ITF), Western Pacific Warm Pool (WPWP), and Leeuwin Current (LC) (Figure 1.2) variability from the late Miocene to the early Pleistocene (Gallagher et al., 2014). In order to address these objectives and determine the effects of ITF variability on Plio-Pleistocene climate (3.5-1.5 Ma), the purpose of this project is to reconstruct the land and sea surface temperature history of NW Australia using multiple organic geochemical proxies of sediments from Site U1463 (18°58'S, 117°37'E; Figures 1.1, 1.2, 1.6).

##### **1.1.2 The ITF and the Plio-Pleistocene**

The Pliocene-Pleistocene time interval encompasses the mid-Pliocene Warm Period (mPWP), which occurred approximately 3.33-3.00 Ma. This interval is characterized by slightly higher global temperatures ( $\sim 3^{\circ}\text{C}$ ) and  $\text{CO}_2$  concentrations similar to modern values (Dowsett et al., 1992; Raymo et al., 1996; Hönisch et al., 2009; Dowsett et al., 2009; Pagani et al., 2010; Bartoli et al., 2011); and therefore provides an analog for modern conditions. Research on climate forcing across the

mPWP could provide crucial data to improve models and responses to future climate change.

The ITF is a critical ocean gateway involved in global thermohaline circulation and the global conveyor, however a limited number of studies have measured the influence of ITF variability on climate during the mPWP and the Pliocene overall (Cane & Molnar, 2001; Karas et al., 2009; Karas et al., 2011a; Karas et al., 2011b). IODP Site U1463 is uniquely sensitive to changes in ITF behavior because it is located close to the ITF outlet (Figure 1.2). From 5-2 Ma, New Guinea and Australia shifted 2-3° north, which caused gradual shoaling and constriction of the ITF (Cane & Molnar, 2001). In turn, shoaling caused the emergence of the Maritime Continent, i.e. the modern islands located within the ITF (Molnar & Cronin, 2015). Prior to constriction from 5-2 Ma, Cane and Molnar (2001) hypothesize that warm, saline South Pacific waters fed ITF currents into the Indian Ocean. The onset of both constriction and shoaling introduced Halmahera Island as a significant land barrier at the opening of the ITF (Figure 1.3), which later grew in surface area due to volcanic activity (Cane & Molnar, 2001). Cane and Molnar (2001) argue that Halmahera eventually blocked South Pacific warm water from entering the ITF, and caused a shift from South Pacific to North Pacific ITF source waters (Morey et al., 1999). In 2006, Martin and Scher (2006) tested this hypothesis by analyzing sediments from ODP Site 757 (eastern Indian Ocean; Figure 1.6) for Nd isotopes ( $\epsilon_{Nd}$ ). Nd is a radiogenic isotope that weathers from continental crust into ocean water, and different water masses reflect different  $\epsilon_{Nd}$  values (Frank, 2002). Martin and Scher (2006) documented an increase in  $\epsilon_{Nd}$  values from 3.4-1 Ma at Site

757, which they suggest could be a reflection of a shift in source waters from the South Pacific (less radiogenic) to the North Pacific (more radiogenic)(Martin & Scher, 2006; references therein). Modern ocean circulation studies indicate that most South Pacific waters are diverted from entering the ITF via the Halmahera Eddy (HE; Figure 1.2a), and North Pacific cold water dominates the ITF (Gordon & Fine, 1996; Gordon et al., 1999; Gordon, 2005).

### **1.1.3 Indian Ocean Surface and Subsurface Temperature Records**

Sea surface temperature (SST) reconstructions at two different locations in the Indian Ocean were conducted in 2009 (DSDP Site 214) and in 2011 (ODP Site 763A; Figure 1.2 & 1.6), in order to further test the hypotheses posed by Cane and Molnar (Karas et al., 2009; Karas et al., 2011a). Karas et al. (2009) conducted chemical analyses on sediment samples from Site 214 (Figure 1.2 and 1.6), cored during the Deep Sea Drilling Project in 1972. The authors measured oxygen isotopes ( $\delta^{18}\text{O}$ ) and magnesium to calcium (Mg/Ca) ratios of the surface dwelling foraminifera species *Globigerinoides ruber* and *Globigerinoides sacculifer*, as well as the deeper dwelling species *Globoconella crassaformis* to produce upper water column temperature reconstructions from 5.5-2.0 Ma (Figure 1.4).  $\text{SST}_{\text{Mg/Ca}}$  of *G. ruber* and *G. sacculifer* across this interval indicate relatively stable temperatures from 24-26.5°C. However, results from *G. crassaformis* indicate a 4°C temperature decrease in subsurface water temperatures from 3.5-2.95 Ma (Figure 1.4). The authors suggest that this cooling trend supports the hypothesis proposed by Cane and Molnar (2001), except that cooling occurred at depth rather than at the surface, likely due to cooling of subsurface rather than surface ITF source waters at the time.

Subsequently, Karas et al. (2011a) reconstructed SST<sub>Mg/Ca</sub> using *G. sacculifer* from ODP Site 763A (Figure 1.4), which was cored during the Exmouth Plateau ODP Expedition in August 1988. Site 763A sits closer to the outlet of the ITF than the previously studied Site 214 (Figure 1.2, 1.6); however, it is still located a considerable distance from the ITF relative to Site U1463. Karas et al. (2011a) identify that while surface temperatures at Site 214 did not change significantly across the 3.5-2.95 Ma interval, SSTs at Site 763A cooled by 2-3°C near 3.3 Ma (Figure 1.4). In order to explain surface cooling at Site 763A and not at Site 214, the authors suggest that constriction of the ITF caused slowing and subsequent cooling of Leeuwin Current surface waters traveling across the west coast of Australia. However, given that to date only these two studies (Karas et al., 2009; 2011a) have reconstructed ITF SST variability across the Plio-Pleistocene, numerous outstanding questions exist regarding variability in ITF strength, position, and history.

#### **1.1.4 Pacific Ocean SSTs and Plio-Pleistocene SST Gradients**

In addition to Indian Ocean records, Pacific SST records spanning the Plio-Pleistocene can help to elucidate shifts in ITF behavior over time. ODP Site 806 (Figure 1.5, 1.6) is located in the western equatorial Pacific (WEP) and is in close proximity to both the Halmahera Eddy (HE) and the entrance to the ITF. For this reason, Site 806 is sensitive to shifts in ocean currents entering the ITF over time. Wara et al. (2005) reconstructed SSTs at Site 806 by measuring Mg/Ca ratios of *G. sacculifer* (Figure 1.5). From ~3.5-2.5 Ma, SSTs at Site 806 decreased by ~2°C, followed by a distinct warming trend near 1.7 Ma (Wara et al., 2005). The warming signal seems to occur after the constriction and shoaling of the ITF ended ~2 Ma,

which suggests that Site 806 received more South Pacific warm waters returning from the entrance of the ITF via the HE (Figure 1.2a) post constriction.

Wara et al. (2005) also reconstructed temperatures in the eastern equatorial Pacific at ODP Site 847 (Figure 1.6) in order to produce a Plio-Pleistocene equatorial west-to-east SST gradient relative to Site 806. Modern equatorial SST gradients can drive shifts in Walker circulation (Wara et al., 2005), and therefore reconstructing these gradients can provide critical insight into ocean-atmosphere dynamics across the Plio-Pleistocene. The equatorial Pacific zonal SST difference between Site 806 and 847 is relatively low from 5.3-1.7 Ma across the mPWP. At 1.7 Ma, Wara et al. (2015) identify an increase in zonal SST difference between these sites, corresponding to a cooling SST signal at Site 847. The authors suggest that this divergence in SSTs marks the initiation of a steep equatorial Pacific SST gradient that previously did not exist during the mPWP. The modern SST gradient between Site 806 and Site 847 is significantly higher at  $\sim 7^{\circ}\text{C}$  than it was during the mPWP at  $\sim 4^{\circ}\text{C}$ .

Brierley et al. (2009) produced a north-to-south meridional SST gradient across the Pacific Ocean from 4 Ma to present by comparing alkenone-based SST measurements from ODP Site 846 (located in the EEP, Figure 1.6) and ODP Site 1012 (located near the California Margin; Figure 1.6). Their results indicate that prior to 2 Ma, the meridional SST gradient was relatively low at  $\sim 2^{\circ}\text{C}$  (Brierley et al., 2009). At  $\sim 2$  Ma, surface temperatures at Site 1012 began to cool more rapidly than those at Site 846, causing a net increase in the meridional SST gradient by  $\sim 7^{\circ}\text{C}$ . This significant meridional SST gradient increase at  $\sim 2$  Ma slightly preceded the

zonal west-to-east equatorial Pacific SST gradient increase at 1.7 Ma. The authors suggest from these results that variations in the meridional SST gradient at 2.0 Ma drove the shift in zonal equatorial SST gradient at 1.7 Ma.

Today, higher meridional and zonal SST gradients confine warm waters to the equator. During the Pliocene, particularly across the mPWP, SSTs were higher at higher latitudes and warm ocean temperatures extended across most of the tropics (Brierley et al., 2009; Brierley & Fedorov, 2010)(Figure 1.7). The progressive drop in the extent of tropical water, hereafter referred to as the tropical warm pool, since the Pliocene may have influenced outflowing ITF SSTs in the Indian Ocean at Site U1463. Therefore, in addition to the tectonic constriction of the ITF from 5-2 Ma (Cane & Molnar, 2001), zonal and meridional SSTs must be analyzed as possible forcing mechanisms that could have influenced SSTs at Site U1463 from 3.5-1.5 Ma.

## **1.2 Research Objectives and Hypotheses**

The hypotheses proposed by Cane and Molnar (2001), Karas et al. (2009), and Karas et al. (2011a) to explain sea surface temperature variability across the ITF rely on limited studies from sediment cores extracted before 1990. Cane and Molnar's hypothesis, that tectonic constriction of the ITF caused a switch in ITF source waters from 5-2 Ma, was first tested by Martin and Scher (2006) using Nd isotopes; however, a thorough, multi-proxy record from a continuous sediment core located close to the outlet of the ITF is required to fully elucidate ITF variability across the Plio-Pleistocene. Furthermore, the role of meridional and zonal SST gradients in both the Indian and Pacific Ocean must be considered as forcing mechanisms influencing SSTs near the ITF.

Since IODP Expedition 356 in 2015, Christensen et al. (2017) have analyzed shipboard Natural Gamma Ray (NGR) data of sediments from Site U1463 and identified a humid (5.5-3.3 Ma), transition (3.3-2.4 Ma), and arid interval (2.4- less than 1 Ma) in NW Australia (Figure 1.8). The authors attribute these shifts in aridity to the constriction and shoaling of the ITF, which they depicted in a useful step-wise illustration (Figure 1.9). Due to the strong correlation between near-shore aridity and sea surface temperatures (SSTs) in Australia (King et al., 2015; Christensen et al., 2017), it is critical to compare the aridity intervals identified by Christensen et al. (2017) to changes in SSTs at Site U1463.

This project reconstructs SSTs from sediments at Site U1463 spanning 3.5-1.5 Ma using organic geochemical proxies including the alkenone unsaturation index,  $U^{K}_{37}$  (Prahl & Wakeham, 1987), the long-chain diol index, LDI (Rampen et al., 2012), and the tetraether index of 86 carbon atoms,  $TEX_{86}$  (Schouten et al., 2002). Furthermore, results are compared to SSTs from Indian Ocean sites 214 (Karas et al., 2009) and 763 (Karas et al., 2011a), as well as to hydrologic intervals identified by Christensen et al. (2017). SST data are also used to produce a zonal (west to east) SST gradient from Site U1463 to Site 806, as well as a meridional (south to north) SST gradient from Site U1463 to northern Site 722 (Herbert et al., 2010)(Figure 1.6). Continental mean annual air temperatures in NW Australia are determined by *a)* applying the  $MBT'_{5ME}$  mean annual air temperature proxy based on branched glycerol dialkyl glycerol tetraethers (brGDGTs) to sediments at Site U1463, and by *b)* applying a new proxy, the  $\#rings_{tetra}$  index (Sinninghe Damsté, 2016), to determine marine versus terrestrial origin of brGDGTs at Site U1463.

Hypotheses for this project are as follows:

- [1] SST reconstructions from  $U^{K'_{37}}$ , LDI, and  $TEX_{86}$  will reflect surface cooling in agreement with results from Karas et al. (2011a).
- [2] The zonal SST gradient from Site U1463 to Site 806 (Wara et al., 2005) will reflect an increase in SST difference between the two sites from the Pliocene into the Pleistocene.
- [3] The meridional SST gradient from Site U1463 to Site 722 (Herbert et al., 2010) will reflect a constriction of the tropical warm pool in the Indian Ocean from the Pliocene into the Pleistocene.
- [4] Results from the  $\#rings_{tetra}$  index will reflect that brGDGTs measured at Site U1463 formed in continental soils and were transported by wind (or rivers in the past when conditions were wetter than today).
- [5]  $MBT'_{5ME}$  measurements will mirror SST trends, and indicate a strong relationship between SSTs and nearby continental air temperatures.
- [6] Cooling in both the terrestrial and marine records will coincide with the arid interval from 2.4 to less than 1 Ma (Christensen et al., 2017), as cooler sea surface temperatures decrease moisture availability onshore.
- [7] SST and MAAT temperature records will correspond to LR04 glacial/interglacial cycles.

SST records from the  $U^{K'_{37}}$ , LDI, and  $TEX_{86}$  proxies will inform Hypotheses [1], [2], [3], [6], and [7]. The  $\#rings_{tetra}$  proxy data will inform Hypothesis [4], and a

continental air temperature record using  $MBT'_{5ME}$  will inform Hypotheses [5], [6], and [7].

### **1.3 Biomarker Background**

At various depths throughout the water column, organisms from the three domains of life (archaea, eukarya, and bacteria) biosynthesize organic matter to produce lipids (Peters et al., 2005). Once a source organism dies and descends to the ocean floor, the remaining organic matter that eventually gets preserved in marine sediment is considered an organic biomarker (Castañeda & Schouten, 2011).

Organisms adjust the structure of their lipid membranes in response to surrounding growth temperature; therefore, the chemical composition of biomarkers varies depending on the climatic conditions (temperature, salinity, pH) of the surrounding environment when the biomarker was produced (Castañeda & Schouten, 2011). The biomarker composition preserved upon burial can be extracted and analyzed in order to reconstruct the environmental conditions that existed during the lifespan of the source organism. In addition to marine sediments, biomarkers are also preserved in continental soils, rocks, petroleum deposits, and coal deposits (Castañeda & Schouten, 2011). The  $U^k_{37}$ ,  $TEX_{86}$ , and LDI temperature proxies applied in this study measure the ratios of different lipid compounds produced by biomarkers preserved in marine sediments, and the  $MBT'_{5ME}$  proxy measures the compounds preserved in NW Australian continental soils from 3.5-1.5 Ma.

#### **1.3.1 $U^k_{37}$ SST Proxy**

The  $U^k_{37}$  Index is based on unsaturation ratios of long-chain alkenones with 37 carbon atoms produced in the open ocean by photosynthetic haptophyte algae

*Emiliani huxleyi* and *Gephyrocapsa oceanica* (de Leeuw et al., 1980; Volkman et al., 1980a; Volkman et al., 1980b; Volkman et al., 1995; Herbert, 2006). Studies indicate that *E. huxleyi* evolved by ~0.27 Ma (Thierstein et al., 1977), and *G. oceanica* evolved by ~1.93 Ma; therefore, most sediments in this study spanning 3.5-1.5 Ma predate the presence of these species. Despite the younger emergence of *E. huxleyi* and *G. oceanica* in the geologic record, the  $U_{37}^k$  index has been applied in previous studies to reconstruct Pliocene temperatures, under the assumption that previously evolved alkenone-producing species had similar relationships with SST (Herbert & Schuffert, 1998). Therefore, in this study we also assume that the modern calibration for  $U_{37}^k$  applies to Plio-Pleistocene sediments from Site U1463.

Long chain alkenones consist of 37 and 39 carbon atoms ( $C_{37}$ - $C_{39}$ ), and are made up of di-, tri-, and tetra- unsaturated methyl and ethyl ketones (Figure 1.10a) (Volkman et al., 1980a; Volkman et al., 1980b; Castañeda & Schouten, 2011). The relative amount of tri-unsaturated ketones within a long chain alkenone increases with decreasing temperature (Figure 1.10b-c) (de Leeuw et al., 1980; Volkman et al., 1980a; Volkman et al., 1980b; Brassell et al., 1986). The original  $U_{37}^k$  index (Brassell et al. 1986) included the di- ( $C_{37:2}$ ), tri- ( $C_{37:3}$ ), and tetra- ( $C_{37:4}$ ) unsaturated alkenones. It was later found that inclusion of the  $C_{37:4}$  alkenone did not improve the calibration's relationship with SST and was absent or in very low abundances at many sites. Prahl and Wakeham (1987) grew haptophyte algae species *Emiliani huxleyi* in lab cultures between 5-25°C and tested the effects of temperature on the presence of  $C_{37:4}$  ketones. They calculated the same values of  $U_{37}^k$  and  $U_{37}^{k'}$  at temperatures above 15°C. Therefore, the  $C_{37:4}$  unsaturated ketones exist only in

water temperatures below 15°C, would not exist in tropical sea surface waters at Site U1463, and can be excluded from the  $U_{37}^{k'}$  calibration equation altogether (Prahla & Wakeham, 1987; Equation 1).

$$U_{37}^{K'} = [C_{37:2}]/[C_{37:2} + C_{37:3}] \quad (1)$$

As shown in Figure 1.10b-c, concentrations of  $C_{37:3}$  decrease and  $U_{37}^{k'}$  ratios approach 1 as temperatures increase. The uppermost temperature limit of the  $U_{37}^{k'}$  SST proxy is ~29°C (Pelejero & Calvo, 2003), depending on the calibration applied, where the tri-unsaturated alkenone peak becomes too small to quantify or is absent. The Muller et al. (1998) calibration (Equation 2) is applied to reconstruct SST from  $U_{37}^{k'}$  measurements at Site U1463, and has a calibration error of  $\pm 1.5^\circ\text{C}$  (Müller et al., 1998).

$$U_{37}^{K'} = 0.033 \times \text{SST} + 0.044 \quad (2)$$

In addition to serving as a SST proxy, alkenone ratios and concentrations also provide other environmental information. The ratio of long chain alkenones with 37 versus 38 carbon atoms ( $C_{37}/C_{38}$ ) can be used to assess if alkenones are produced in the open ocean or if there is an influence from coastal species (which have a different relationship between the unsaturation index and SST). Long chain alkenones produced in open ocean environments by *Emiliani huxleyi* and *Gephyrocapsa oceanica* (de Leeuw et al., 1980; Volkman et al., 1980a; Volkman et al.,

1980b; Castañeda & Schouten, 2011) have average C<sub>37</sub>/C<sub>38</sub> ratios between 0.7-1.7 (Prah & Wakeham, 1987), whereas coastal species generally are characterized by higher C<sub>37</sub>/C<sub>38</sub> ratios. As haptophyte algae are one of the main primary producers in the world's oceans, alkenone concentrations or mass accumulation rates in marine sediments can serve as a proxy for past productivity (Prah & Muehlhausen, 1989; Brassell, 1993). Previous research has suggested that major changes in primary productivity, related to strengthening of the westerlies and increased upwelling, occurred during the Plio-Pleistocene (Lawrence et al., 2013).

### 1.3.2 LDI SST Proxy

The Long-Chain Diol Index (LDI) is the most recently developed SST proxy to date (Rampen et al., 2012), and has been only scarcely applied to Pliocene ocean sediments (Naafs et al., 2012). Naafs et al. (2012) applied LDI to 14 samples spanning 2.41-2.49 Ma from the North Atlantic, however this research project will be the first to apply this new proxy to sediments as old as 3.5 Ma. LDI was developed by Rampen et al. (2012) to reconstruct SSTs between -3 and 27°C, and measures the ratio of C<sub>30</sub>1,15 *n*-alkyl-diol, C<sub>28</sub>1,13 *n*-alkyl-diol and C<sub>30</sub>1-13 *n*-alkyl-diol (Equation 3).

$$\text{LDI} = \frac{F_{\text{C}_{30}1,15\text{-diol}}}{F_{\text{C}_{28}1,13\text{-diol}} + F_{\text{C}_{30}1,13\text{-diol}} + F_{\text{C}_{30}1,15\text{-diol}}} \quad (3)$$

Where 'F' indicates fractional abundance of each *n*-alkyl diol. These diols are differentiated by the number of carbon atoms comprising their alkyl chain (C<sub>30</sub> or C<sub>28</sub>) and by the position of alcohol groups along their alkyl chain, at sites 1 and 13 or

sites 1 and 15 (Rampen et al., 2012). These diols are likely synthesized by phototrophic species of diatoms and microalgae (Rampen et al., 2012), which dwell in the photic zone of the ocean and thereby must capture a SST signal. There is a strong correlation between LDI and SST ( $r^2 = 0.969$ ; Equation 4), and the proxy has a calibration error of  $\pm 2^\circ\text{C}$  (Rampen et al., 2012). Rampen et al. (2012) applied the LDI proxy to Holocene sediments from the South Atlantic to compare it to  $U_{37}^{k'}$  sea surface temperatures from the same core. They measured a 1-2 $^\circ\text{C}$  difference between the two proxies, which they deem insignificant relative to calibration errors.

$$\text{LDI} = 0.033 \times \text{SST} + 0.095, r^2 = 0.969 \quad (4)$$

Small differences discussed by Rampen et al. (2012) between the LDI and  $U_{37}^{k'}$  temperature reconstructions encourage more comparisons in future studies. If possible, it would be useful to compare SSTs from both of these proxies at Site U1463.

The LDI was applied to marine sediments spanning the past 135,000 years collected off the coast of southeast Australia from AUSCAN 2003 core MD03-2607 ( $36^\circ 57.64'\text{S}$ ,  $137^\circ 24.39'\text{E}$ ; Lopes dos Santos et al., 2013)(Figure 1.6). The authors compared their LDI record to their  $U_{37}^{k'}$  and  $\text{TEX}^{\text{H}_{86}}$  SST records measured on the same samples, and found an overall agreement in SST trends across the time interval. While comparable in overall trends, they did observe that LDI temperatures were higher than both  $U_{37}^{k'}$  and  $\text{TEX}^{\text{H}_{86}}$  SSTs during glacial periods.

The authors suggest that part of the temperature offset between proxy records could be due to calibration errors (Lopes dos Santos et al., 2013), however other variables must be considered to explain the more significant differences in temperature between proxies. They provide several factors that could contribute to differences in their records, and these factors include: 1) possible input of soil organic matter from nearby rivers, which could affect TEX<sup>H</sup><sub>86</sub> values, 2) lateral transport and selective degradation, which must be considered if there are significant differences in overall trends between proxies, 3) light and nutrient limitation (Epstein et al., 2010; Prahl et al., 2005; Sikes et al., 2005), 4) water depth in which the source organism lived, and 5) preferred growing season of the source organism. It is important to consider each of these variables relative to the multi-proxy records from this study at Site U1463.

In addition to measuring the ratio of C<sub>30</sub>1,15, C<sub>28</sub>1,13 and C<sub>30</sub>1,13 *n*-alkyl-diols for the LDI (Equation 3), the C<sub>32</sub> 1,15-diol can be utilized as a proxy for river input to marine settings because studies suggest that this diol is produced by freshwater dwelling eustigmatophyte algae (Lattaud et al., 2017). The total concentration of C<sub>32</sub> 1,15-diols will be calculated in sediments from Site U1463 spanning 3.5-1.5 Ma, in order to determine the relative input of freshwater from rivers to Site U1463 across this interval. It is important to note that a high relative input of freshwater from rivers could influence the applicability of LDI at Site U1463, because C<sub>30</sub>1,15, C<sub>28</sub>1,13 and C<sub>30</sub>1-13 *n*-alkyl-diols measured at Site U1463 could originate from either a freshwater or marine source (Lattaud et al., 2017).

### 1.3.3 TEX<sub>86</sub> Surface/Subsurface Temperature Proxy

The TetraEther indeX with 86 carbons (TEX<sub>86</sub>) is a water temperature proxy based on isoprenoidal GDGTs. These compounds are formed by mesophilic archaea, the Thaumarchaeota (Schouten et al., 2000; Brochier-Armanet et al., 2008), and are made up of isoprenoid structures with glycerol alkyl groups bonded to either end of the compound (Castañeda & Schouten, 2011)(Figure 1.11). Within a given iGDGT resides between 0 to 4 cyclopentane rings (Castañeda & Schouten, 2011). Compounds with 4 cyclopentane moieties contain a cyclohexane ring indicative of 'crenarchaeol', a compound that is uniquely produced by Thaumarchaeota and not other types of archaea (Sinninghe Damsté et al., 2002; Schouten et al., 2002).

Before they were identified as a separate phylum altogether, Thaumarchaeota were originally considered Group I Crenarchaeota (Brochier-Armanet et al., 2008; Spang et al., 2010; Hurley et al., 2016). Karner et al. (2001) detected marine crenarchaeota across a large range of depths, from the mesopelagic through the bathypelagic (approximately 200-1000m in depth), indicating that these species can flourish across a large range of temperatures and therefore must utilize some sort of biologic mechanism to adapt to different environments. Previous phylogenetic research suggested that all Crenarchaeota were thermophilic, meaning that all were high temperature extremophiles (Hershberger et al., 1996; Schouten et al., 2002). However, Brochier-Armanet et al. (2008) compared certain phylogenetic-marker proteins in the mesophilic archaea species *Cenarchaeum symbosium* to marker proteins in both Crenarchaeota and Euryarchaeota, and determined that the mesophilic archaea are unique in protein composition relative

to the two other phyla. These mesophilic archaea were categorized as a new phylum entitled Thaumarchaeota (Brochier-Armanet et al., 2008), which are abundant across the globe and contain membrane-forming isoprenoid GDGTs (Schouten et al., 2000). Thaumarchaeota are ammonia-oxidizing Archaea (AOA), meaning they oxidize ammonia or ammonium into nitrite, thereby facilitating the first step of nitrification (Könneke et al., 2005; Beman et al., 2008; Newell et al., 2013; Hurley et al., 2016). As AOAs, Thaumarchaeota can utilize ammonia to grow at depths with limited sunlight and organic energy sources (Könneke et al., 2005); therefore, Thaumarchaeota are not limited to the photic zone to survive, and isoprenoid GDGTs preserved in sediments at Site U1463 could originate from surface or subsurface water depths. In fact, Thaumarchaeota have been previously identified in epipelagic, mesopelagic and bathypelagic ocean depths (Karner et al., 2001; Beman et al., 2008; Tolar et al., 2013). Unlike LDI and  $U_{37}^{k'}$ ,  $TEX_{86}$  cannot be considered strictly as a SST proxy.

Schouten et al. (2002) calibrated the  $TEX_{86}$  SST proxy after measuring a significant difference in iGDGT composition between cold and warm ocean sediments sampled across the globe. In cold Antarctic sediments from Halley Bay Station, the authors measured crenarchaeol and trace concentrations of GDGT 0 and GDGT 1, whereas in warm sediments from the Arabian Sea, the authors measured higher concentrations of GDGTs 0-4. Their results confirmed previous observations that the number of cyclopentane rings increases when temperature increases (Uda et al., 2001; Schouten et al., 2002). The authors conducted linear correlations between local SST records collected from the World Ocean Atlas (1998) and ratios

of isoprenoid GDGT concentrations from their samples to produce the first TEX<sub>86</sub> calibration (Equation 5). Their calibration yielded TEX<sub>86</sub> values with high correlations to SST ( $r^2=0.92$ ) (Equation 6).

$$\text{TEX}_{86} = \frac{[\text{GDGT-2}]+[\text{GDGT-3}]+[\text{GDGT-4 cren}]}{[\text{GDGT-1}]+[\text{GDGT-2}]+[\text{GDGT-3}]+[\text{GDGT-4}]} \quad (5)$$

$$\text{TEX}_{86} = 0.015T + 0.28, r^2 = 0.92 \quad (6)$$

As the TEX<sub>86</sub> SST proxy has been further developed and more samples added to the global calibration dataset, additional temperature calibrations have been proposed (e.g. Kim et al., 2008; Kim et al., 2010). One of the more recent calibrations, BAYSPAR, is a Bayesian, spatially-varying calibration model (Tierney & Tingley, 2014; Tierney and Tingley, 2015). This model accounts for slight deviations from the overall SST-TEX<sub>86</sub> and SubT-TEX<sub>86</sub> correlations at a given field location, in order to improve accuracy of TEX<sub>86</sub> reconstructions by study site (Tierney & Tingley, 2014). This approach works well in areas where there is a sufficient amount of modern surface sediment data and is generally the preferred calibration used by the TEX<sub>86</sub> scientific community. Therefore, the BAYSPAR TEX<sub>86</sub> calibration causes slight changes in Equation 6 depending on the geographic region from which samples originate.

Huguet et al. (2007) applied TEX<sub>86</sub> to samples collected from sediment traps suspended at 490m water depth in Santa Barbara Basin, CA, and measured temperatures significantly lower than modern SST values for the region. The

authors argue that these low TEX<sub>86</sub> temperatures indicate that iGDGTs were produced at subsurface depths, likely between 100-150m (Huguet et al., 2007), rather than at surface depths. Huguet et al. (2007) also identify several iGDGT fluxes in their record, which they suggest correspond to increased seasonal upwelling and El Niño Southern Oscillations (ENSO; Thunell et al., 1999). In 2008, Lee et al. measured TEX<sub>86</sub> of surface waters, subsurface waters, and core top sediments collected off the coast of western South Africa, which is a strong coastal upwelling region. Their results indicate that satellite-based SST values in the region are higher than TEX<sub>86</sub>-based temperature values from core-top and surface water samples (Lee et al., 2008). Similar to Huguet et al. (2007), the authors suggest from these results that iGDGTs formed in the subsurface ocean layer and moved to surface waters via regional upwelling.

Conversely, Wutcher et al. (2006) applied TEX<sub>86</sub> to samples collected from sediment traps in the northeastern Pacific Ocean and the Arabian Sea, and their results yielded comparable temperatures to SST satellite measurements. The authors in this study conclude that Thaumarchaeota must have been growing in surface waters, rather than in mesopelagic or bathypelagic settings (Wuchter et al., 2006). Lee et al. (2008) measured TEX<sub>86</sub> of surface waters, subsurface waters, and core top sediments collected off the coast of western South Africa, which is a strong coastal upwelling region. Their results indicate that TEX<sub>86</sub>-based SSTs from core-top and surface water samples were lower than satellite-based SST values in the region (Lee et al., 2008). Similar to Huguet et al. (2007), the authors suggest that iGDGTs form in the subsurface and are transported to surface waters via regional upwelling.

Without conducting sediment trap analyses, it will be difficult to discern whether iGDGT compounds from Site U1463 originate in the subsurface or surface layer. Direct comparison between BAYSPAR TEX<sub>86</sub> and the strictly photic zone temperature proxy LDI will hopefully elucidate the water depth in which iGDGTs formed at Site U1463.

Finally, studies have identified iGDGT compounds (II-IV and region-isomer of crenarchaeol VI') in small concentrations in soil and peat bog samples (Gattinger et al., 2003; Weijers et al., 2004; Weijers et al., 2006). Therefore, if any soil-based iGDGT compounds are present in sediments from Site U1463, the TEX<sub>86</sub> proxy may not reflect a strictly marine ocean temperature. The Branched and Isoprenoid Tetraether index (BIT Index; Hopmans et al., 2004) can be applied to constrain the presence of terrestrial iGDGT compounds at Site U1463. The BIT Index is a proxy for soil vs. marine organic matter input as a ratio of terrestrially sourced branched GDGTs I, II and III versus marine sourced crenarchaeol (IV) (Equation 7):

$$\text{BIT index} = \frac{[\text{brGDGT I} + \text{brGDGT II} + \text{brGDGT III}]}{[\text{brGDGT I} + \text{brGDGT II} + \text{brGDGT III} + \text{IV}]} \quad (7)$$

BIT values between 0.98-1 indicate that compounds formed in soils and contain almost entirely branched GDGTs, and values near 0 indicate either no terrestrial origin of organic matter or high concentrations of crenarchaeol. Previous studies have determined that low BIT index values (approximately <0.3-0.4) indicate that the relative concentration of soil-derived GDGTs is low overall (Weijers et al., 2006).

#### 1.3.4 MBT'<sub>5ME</sub> Mean Annual Air Temperature Proxy

Branched GDGTs (hereafter, brGDGTs) are believed to be lipid membranes of certain unknown bacteria, possibly acidobacteria (Weijers et al., 2006; Weijers et al., 2007a; Sinninghe Damsté et al., 2011; Sinninghe Damsté et al., 2014) and are produced in soils, peats, rivers and lakes (Schouten et al., 2000; Sinninghe Damsté et al., 2000; Weijers et al., 2007a; Sinninghe Damsté et al., 2009; De Jonge et al., 2013; De Jonge et al., 2014a; De Jonge et al., 2014b). Unlike iGDGTs that are comprised of isoprenoid structure alkyl moieties (Castañeda & Schouten, 2011), brGDGTs are comprised of branched carbon chains (Sinninghe Damsté et al., 2000) and can contain different numbers of cyclopentane moieties (Schouten et al., 2000). These compounds can reach marine environments via wind or river runoff.

Weijers et al. (2007a) developed the methylation index of branched tetraethers (MBT), which measures the ratio of brGDGTs containing between 4-6 methyl branches (Figure 1.12)(Sinninghe Damsté et al., 2000; Weijers et al., 2006; Weijers et al., 2007a). Through studying a suite of globally distributed soil samples, the authors noted a relationship between the degree of methylation and mean annual air (soil) temperature. The original MBT calibration was later revised by Peterse et al. (2012), who added additional sites to the global soils calibration and measured the relative abundances of each brGDGT species versus MAT (°C). The authors found that brGDGTs IIIb and IIIc were absent in 204 of the analyzed 278 samples and thus they eliminated IIIb and IIIc from the MBT calculation and refined the MBT index to MBT'. De Jonge et al. (2014a) then critically revised the MBT' proxy after discovering brGDGT isomers IIa'-IIc' and IIIa'-IIIc' (Figure 1.12)(De

Jonge et al., 2013; De Jonge et al., 2014b), which co-eluted using older HPLC separation techniques and therefore were previously measured together. Since the development of the MBT and MBT' proxies, HPLC chromatography has improved and newer techniques developed to better facilitate separation of structurally similar compounds.

Hexamethylated brGDGT isomers IIIa'-IIIc' (Figure 1.12) and pentamethylated brGDGT isomers IIa'-IIc' differ from non-isomers by the position (6' rather than 5') of the fifth and six methyl branches along the C<sub>28</sub> alkyl carbon chain. The separation of 6-methyl isomers (Figure 1.12), which resulted from significant improvements in HPLC chromatography, allowed De Jonge et al. (2014a) to recalibrate MBT' to MBT'<sub>5ME</sub> (Equations 7 and 8). In 2016, Hopmans et al. (2016) further improved the quantification of GDGT compounds by utilizing double silica columns for HPLC chromatography. The authors identified noticeable differences in resulting MBT'<sub>5ME</sub> values using this new method, and therefore suggest that the proxy be recalibrated in the future to best fit the two-column methodology (Hopmans et al., 2016).

$$MBT'_{5ME} = \frac{Ia+Ib+Ic}{Ia+Ib+Ic+IIa+IIb+IIc+IIIa} \quad (8)$$

$$MAT = -8.57 + 31.45 * MBT'_{5ME} \quad (9)$$

The MBT'<sub>5ME</sub> versus measured MAT (°C) calibration by De Jonge et al. (2014a) is based on soils and yields a strong correlation ( $r^2=0.66$ ) to one another. The calibration error of the MBT'<sub>5ME</sub> proxy is +/- 4.6°C (De Jonge et al., 2014a).

Recent studies have determined that branched GDGTs can also form in-situ in marine environments (Sinninghe Damsté, 2016). This poses the question of whether brGDGTs within marine samples were formed in-situ or were transported from terrestrial soils. In 2016, Sinninghe Damsté addressed this question by introducing a new proxy called the #rings<sub>tetra</sub> index to distinguish soil from marine produced brGDGTs (Equation 9). The authors analyzed brGDGT distributions across the Berau shelf, NE Kalimantan, Indonesia, and observed high concentrations of both brGDGT Ia and tetramethylated brGDGTs at the mouth of the river delta, corresponding to a low #rings<sub>tetra</sub> value of 0.22. Further from the outlet of the river delta, concentrations of pentamethylated brGDGTs increased, and the value of #rings<sub>tetra</sub> rose to 0.83. The authors conclude that #rings<sub>tetra</sub> values greater than 0.7 indicate marine in-situ production, and values below 0.7 suggest continental brGDGT production.

$$\text{\#rings}_{\text{tetra}} = ([\text{Ib}] + 2 * [\text{Ic}]) / ([\text{Ia}] + [\text{Ib}] + [\text{Ic}]) \quad (10)$$

This will be a critical proxy to apply on sediments from Site U1463, in order to determine if temperatures calculated from MBT'<sub>5ME</sub> reflect a continental air temperature signal.

BrGDGTs have been successfully utilized on samples collected in the Congo River drainage basin to reconstruct continental temperatures in the Congo Basin over the last 25,000 years (Weijers et al., 2007b). Weijers et al. (2007b) applied the original MBT proxy to constrain shifts in Congo Basin continental temperatures, and successfully compared results to drainage basin SSTs in order to determine the relationship between tropical Atlantic Ocean temperatures and inland climate. Similar to the study by Weijers et al. (2007b), brGDGT compounds preserved in marine sediments from Site U1463 will be quantified in order to determine continental temperatures in northwest Australia across the study period. Air temperatures will be calculated using the more recent MBT'<sub>5ME</sub> proxy (De Jonge et al., 2014a), and will be compared to offshore SSTs in order to relate offshore shifts in ocean temperature with onshore shifts in continental climate.

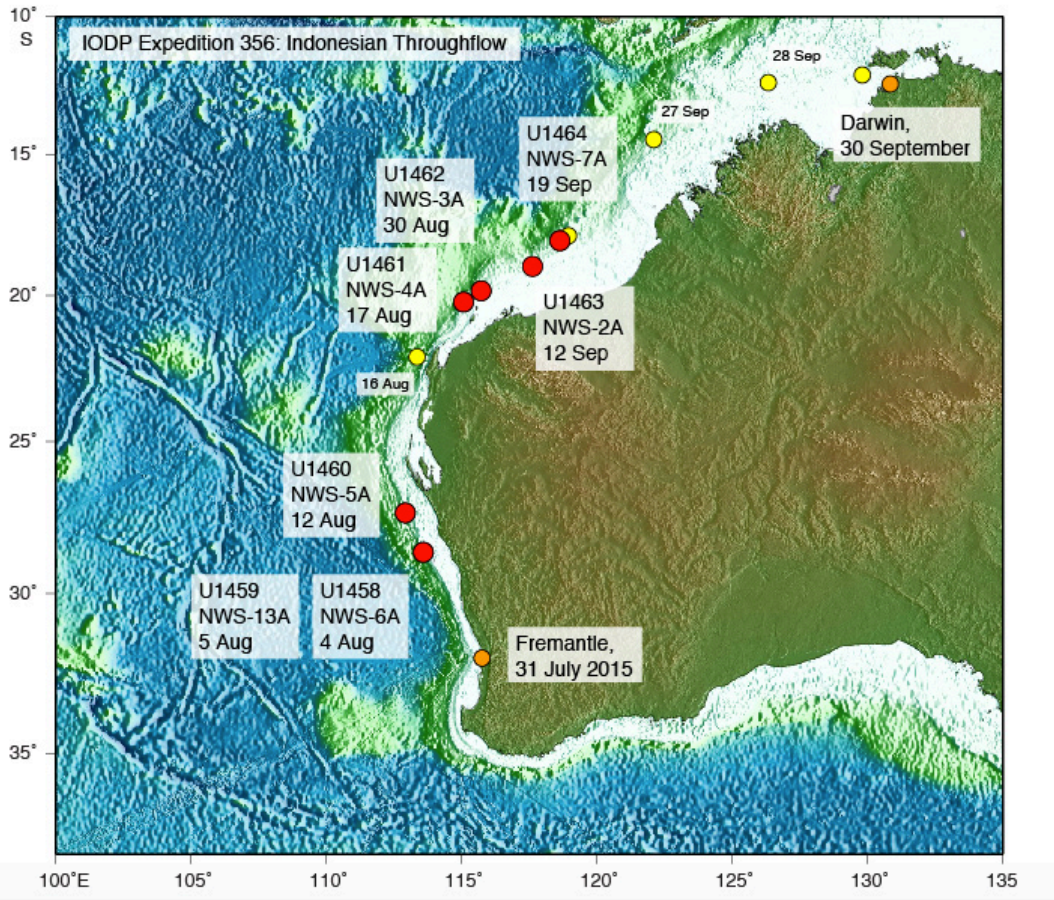


Figure 1.1: Drilling Sites U1458-U1464 of IODP Expedition 356 across NW Australia. Image from IODP Discovery Program *JOIDES* Resolution Science Operator: URL: [http://iodp.tamu.edu/scienceops/expeditions/indonesian\\_throughflow.html](http://iodp.tamu.edu/scienceops/expeditions/indonesian_throughflow.html).

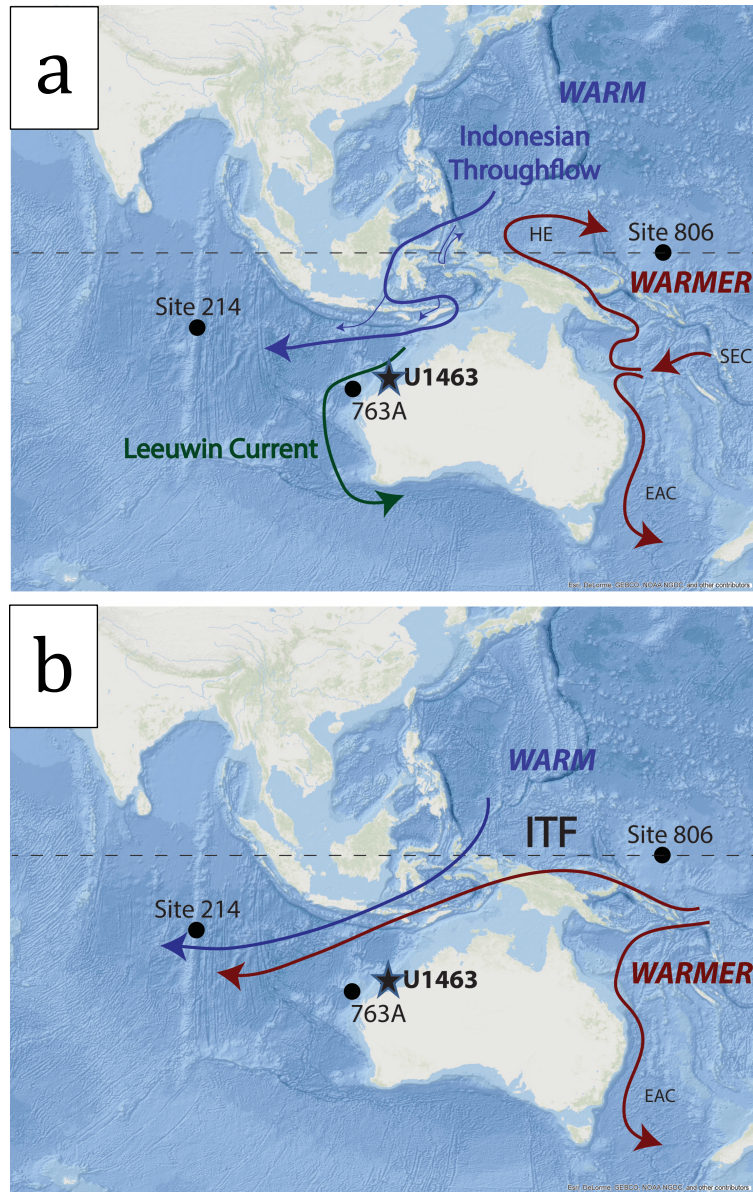


Figure 1.2: Site U1463 analyzed in this study (black star), as well as Sites 763A, 214, and 806. Plotted in **a**) a modern illustration of ocean currents in and around NW Australia, including the Leeuwin Current (LC; green), the Indonesian Throughflow (ITF; blue), and the South Equatorial Current (SEC; red), which splits south to the Eastern Australian Current (EAC) and north to the Halmahera Eddy (HE). Notably in Illustration **a**), South Pacific warm water is diverted back into the Pacific Ocean via the HE, and the ITF is dominated by cooler North Pacific source waters. All Sites are also plotted in **b**) a Pliocene illustration of hypothesized ocean current dynamics prior to tectonic constriction and shallowing. Notably in **b**), South Pacific warm waters can flow through the ITF and freely mix with cooler North Pacific source waters. It is also important to note that the LC was not present during the Pliocene and thus absent from **b**). Figure modified from Esri “World Ocean Base” [basemap].

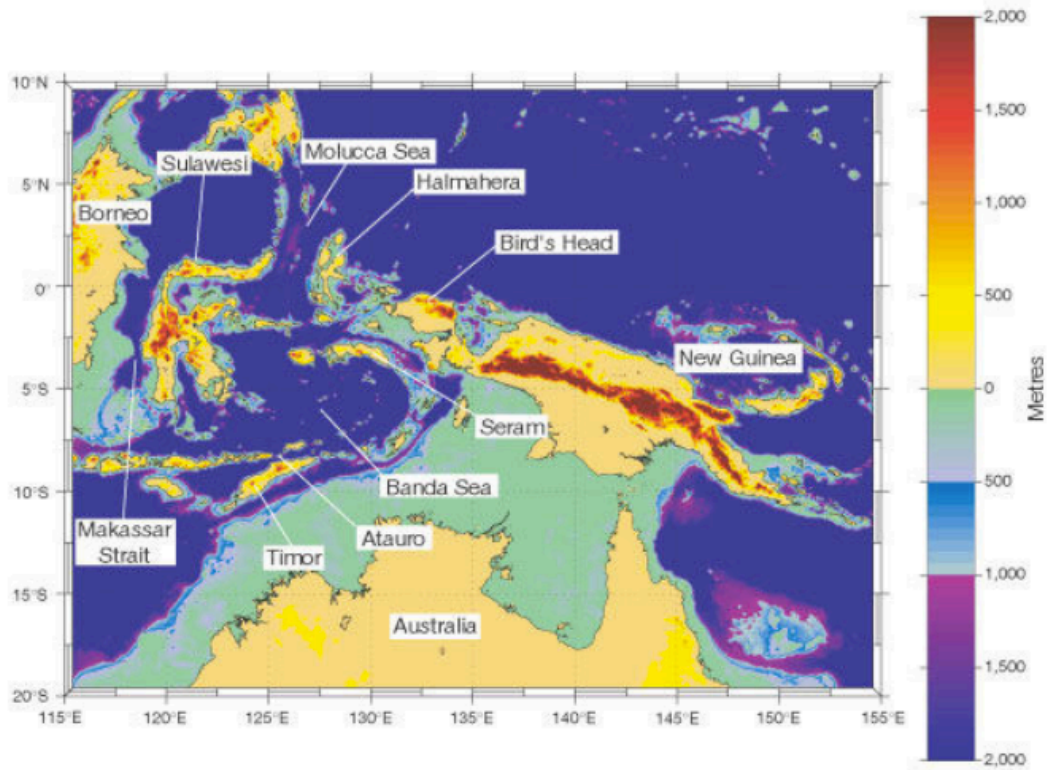


Figure 1.3: Depth (meters) of islands within the ITF constituting what is referred to as the Maritime Continent. Most of the land mass of Halmahera, between 125°E-130°E, was exposed during shoaling of the ITF and regional volcanism between 5-3 Ma. From Cane and Molnar (2001).

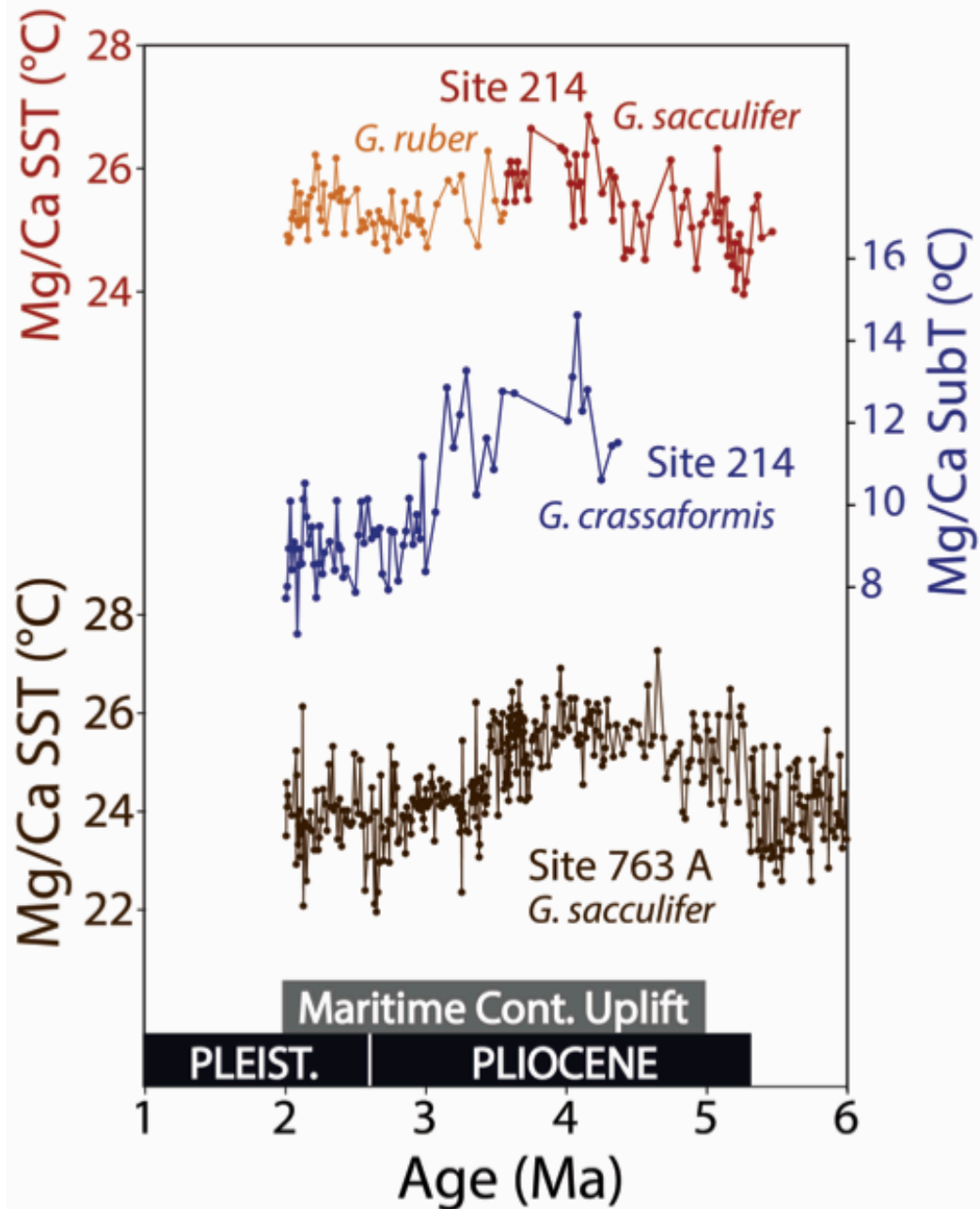


Figure 1.4: Geochemical records from Indian Ocean Sites ODP 214 and ODP 763A. Shown in the upper curve (red) and middle curve (blue) are Mg/Ca SST reconstructions from 5.5-2 Ma from Karas et al. (2009). Shown in blue (*G. crassaformis*) are subsurface Mg/Ca temperatures from Site 214. Shown in the bottom curve (brown) is the Mg/Ca SST reconstruction from Site 763A from Karas et al. (2011a). The lowermost gray bar indicates the period of Maritime Continental Uplift (5-2 Ma).

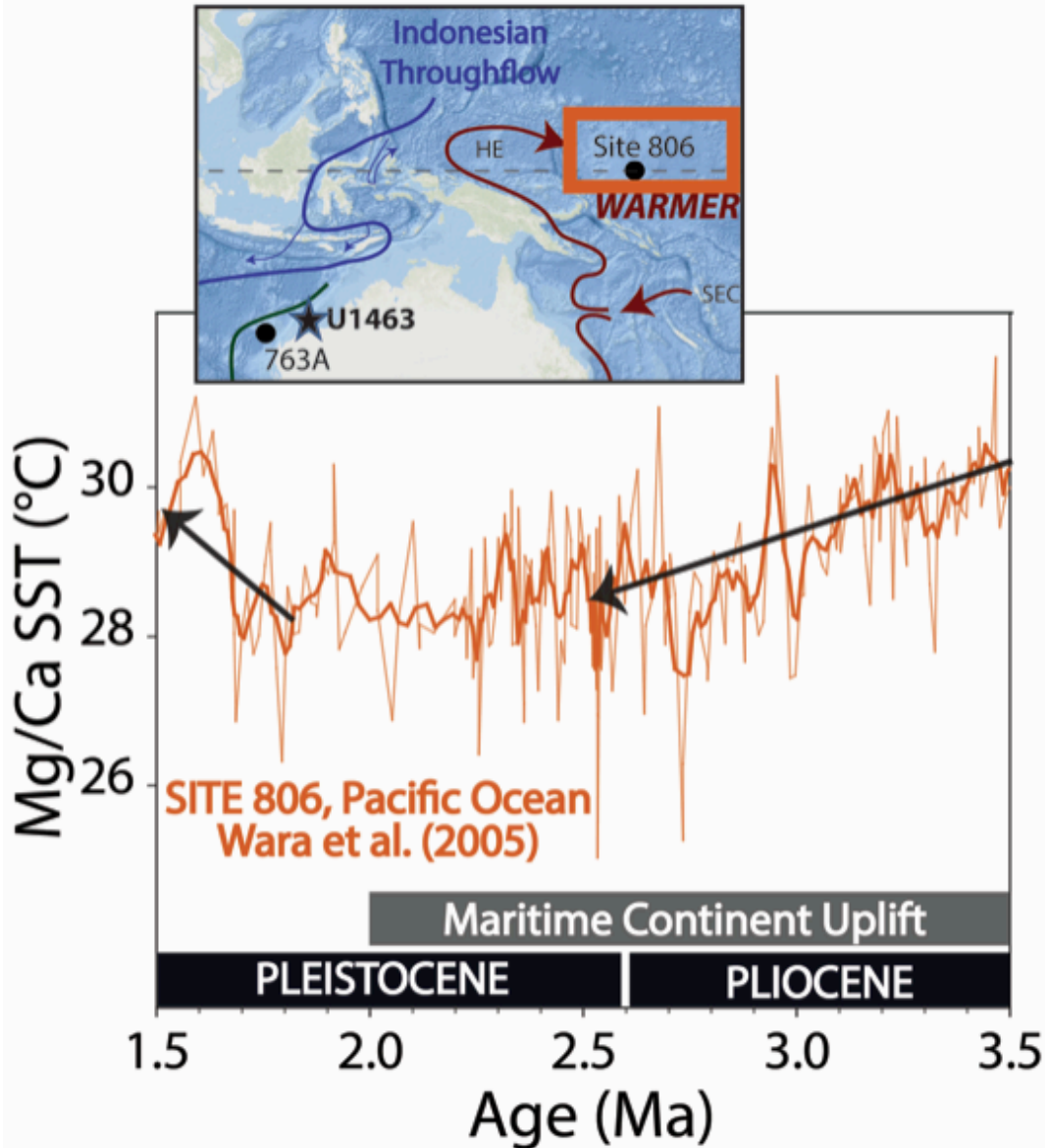
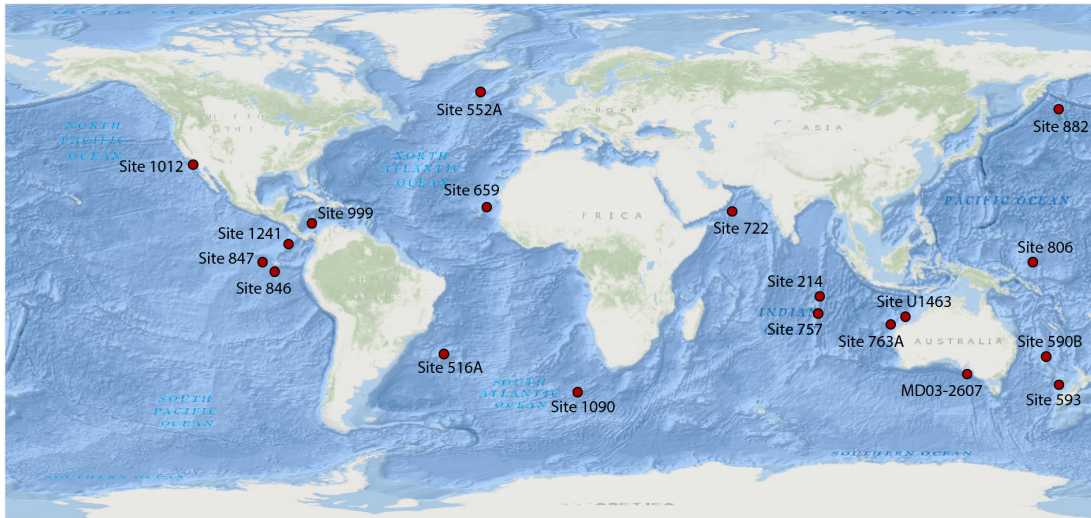


Figure 1.5: The SST record from Site 806 (Wara et al., 2005), located in the western equatorial Pacific (WEP), near the inlet of the ITF and the return flow of south Pacific warm waters from the HE. The dark orange line indicates a smoothed 5 point running average of SST data.



Esri, Delorme, GEBCO, NOAA NGDC, and other contributors. Sources: Esri, GEBCO, NOAA, National Geographic, Delorme, HERE, Geonames.org, and other contributors.

Figure 1.6: Global map of relevant SST records. In the Pacific Ocean are study Sites 1012 (Brierley et al., 2009), 1241 (Steph et al., 2006, 2010), 847 (Wara et al., 2005), 846 (Brierley et al., 2009), 882 (Martínez-García et al., 2010), 806 (Wara et al., 2005), 590B (Karas et al., 2011b), and 593 (McClymont et al., 2008). In the Atlantic Ocean are study Sites 552A (Karas et al., 2017), 659 (Tiedemann et al., 1994), 516A (Karas et al., 2017), 999 (Haug and Tiedemann, 1998) and 1090 (Martínez-García et al., 2010). Sites 722 (Herbert et al., 2010), 214 (Karas et al., 2009), 757 (Martin and Scher, 2006), 763A (Karas et al., 2011a), MD03-2607 (Lopes dos Santos, 2013) and U1463 (this study) are located in the Indian Ocean. Figure modified from Esri “World Ocean Base” and Esri “World Ocean Reference”.

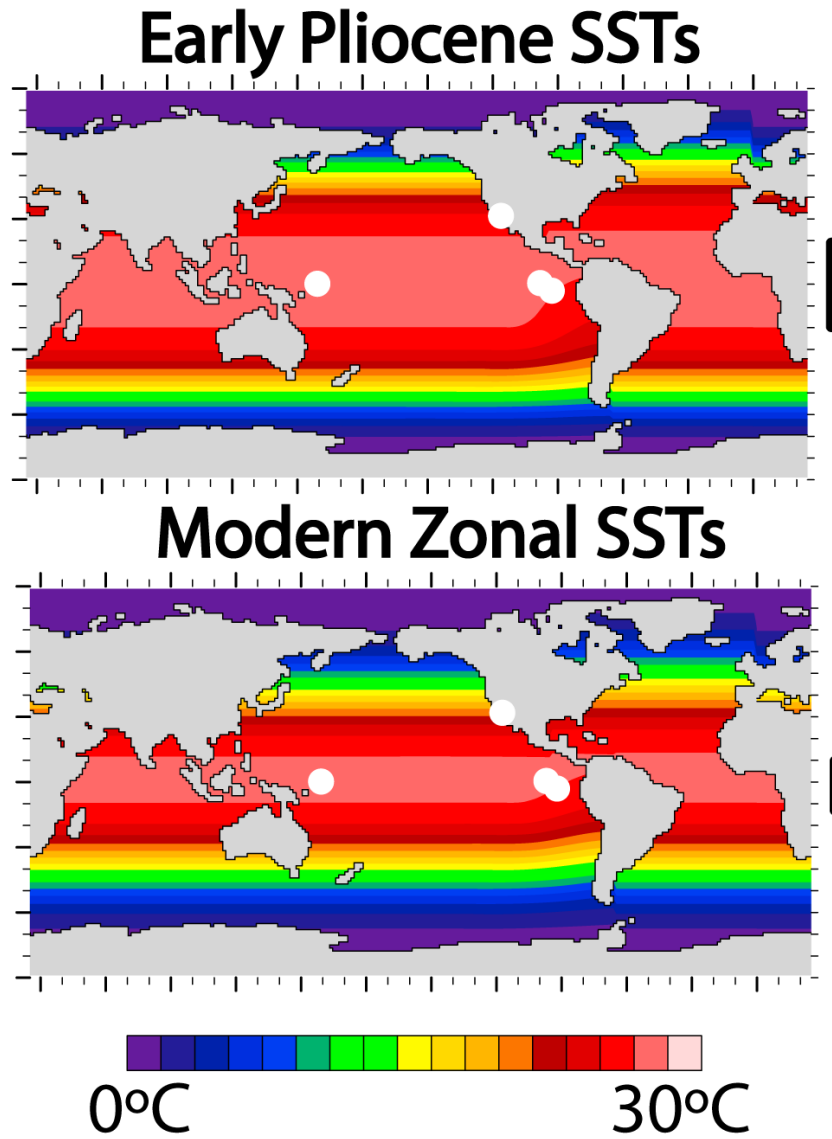


Figure 1.7: The modeled extent of the equatorial warm pool in the Pliocene versus the Modern (edited from Brierley and Fedorov, 2010). Black bars on the right indicate the latitudinal extent of the warm pool across each period.

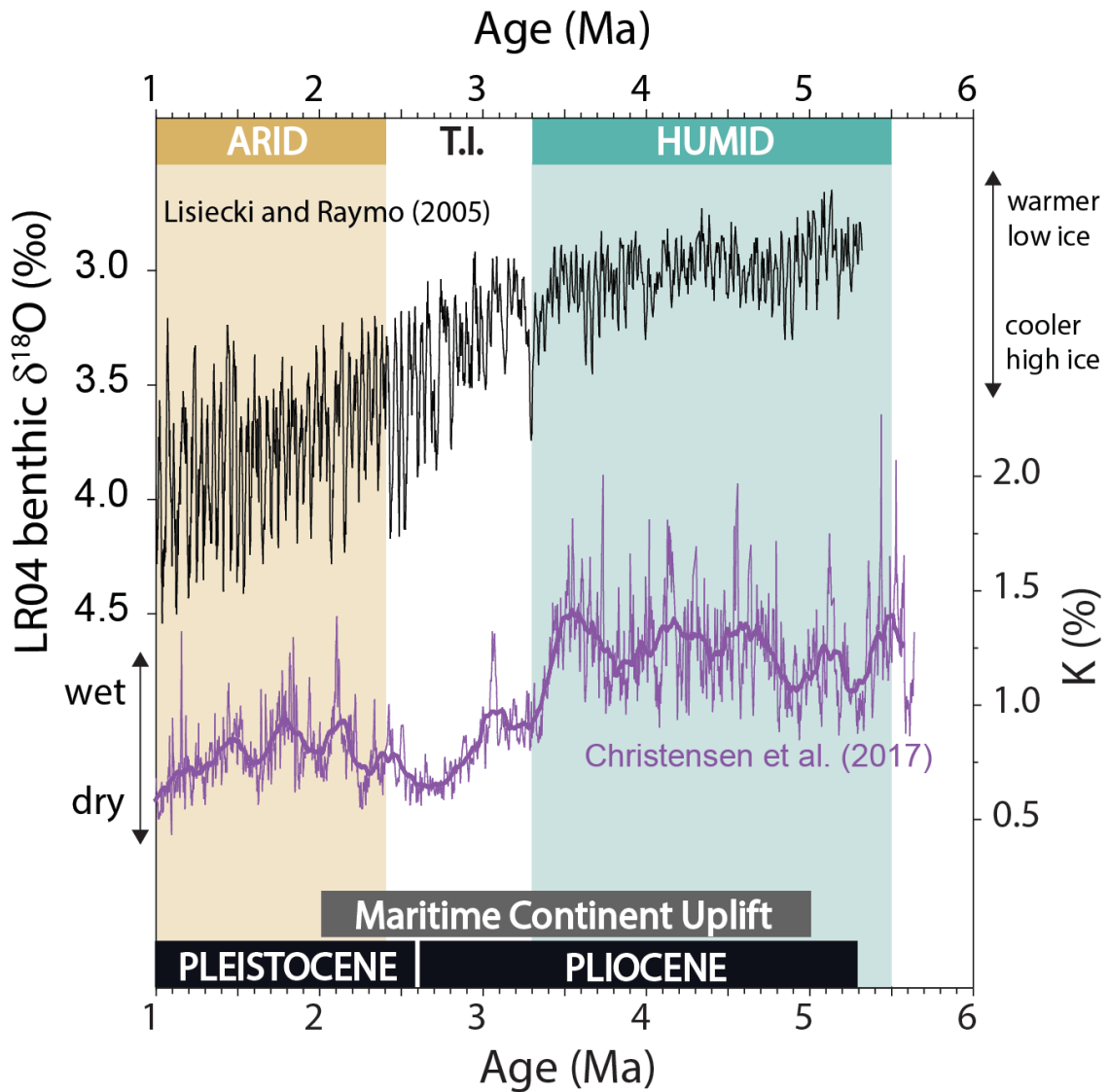


Figure 1.8: Age vs. %K (Christensen et al., 2017) and  $\delta^{18}\text{O}$  (Lisiecki and Raymo, 2005). %K is depicted in purple (lower), with higher values showing wetter conditions. The LR04 benthic  $\delta^{18}\text{O}$  stack is depicted in black (upper), with more enriched values indicating higher global ice volume. The Humid Interval is shown in light green, extending from 5.5-3.3 Ma. The Arid Interval is shown in light brown, extending from 2.4-1 Ma. Depicted in grey is the period of Maritime Continental Uplift (5-2 Ma).

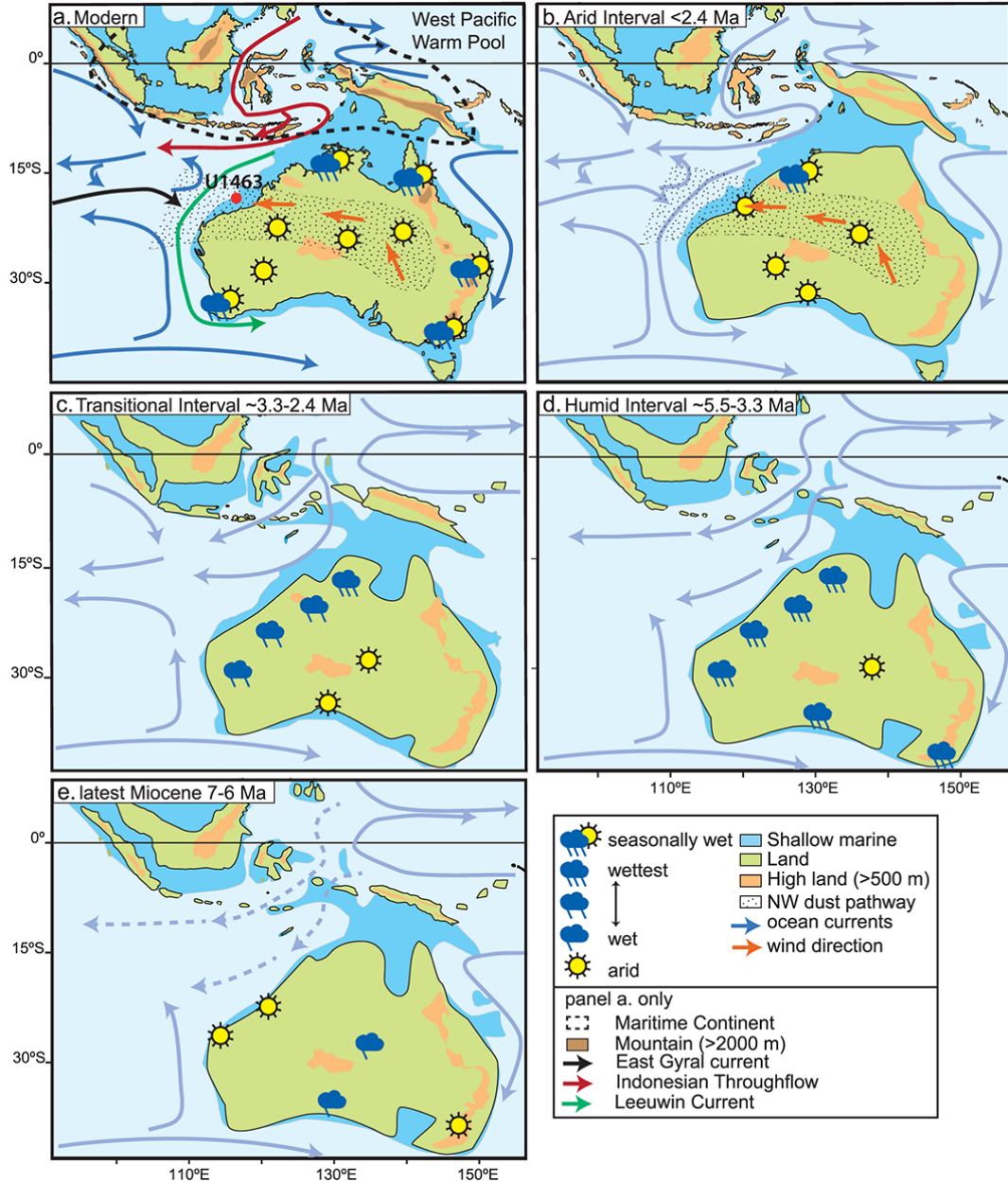


Figure 1.9: Illustration of evolution of NW Australian hydrology from 7 Ma to the modern (Christensen et al., 2017). Moving from e→a: **e**) the ITF during the latest Miocene, from 7-6 Ma, prior to Maritime Continental Constriction, **d**) the onset of humidity in NW Australia from 5.5-3.3 Ma, associated with the onset of ITF constriction and emergence of Maritime Continent, **c**) the Transition Interval, extending from 3.3-2.4 Ma, showing a transition to more arid conditions and a switch in ITF source water, **b**) the onset of the Arid Interval from 2.4-1 Ma, showing the complete emergence of New Guinea and Halmahera and the complete shift from South Pacific to the North Pacific ITF source waters, and **a**) the modern ocean-atmosphere climate system in NW Australia and the presence of the Leeuwin Current across the west coast of Australia.

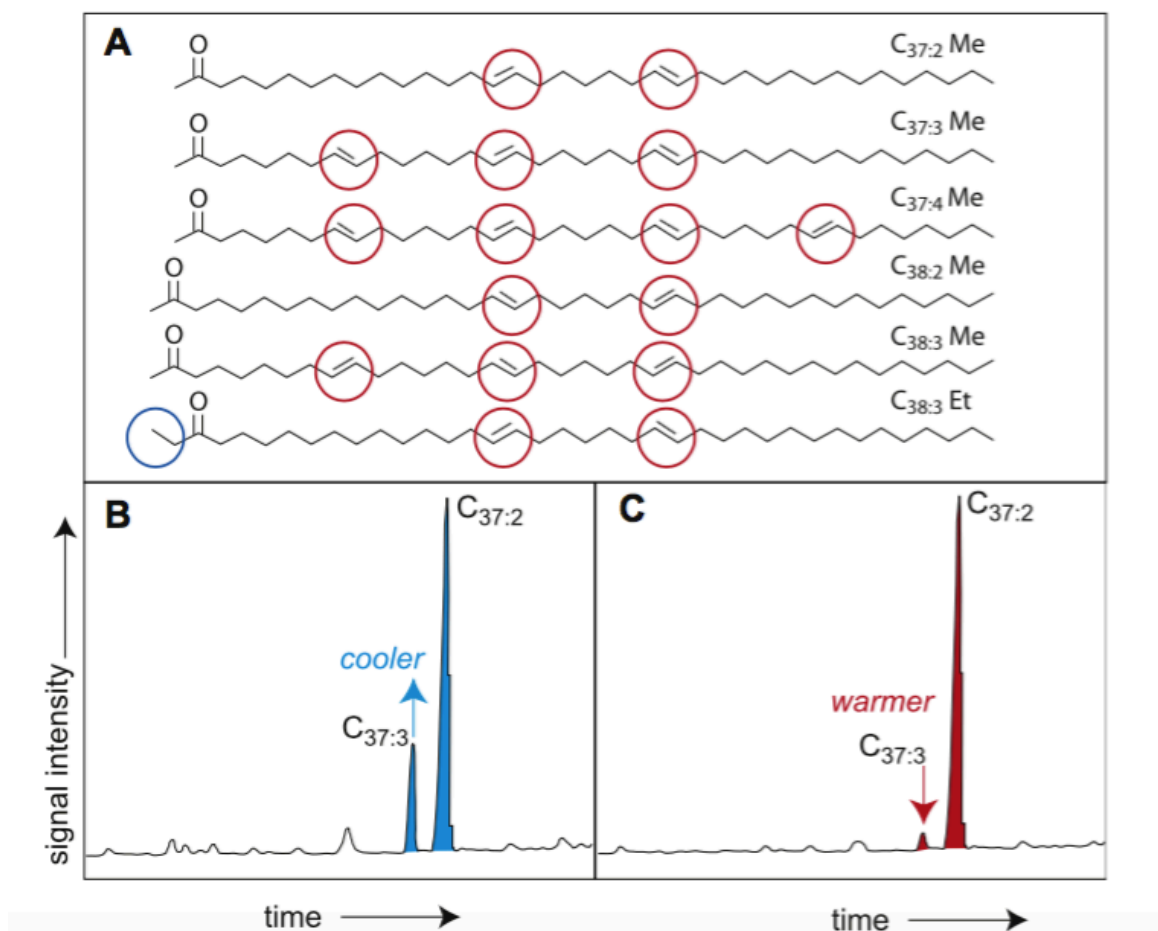


Figure 1.10: Structural changes in long chain alkenones associated with shifts in water temperature. A) structures of long chain alkenones, notably C<sub>37:2</sub>-C<sub>37:4</sub>, which are distinguished by numbers double bonds shown in red circles. B) an example GC-MS chromatogram from of a cold sample containing relatively high concentrations of unsaturated C<sub>37:3</sub>. C) a similar chromatogram under warmer conditions showing a decrease in C<sub>37:3</sub> as the sample approaches saturation. From Castañeda et al. (2011).

# TEX<sub>86</sub>

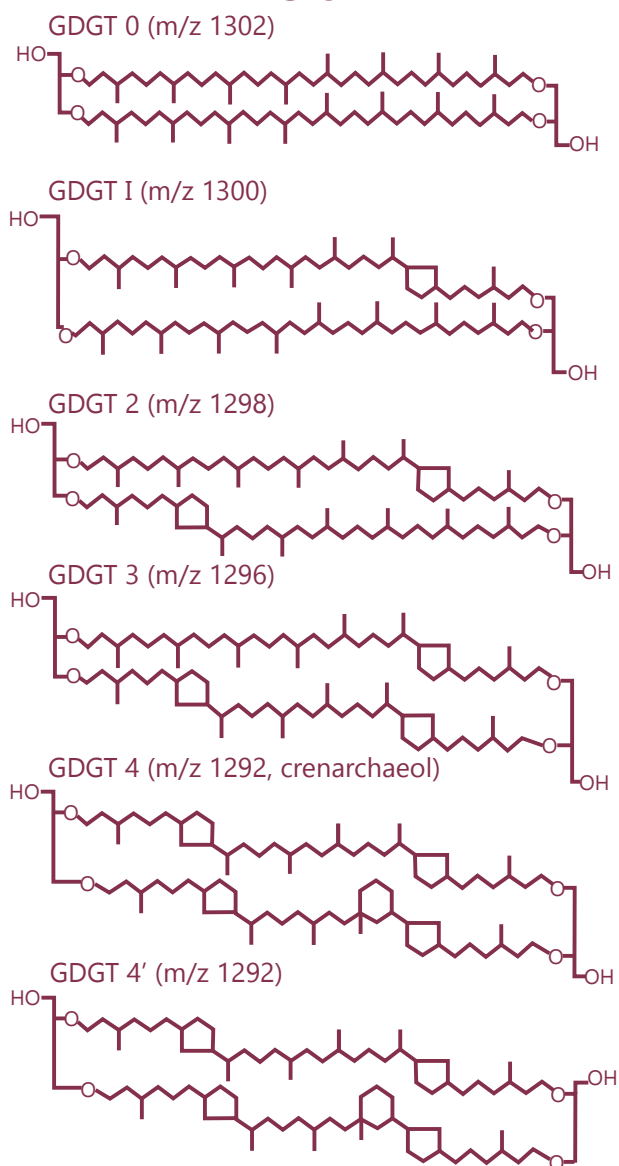


Figure 1.11: Isoprenoid GDGT structures. On either end of each compound are glycerol alkyl groups. Illustrated by I. Castañeda.

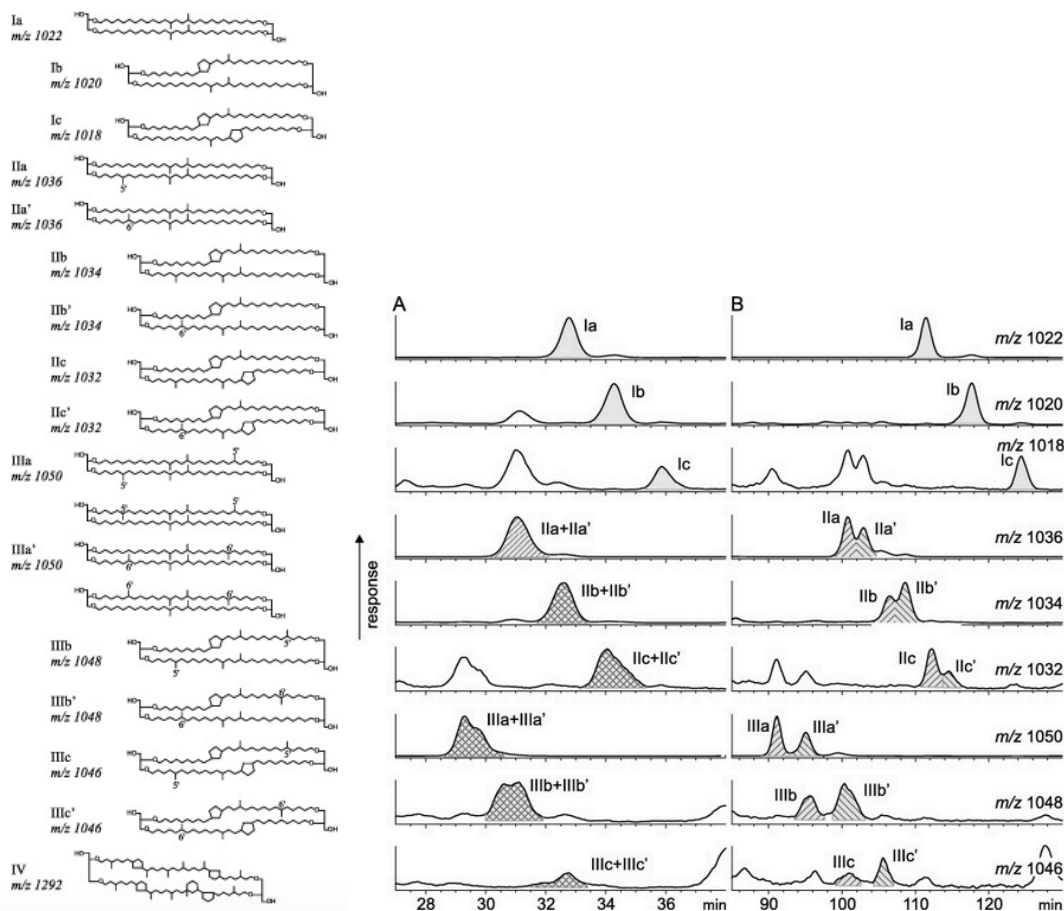


Figure 1.12: Branched GDGT structures. From De Jonge et al., 2013, 2014a-b, **LEFT**) Structures of brGDGTs and their isomers (De Jonge et al., 2014a-b). BrGDGTs containing four methyl branches are tetra-methylated and written as brGDGTs Ia-c. BrGDGTs IIa-c contain one more methyl branch than brGDGTs Ia-c, located five carbons into the molecule's carbon chain, and are considered penta-methylated. BrGDGTs IIIa-c contain six methyl branches, with the additional methyl branches located at the 5 and 5' carbon positions on the opposite ends of the molecule, and are considered hexa-methylated. BrGDGTs Ib, IIb, and IIIb each contain one cyclopentane ring, and brGDGTs Ic, IIc and IIIc each contain two cyclopentane rings. No isomers were identified for brGDGTs Ia-Ic. Pentamethylated brGDGTs IIa-IIc (containing 5 methyl branches) have their 5<sup>th</sup> methyl branch at location 5' along the C<sub>28</sub> chain, whereas pentamethylated brGDGT isomers IIa'-IIc' have their 5<sup>th</sup> methyl branch at location 6' along the C<sub>28</sub> alkyl chain. The same pattern is observed in Hexamethylated brGDGTs. GDGTs IIIa-IIIc (containing 6 methyl branches) have their 5<sup>th</sup> and 6<sup>th</sup> methyl branches located at location 5' at each end of the compound, whereas hexamethylated brGDGT isomers have their 5<sup>th</sup> and 6<sup>th</sup> methyl branches located at the 6' position along each end of the alkyl chain. **RIGHT**) A- Chromatograms from Schouten et al. (2007) of brGDGTs I-III, where isomers are indistinguishable from non-isomer brGDGT peaks. B- Chromatograms from De Jonge et al. (2014a), with brGDGT IIa-c and IIIa-c peaks distinguished from their respective isomer peaks, IIa'-c' and IIIa'-c'.

## CHAPTER 2

### METHODS

#### 2.1 Sample Preparation

A total of 376 sediments were sampled from the continuous, stratigraphically correlated core spliced from Holes B-D at IODP Site U1463 (18°58'S, 117°37'E; Figures 1.1-1.2; detailed in Christensen et al., 2017). Sediments were collected approximately every 35 cm between 161.45-401.77 cored meters below sea-level (m CSF-A), corresponding to a sample resolution of ~5 ka between 1.50-3.48 Ma B.P.

Samples were freeze-dried and homogenized, and the total lipid extract (TLE) was collected using dichloromethane (DCM): methanol (MeOH) (9:1, v:v) and a Dionex accelerated solvent extractor (ASE 200). Once extracted, TLEs were dried under a stream of N<sub>2</sub> gas and sequentially separated with activated alumina oxide into apolar, ketone and polar fractions using solvent mixtures of DCM:hexane (9:1, v:v), DCM:hexane (1:1, v:v), and DCM:MeOH (1:1, v:v), respectively. Polar fractions were split equally using DCM:MeOH (1:1, v:v).

#### 2.2 Alkenones

Ketone fractions were injected into a dual inlet Agilent 7890A gas chromatograph (GC) coupled to a flame ionization detector (FID). Compounds eluted from an Agilent 19091J-416 Column (60m x 320µm x 0.25µm) with H<sub>2</sub> gas and an oven program beginning at 70°C, ramping at 17°C /min to 130°C, ramping at 7°C per min to 320 °C and holding for 15 minutes. Alkenone concentrations were quantified using an external squalane calibration curve, and values of U<sup>k</sup><sub>37</sub> were

calculated following the definition by Prah1 and Wakeham (1987)(Equation 1). Sea surface temperatures were calculated using the global core top calibration from Muller et al. (1998)(Equation 2).

### **2.3 Long Chain Diols**

One half of each polar fraction was derivatized using equal parts of BSTFA and acetonitrile (1:1, v:v) and placed in a 60°C oven for 30 minutes. Samples were then dried under N<sub>2</sub> gas and injected into an HP 6890 gas chromatograph (GC) coupled to an Agilent 5973 mass selective detector (MSD) following the methods of Rampen et al. (2012) and Rampen et al. (2008). Compounds eluted from an Agilent DB-5ms GC column (60m x 0.32 mm x 0.25 µm) with He gas and a temperature program beginning at 70°C, heating to 170°C at a rate of 20°C/min, heating again to 300°C at a rate of 4°C/min, and remaining at high temperature for 35 minutes. Compounds were analyzed in selective ion monitoring (SIM) mode for m/z ratios 299 (C<sub>28</sub> 1,14), 313 (C<sub>28</sub> 1,13 and C<sub>30</sub> 1,15), 327 (C<sub>30</sub> 1,14), and 341 (C<sub>30</sub> 1,13 and C<sub>32</sub> 1,15).

SSTs were calculated by determining the Long-Chain Diol Index (LDI) (Equation 3) and applying the calibration of Rampen et al. (2012) (Equation 4).

### **2.4 Isoprenoid and Branched GDGTs**

The other half of each polar fraction was filtered through a 0.45µm PTFE filter using hexane:isopropanol (99:1, v:v). Samples were subsequently dried under a stream of N<sub>2</sub> gas, and C<sub>46</sub> was added as internal standard for compound quantification. Glycerol dialkyl glycerol tetraethers (GDGTs) were measured on an Agilent 1260 series ultra-high performance liquid chromatograph (HPLC) coupled

to an Agilent 6120 single quadrupole mass selective detector (MSD) following the methods of Hopmans et al. (2016). Compounds were eluted from two in series BEH HILIC Columns (2.1 x 150mm, 1.7 $\mu$ m; Waters) held initially at 30°C using mixtures of solvent A) pure hexane and B) hexane:isopropanol (9:1; v/v) following the elution method from Hopmans et al. (2016) at a flow rate of 0.2mL/min.

Compounds were analyzed in selective ion monitoring (SIM) mode for m/z ratios between 744-1302.

Sea surface temperatures were calculated using the TetraEther index with 86 carbon atoms (TEX<sub>86</sub>; Schouten et al., 2002) and based on isoprenoidal GDGTs with m/z ratios 1302 (GDGT-0), 1300 (GDGT-1), 1298 (GDGT-2), 1296 (GDGT-3), 1292 (GDGT-4) and 1292' (GDGT-4') (Equation 5). TEX<sub>86</sub> values were converted to temperatures using the SST and subsurface temperature (hereafter, sub-T) BAYSPAR calibrations by Tierney and Tingley (2014, 2015). In order to confirm that iGDGTs were sourced from marine sediments rather than continental soils, the BIT Index was also applied (Equation 7; Hopmans et al., 2004) to sediments from Site U1463.

Continental air temperature was determined using the revised methylation index of branched tetraethers (MBT'<sub>5ME</sub>; De Jonge et al., 2014a; Equation 8) and based on ratios of 5-methyl brGDGT compounds with m/z ratios 1050 (brGDGT-III), 1036 (brGDGT-IIa), 1034 (brGDGT-IIb), 1032 (brGDGT-IIc), 1022 (brGDGT-Ia), 1020 (brGDGT-Ib) and 1018 (brGDGT-Ic). MBT'<sub>5ME</sub> values were converted to mean annual air temperatures (MAT) using the calibration of De Jonge et al. (2014a) (Equation 9).

We additionally calculated the  $\#rings_{tetra}$  index (Equation 10) to determine continental versus marine brGDGT origin (Sinninghe Damste et al, 2016).

## CHAPTER 3

### RESULTS

#### 3.1 Alkenone Data

Initially, the  $U^k_{37}$  Index was going to be applied as a SST proxy. However, the resulting temperature record is highly variable and is not in agreement with the other temperature proxies examined in this study. Further examination of the samples revealed the likely presence of coastal haptophyte species and therefore the  $U^k_{37}$  Index cannot be applied in this study. In general, open ocean long chain alkenone producing species (dominated by *E. huxleyi* and *G. oceanica*) yield  $C_{37}/C_{38}$  ratios between 0.7-1.7, whereas coastal alkenone producing species yield higher values (Prahl & Wakeham, 1987). The average value of the  $C_{37}/C_{38}$  ratio for U1463 sediments is 2.1, the minimum value is 0.96, and the maximum value is 16.4 (Figure 3.1). These high values suggest the presence of coastal marine alkenone producing species at Site U1463, some of which have a very different slope between SST and  $U^k_{37}$  values in comparison to *E. huxleyi* and *G. oceanica*. Furthermore, calcareous nannofossil data confirm the presence of numerous species of coastal haptophytes at Site U1463 (Henderiks et al., unpublished data in prep) and therefore eliminates the use of the  $U^k_{37}$  proxy as a SST paleothermometer here due to mixed assemblages.

#### 3.2 LDI Data

Unlike  $U^k_{37}$ , the LDI proxy was successfully applied to reconstruct SSTs. When averaged across the study interval from 1.5-3.5 Ma, the  $C_{30}$  1,15-diol constitutes 81% of the fractional abundance of long chain diols (Figure 3.2). The  $C_{30}$

1,14-diol makes up 6.9% of total diols, and the C<sub>28</sub> 1,14-diol accounts for 5.65%. In lesser quantities, the C<sub>28</sub> 1,13-diol, the C<sub>30</sub> 1,13-diol and the C<sub>32</sub> 1,15 diol comprise only 1.98%, 1.79% and 2.57% total diols in sediment, respectively. In comparing LDI abundance downcore, at shallower depths the relative concentration of C<sub>30</sub> 1,15-diol decreases and relative concentrations of C<sub>30</sub> 1,14 diol increases, from ~161-170 m CCFS-A (Figure 3.3).

The LDI-SST record (Figures 3.4-3.5, blue) shows that SSTs were relatively high and stable, ranging between ~23-26°C, from 3.5 to ~1.7 Ma. Despite the overall relatively stable SST trend across this interval, there were several notable dips in SSTs from 3.5-1.7Ma. From ~3.3-3.1 Ma, SSTs dropped by 1.6°C. SSTs dropped by 1.7°C from 2.8-2.6 Ma, and by ~4°C from 2.3-2.1 Ma. At 1.8 Ma, SSTs dipped to 22.4°C before increasing to 25°C at 1.7 Ma. The most pronounced cooling trend is observed from 1.7-1.5 Ma (Figure 3.4-3.5), reaching temperatures as low as 16.9°C.

### **3.3 Isoprenoid GDGT Data**

In addition to the LDI, the TEX<sub>86</sub> was applied as another SST proxy based on the relative abundance of isoprenoid GDGTs. The concentration of isoprenoid GDGTs averaged across the study interval is significantly higher at 0.11ug/g sediment relative to the concentration of branched GDGTs, which is 0.03 ug/g sediment (Figure 3.6). This pattern is typical of open marine sediments. There are noticeable increases in iGDGT concentrations from approximately 2.4-2.1 Ma, 1.75-1.65 Ma, and 1.62-1.50 Ma (Figure 3.6) whereas the lowest iGDGT concentrations are noted from approximately 3.42 to 2.76 Ma and from 2.74-2.42 Ma. Furthermore,

there is a net increase in variability from approximately 2.4 Ma into the Pleistocene (Figure 3.6).

The TEX<sub>86</sub> SST record shows net cooling as well as high SST variability ranging from 24-32°C from 3.5-1.5 Ma (Figure 3.4-3.5, purple). There are several notable dips in SST in the TEX<sub>86</sub> record (Figure 3.5). High amplitude drops in SST occur across this record specifically at 1.79 Ma, 2.16 Ma, 2.21 Ma, 2.28 Ma, 2.99 Ma, and at the boundary between the humid and transition interval at 3.3 Ma. A sharp cooling trend within the arid interval from 1.7-1 Ma is evidenced by a decrease in SST from ~31°C to 24°C. Subsurface temperatures reconstructed using the TEX<sub>86</sub> subT BAYSPAR calibration are between 2.6-3.5°C lower than all TEX<sub>86</sub> SSTs, however both records exhibit the same overall trends.

### **3.4 Branched GDGT Data**

While LDI and TEX<sub>86</sub> reconstruct offshore NW Australian SSTs, the MBT'<sub>5ME</sub> proxy was applied to reconstruct continental mean annual air temperatures based on the relative distribution of brGDGTs. Despite the large difference in concentrations between iGDGTs and brGDGTs, both exhibit similar variability in terms of maxima and minima concentrations across the study interval (Figure 3.6). Highest brGDGT concentrations occur from approximately 2.24-2.13 Ma, 1.74-1.68 Ma, and 1.6-1.5 Ma, whereas the lowest brGDGT concentrations are noted from approximately 3.47-2.25 Ma, and 2.13-1.83 Ma (Figure 3.6). Furthermore, there seems to be a slight increase in amplitude of variability from approximately 2.25 Ma into the Pleistocene, although this variability is considerably lower in amplitude than iGDGT variability due to lower overall concentrations of brGDGTs (Figure 3.6).

Although brGDGTs are present in relatively low concentrations, abundances are sufficient to measure the MBT'<sub>5ME</sub> index. Group 1 brGDGTs comprise over 95% of total brGDGTs on average, whereas Group 3 brGDGTs make up the remaining 4.6% of total brGDGT concentrations, and interestingly no Group 2 brGDGTs are present (Figure 3.7).

The ratio of brGDGT groups 1-3 can be used to measure continental mean annual air temperature (MAAT), provided that these compounds formed in continental soils rather than in-situ in marine sediments. The #rings<sub>tetra</sub> index is used to identify the source environment of these Group 1-3 brGDGTs. Notably, all #rings<sub>tetra</sub> values fall below 0.7 within the 3.5-1.5 Ma study interval (Figure 3.8), indicating that all brGDGTs must have originated in continental soils and were not produced in-situ in the ocean [Hypothesis 4]. Therefore, it is appropriate to apply the MBT'<sub>5ME</sub> index to examine past continental temperature.

Across the study interval, the MBT'<sub>5ME</sub> MAAT record indicates a relatively warm Pliocene and a slightly cooler Pleistocene (Figures 3.4 and 3.5). There are small cooling events at 3.3 Ma, 3.1 Ma, and 2.54 Ma, although overall air temperatures are warm and stable from 3.5-2.2 Ma. MAATs increase to 22.1°C near 2.17 Ma, and subsequently decrease to 21.4°C at 2.03 Ma. From 2.03-1.71 Ma, temperatures are relatively stable, and at 1.71 Ma, cooling begins. Air temperatures are lowest at 20.5°C by 1.50 Ma. Overall shifts in air temperature do not exceed 1.5°C at any point from 3.5-1.5 Ma.

Finally, the BIT index was applied in order to determine the relative input of continental versus marine organic matter to Site U1463. BIT values range between

0.46-0.08 and have an average value of 0.16 (Figure 3.9). These low values likely correspond to the low concentration of brGDGTs sourced from continental soils at Site U1463. Maximum BIT values occur approximately between 2.66-2.59 Ma, 2.42-2.04 Ma, and 1.82-1.50 Ma, and minimum values between 3.46-2.66 Ma, 2.59-2.43 Ma, and 2.04-1.82 Ma. Notably similar to both iGDGT and brGDGT concentration curves (Figure 3.6), BIT values increase in amplitude of variability from approximately 2.4-1.5 Ma. The highest BIT value of 0.46 occurs late in the record at 1.55 Ma, which may reflect a slight increase in continental dust input at Site U1463.

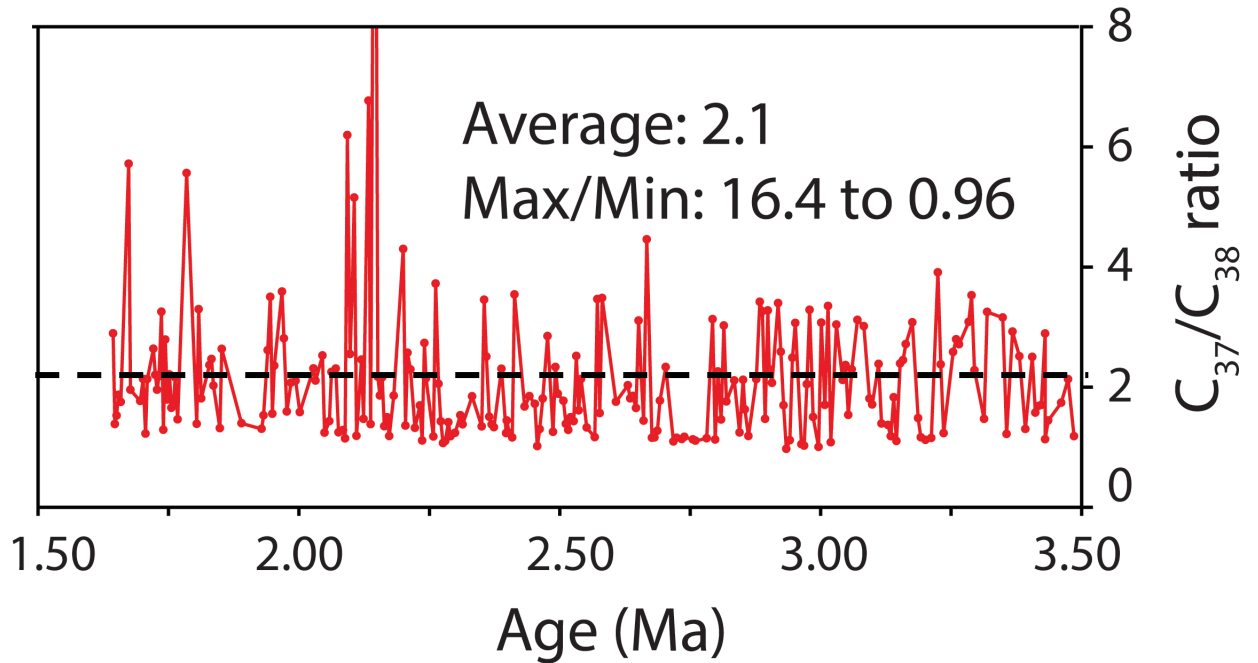


Figure 3.1: The ratio of  $C_{37}$  to  $C_{38}$  LCAs measured at Site U1463 versus Age from 3.5-1.5 Ma. The black dashed bar indicates average  $C_{37}/C_{38}$  ratio values.

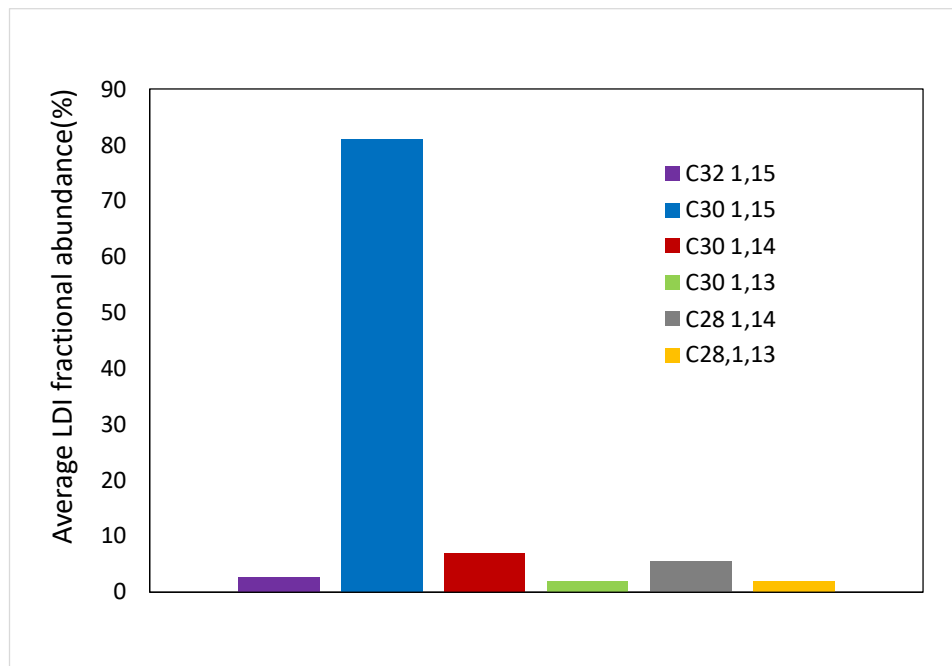


Figure 3.2: Fractional abundance of each long chain diol (%), averaged across the entire study interval from 3.5-1.5 Ma.

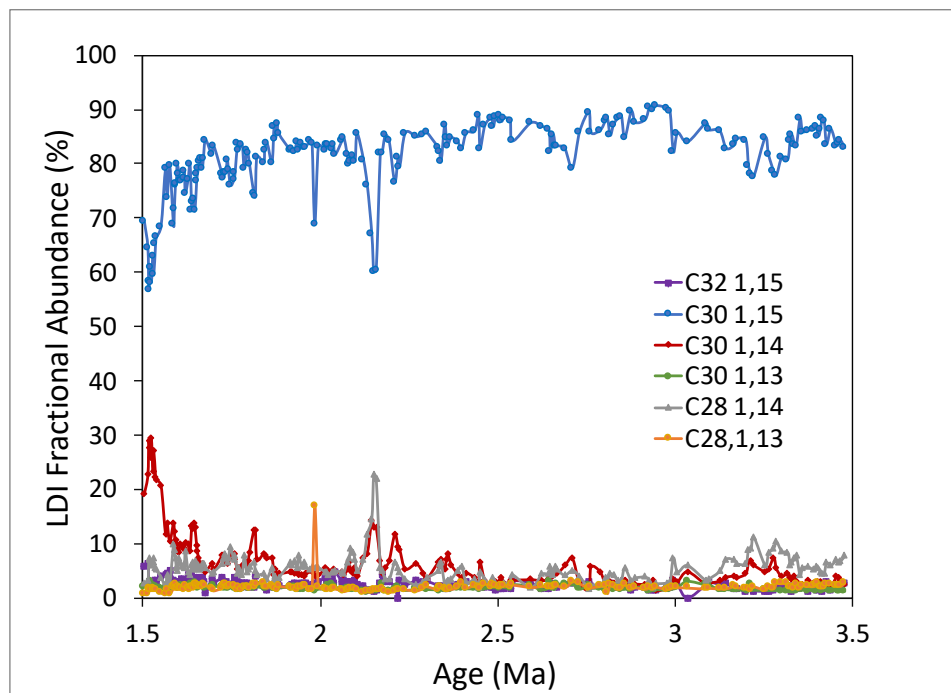


Figure 3.3: Fractional abundance, reported in % of total long chain diol concentration, of each long chain diol plotted versus core depth in meters core composite depth below seafloor (m CCFS-A).

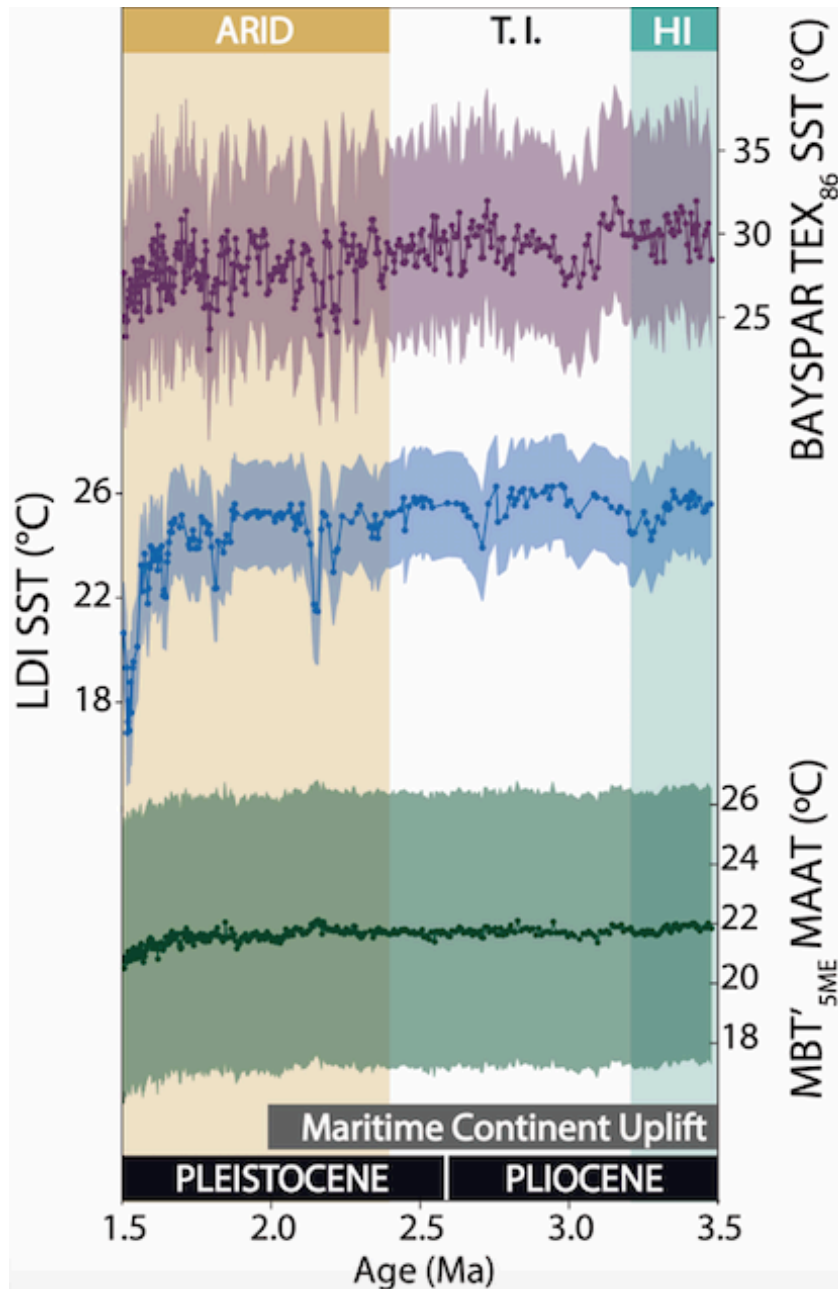


Figure 3.4: Temperature records with calibration error from Site U1463 vs. Age from 3.5-1.5 Ma. The upper curve shows the high-resolution BAYSPAR TEX<sub>86</sub> record, as well as the calibration error of the proxy ( $\pm 2.5^{\circ}\text{C}$ ). The middle curve shows the LDI SST record, with a calibration error shown in blue of  $\pm 2^{\circ}\text{C}$ . The lower curve shows mean annual air temperature derived using the MBT'<sub>5ME</sub> proxy, as well as the calibration error of the proxy ( $\pm 4.6^{\circ}\text{C}$ ). Superimposed over data are the three hydrologic (brown for arid, white for transition, and teal for humid) intervals identified by Christensen et al. (2017).

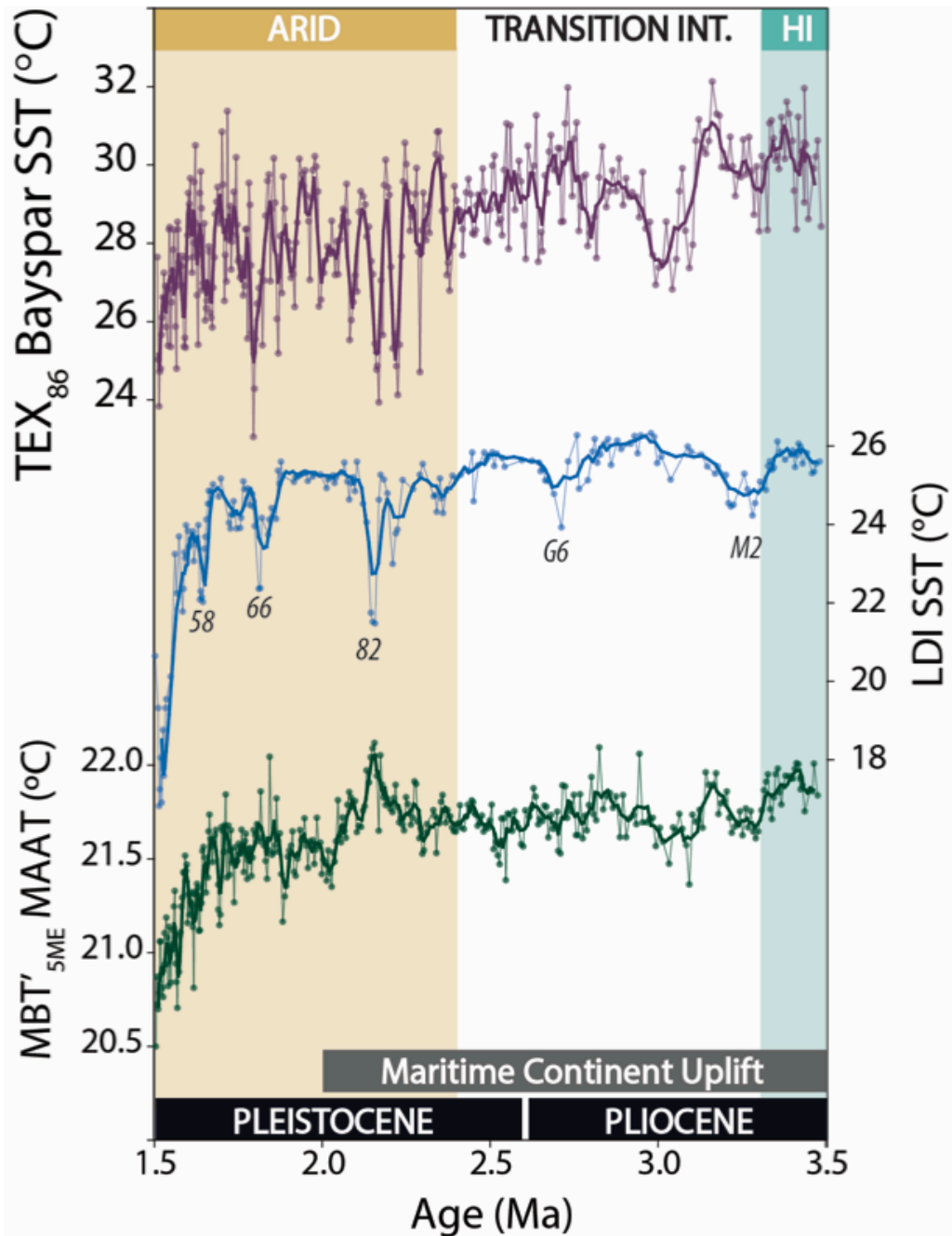


Figure 3.5: Temperature records without calibration error from Site U1463 vs. Age from 3.5-1.5 Ma. Shown above each record is a 5-pt mean data smooth (darker trend line). The upper curve shows the high-resolution BAYSPAR  $TEX_{86}$  record in light purple. The LDI record is shown as the middle curve in blue, and the  $MBT'_{5ME}$  record is shown in green below. Superimposed over data are the three hydrologic (brown for arid, white for transition, and teal for humid) intervals identified by Christensen et al. (2017).

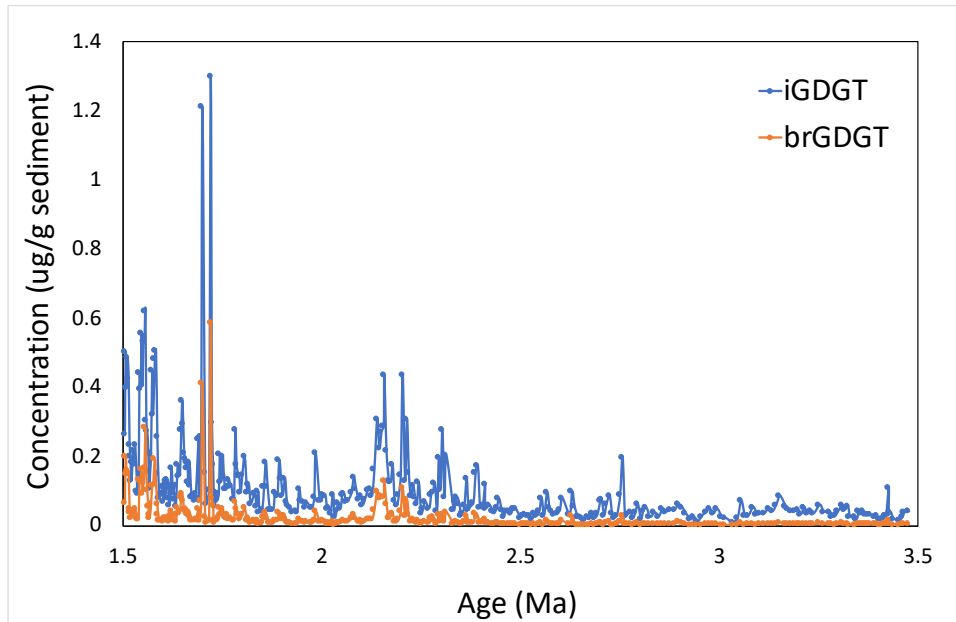


Figure 3.6: Concentrations in ug/g sediment of brGDGTs (orange) and iGDGTs (blue) from Site U1463 vs. Age from 3.5-1.5 Ma.

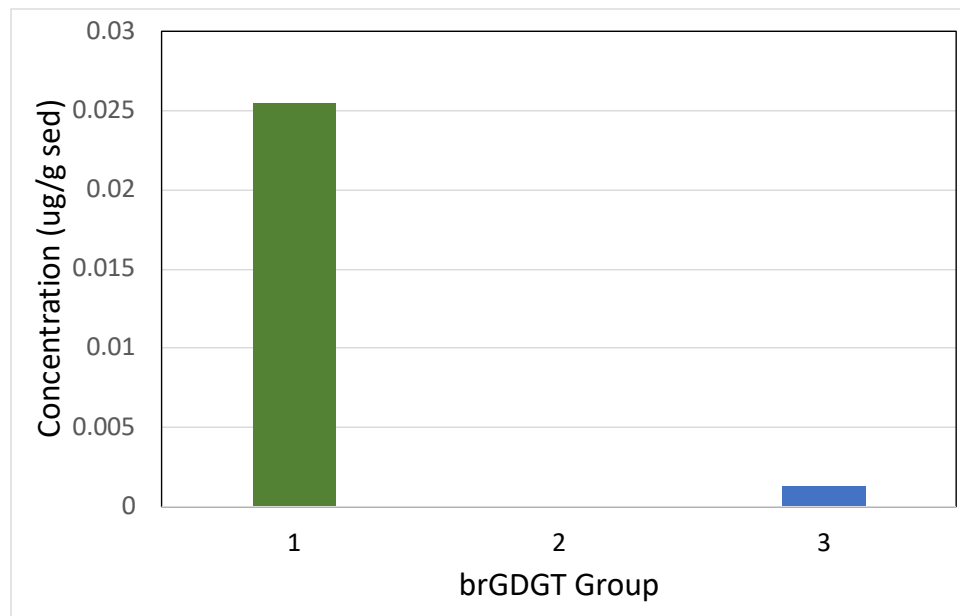


Figure 3.7: Average concentration in ug/g sediment of brGDGTs group 1-3 from 3.5-1.5 Ma. BrGDGT group 1 is shown in green, group 3 in blue, and group 2 absent.

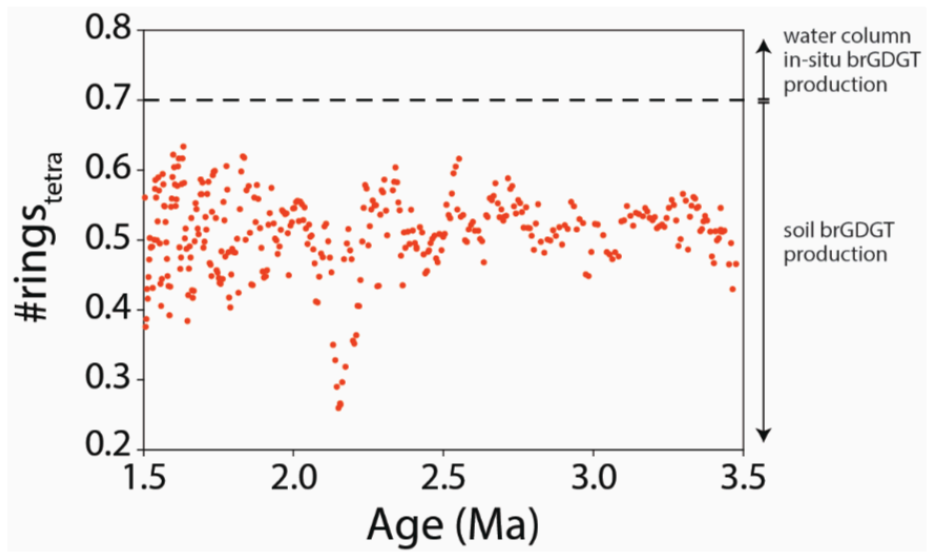


Figure 3.8: The #rings<sub>tetra</sub> index vs. Age from 3.5-1.5 Ma. Data points above 0.7 (dashed line) indicate water column in-situ brGDGT formation, and data points <0.7 indicate soil origin of brGDGTs.

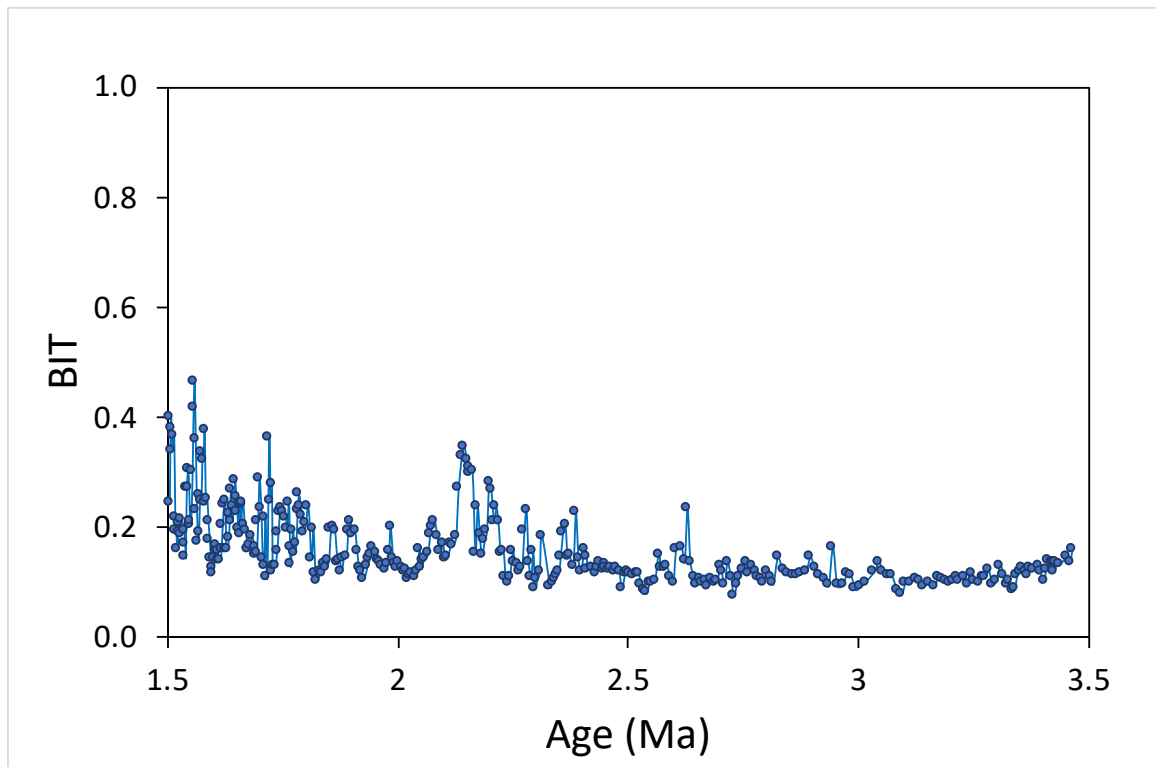


Figure 3.9: BIT index values, plotted from 0-1, vs. Age from 3.5-1.5 Ma.

## CHAPTER 4

### DISCUSSION

#### 4.1 SST Proxy Comparison

Average modern (1850-2015) SSTs off the coast of NW Australia range from ~27.5-29.5°C (COBE-SST2 dataset; Hirahara et al., 2013; Figure 4.1). These modern temperatures are in general agreement with mean TEX<sub>86</sub>-based SST values at Site U1463 of 28°C, although comparison to modern or Holocene sediments from this site would be more useful (Figure 4.2). The TEX<sub>86</sub> subT record yields a mean value of 25.5°C, which is about 2°C lower than modern mean SST values, and the LDI record yields the lowest mean reconstructed SST value of 24.4°C. The general agreement between modern SSTs and mean TEX<sub>86</sub>-based SSTs suggests that TEX<sub>86</sub> might reflect a surface rather than subsurface temperature signal at Site U1463. Although we cannot fully rule out that TEX<sub>86</sub> represents a shallow subsurface signal, or that the proxy may have varied between reflecting SST and subT on glacial-interglacial timescales, for the remainder of this discussion, TEX<sub>86</sub> will be considered a SST proxy at Site U1463.

It is important to consider that a contribution of iGDGTs from continental soils would have the potential to influence the applicability of TEX<sub>86</sub> as a SST proxy in this study. The average BIT index value across the entire study interval is 0.16, which does not reflect any significant contribution from continental soils (Figure 3.9). Interestingly, variability of BIT values increases slightly in amplitude in the younger half of the core from 2.5-1.5 Ma (Figure 3.9), which seems to coincide with the last stages of ITF shallowing and constriction from 5-2 Ma (Cane & Molnar,

2001), as well as an interval of sediment uplift spanning 2-1 Ma (Kominz et al., 2017), and a net increase in continental aridity observed by Christensen et al. (2017) from 2.4-1 Ma. This correlation suggests that ITF constriction as well as continental uplift and erosion may have contributed to soil input at Site U1463. Perhaps Site U1463 received an increase in both soil and iGDGT material across this period, however BIT values are overall lower than 0.4 (Figure 3.9), indicating that any continental iGDGT content is not enough to influence TEX<sub>86</sub>-based SST reconstructions. Reproducibility of results between different lab groups is an additional factor to consider when interpreting BIT data. Unlike TEX<sub>86</sub> measurements, which are quite reproducible between labs, BIT values can vary significantly by lab and depending on maintenance of respective mass spectrometers (Schouten et al., 2009). For example, BIT values measured in the Biogeochemistry Lab at UMass Amherst are ~0.1 higher than those measured at the NIOZ Royal Netherlands Institute for Sea Research (unpublished data from Castañeda). Therefore, BIT values measured in this study may be higher than would be measured by other labs, and are convincingly below concentrations suggestive of soil-based iGDGT production (0.8-0.9).

Similar to TEX<sub>86</sub>, the LDI can also be influenced by terrestrially sourced organic matter (Lattaud et al., 2017). Lattaud et al. (2017) determined that the C<sub>32</sub> 1,15 diol, which was previously identified in lakes and culture experiments (Volkman et al., 1992; Volkman et al., 1999; Rampen et al., 2014), can also be produced in-situ in river environments by freshwater-dwelling eustigmatophyte algae, and transported to offshore marine sites. While this particular diol is not

included in the calibration equation for the LDI (Equation 3), its presence could influence the relative abundances of diols in nearshore marine environments, as well as possibly introduce other diols produced by river-dwelling eustigmatophyte algae into the system (Lattaud et al., 2017). Similar to utilizing the BIT Index to constrain the relative input of GDGTs from continental soils, the fractional abundance of the C<sub>32</sub> 1,15 diol can be utilized as a proxy for river input of long chain diols into marine settings (Lattaud et al., 2017). At Site U1463, the fractional abundance of the C<sub>32</sub> 1,15-diol has an average value of 2.57%, and a maximum abundance of 6.45% across the entire study interval (Figure 3.3). Anything below 20% fractional abundance of C<sub>32</sub> 1,15-diol suggests low riverine input (Rampen et al., 2014; Lattaud et al., 2017), therefore it is reasonable to conclude that the LDI proxy reflects a marine SST signal and marine long-chain diol production.

Overall TEX<sub>86</sub> and LDI display somewhat similar patterns with higher temperatures in the Pliocene and cooling noted in the more recent part of the record after ~1.7Ma (Figure 3.4-3.5). Both records follow the trend of the global benthic δ<sup>18</sup>O stack (Figures 4.3-4.4)(Lisiecki & Raymo, 2005), which indicates that SSTs from Site U1463 have likely not been influenced significantly by selective degradation or lateral transport. It should be noted that if taking into consideration the relatively large calibration errors for both proxies, the LDI and TEX<sub>86</sub> SST records could have overlapping values. Differences in absolute reconstructed temperatures between the two proxies may be in part due to systematic calibration differences; however, other variables must be considered to explain trend differences.

In comparison to LDI, TEX<sub>86</sub> exhibits more variability from 3.5-1.5 Ma, and a cross plot with LDI reveals only a weak correlation ( $r^2=0.257$ ) (Figure 4.5). Presently the LDI record is at lower resolution (n=197 samples) than the TEX<sub>86</sub> record (n=369 samples). LDI-reconstructed SSTs (16.8-26.3°C) are lower in comparison to TEX<sub>86</sub> SSTs (32.0-24.1°C), which seems counterintuitive given that diatoms and other algae producing diols must reside within the photic zone and therefore reflect SST, whereas Thaumarchaeota perform chemosynthesis via ammonium oxidation and are not required to reside in the photic zone (Könneke et al., 2005; Beman et al., 2008; Newell et al., 2013; Hurley et al., 2016). One possible explanation for lower LDI values is that the long-chain diols at Site U1463 underwent oxic degradation within the sediments, which would cause a significant drop in C<sub>30</sub> 1,15-diol concentration and slightly less significant reduction in both C<sub>28</sub> 1,13-diol and C<sub>30</sub> 1,13-diol concentrations (Rodrigo-Gámiz et al., 2016). Decreases in total concentrations of C<sub>30</sub> 1,15-diol from oxic degradation would cause a decrease in LDI (Equation 3) and LDI reconstructed SSTs (Equation 4) (Rodrigo-Gámiz et al., 2016). Oxic degradation does not impact isoprenoid GDGTs, and therefore does not significantly influence TEX<sub>86</sub> SST reconstructions (Schouten et al., 2004). Therefore, the overall pattern of lower LDI-reconstructed SSTs may be a function of the susceptibility of diols, but not iGDGTs, to oxic degradation. However, oxic degradation of diols likely cannot account for all of the differences between these two proxies. For example, the LDI record shows more pronounced cooling than the TEX<sub>86</sub> record from 1.7-1.5 Ma (Figure 3.6-3.7), which may be due to increased upwelling, a shift in wind direction, or lateral transport of diols across this time

interval, although the exact reasons for such a pronounced cooling at this time are not clear.

Another possibility is that these two proxies reflect different seasonal growth temperatures. While initial calibration studies of  $\text{TEX}_{86}$  measured the strongest correlation with mean annual SST (Schouten et al., 2002), subsequent studies have found seasonal growth biases in specific locations (Herfort et al., 2006; Menzel et al., 2006; Leider et al., 2010; Castañeda et al., 2010; Hugué et al., 2011). When comparing LDI (Rampen et al., 2012),  $\text{TEX}^{\text{H}}_{86}$  (Kim et al., 2010) and  $\text{U}^{\text{K}}_{37}$  (Müller et al., 1998) records from the Murray Canyons Group area off the coast of southeastern Australia, Lopes dos Santos (2013) suggest that LDI likely captures a peak-warm season signal corresponding to austral summer months, whereas  $\text{TEX}^{\text{H}}_{86}$  likely captures a cooler winter signal. Furthermore, a study in the North Sea (Herfort et al., 2006) found that  $\text{TEX}_{86}$  SSTs were much lower than mean temperatures provided by the World Ocean Atlas (1998) and reflected a winter signal, which the authors attribute to a higher concentration of the compound crenarchaeol and blooms of *Thaumarchaeota* during winter months (Wuchter et al., 2006).  $\text{TEX}_{86}$  has also shown a summer-season bias in Mediterranean marine sediments (Menzel et al., 2006; Leider et al., 2010; Hugué et al., 2011).  $\text{TEX}_{86}$  seems to be most correlated with mean annual temperature in regions without preferential growing season of *Thaumarchaeota* (Kim et al., 2008). At Site U1463,  $\text{TEX}_{86}$  SSTs are higher than LDI SSTs, suggesting that a summer seasonal bias may be occurring. However, it seems unlikely that a significant seasonal bias is the most likely explanation here given that the sample resolution at Site U1463 is  $\sim 5$  ka and that the record spans 2 million

years, during which time significant climatic and oceanographic changes in the region have occurred. On such long timescales it seems more plausible that a process such as oxic degradation or changes in preservation may have a more pronounced influence on the different proxies. Oxic degradation influences only LDI, however TEX<sub>86</sub> is sensitive to thermal maturity of sediments (Schouten et al., 2004). Most notably, iGDGTs I-IV degrade when sediments reach temperatures between 240-300°C (Schouten et al., 2004); however sediments from Site U1463 were not exposed to temperatures of this magnitude at any point.

We note that we cannot conclusively rule out the possibility that other non-thermal factors including a seasonal growth bias, differences in light limitation, growth rate or nutrient supply are responsible for the offset between LDI and TEX<sub>86</sub> temperatures at Site U1463. The effects of light limitation and nutrient supply have been measured in long chain alkenone culture experiments (Prahl et al., 2005; Placencia et al., 2010), however, the effects of these non-thermal factors are not as well constrained on diol-producing diatoms and microalgae, or on marine Thaumarchaeota. Despite the environmental factors that may contribute error to each of these proxies, when analyzed together, both LDI and TEX<sub>86</sub> records indicate substantial cooling at 1.7 Ma at Site U1463 (Figures 3.6-3.7).

#### **4.2 Site U1463 vs. Nearby Sites**

In the following discussion, we compare our new LDI and TEX<sub>86</sub> SST records from Site U1463 to other Pacific and Indian Ocean SST records on either side of the ITF in order to constrain variability in temperature both at the inlet and outlet of this critical ocean gateway across the Plio-Pleistocene.

### 4.2.1 Indian Ocean Records

To date, two main studies have examined past ITF variability from sites in the Indian Ocean. The Site 214 Mg/Ca SST record (Karas et al., 2009; Figure 1.4) extends back to 5.5 Ma, while the record from Site 763A (Karas et al., 2011a) extends back to 6 Ma; however, neither of these studies reconstruct SSTs younger than 2 Ma (Figure 4.7). Therefore, this project provides the first Indian Ocean SST record examining ITF variability from 2-1.5 Ma. Notably the strongest cooling signal observed from Site U1463 occurs within this new, youngest portion of the record (Figure 4.7). SSTs at Site 214 remained relatively warm and stable across the entire study interval from 5.5-2 Ma, however, Karas et al. (2011a) observe surface cooling at Site 763A by 2-3°C beginning at 3.3 Ma. The authors attribute this cooling to a switch in ITF source waters and a reduction of Leeuwin Current intensity. It is important to note that within the context of the results from Christensen et al. (2017), SSTs at Site 763A increase at the onset of the humid interval (5.5 Ma), and decrease at the end of the humid interval (3.3 Ma)(Figure 4.7). In partial agreement with the conclusions of Karas et al. (2011a), the constriction of the ITF and the emergence of the Maritime Continent 5-2 Ma likely caused partial surface water cooling at Site 763A at 3.3 Ma. However, the dramatic cooling signal at 1.7 Ma from Site U1463 suggests that the final transition from South Pacific to North Pacific source waters may have occurred later in the record during the arid interval, post-Maritime Continental uplift.

### **4.2.2 Pacific Ocean Records**

While SST cooling is observed at Site U1463 from 1.7-1.5 Ma, SST warming is observed across this period in the western equatorial Pacific at Site 806 (Wara et al., 2005)(Figure 4.8). Site 806 is located near the inlet of the ITF and the return flow of the Halmahera Eddy (Figure 1.2). When compared with the cooling signal near the outlet of the ITF at Site U1463, the onset of warming at Site 806 at 1.7 Ma supports the hypothesis that the final switch in ITF source waters occurred at 1.7 Ma and caused South Pacific warm waters to divert from the entrance of the ITF via the Halmahera Eddy back into the South Pacific Ocean.

It does not seem likely that the 2-3°C SST cooling signal at 3.3 Ma from Site 763A (Karas et al., 2011a) reflects a complete shift in ITF source waters because no warming trend, which would reflect return flow of South Pacific warm waters via the Halmahera Eddy, is observed at Site 806 at that time (Figure 4.8). Overall, these findings offer an alternate hypothesis compared to Hypothesis 1 because cooling in Site U1463 records does not reflect cooling in agreement with the results of Karas et al. (2011a). Instead, results from this study suggest that ITF source waters transitioned later at 1.7 Ma, and prompted not only a cooling signal at Site U1463, but also a warming signal at Site 806 (Wara et al., 2005).

### **4.3 Zonal and Meridional SST Gradients**

The geographic location of Site U1463 between Site 722 in the northwest Indian Ocean and Site 806 in the western Pacific Ocean (Figure 1.6) makes it an ideal study site with which to produce both a meridional and zonal SST gradient from 3.5-1.5 Ma. The amplitude of SST difference between Site U1463 (LDI) and Site

806 increases significantly near the end of the arid interval, likely corresponding to the dramatic cooling event observed at Site U1463 at 1.7 Ma (Figure 4.9, lower). The zonal SST difference calculated with the  $TEX_{86}$  record shows increased variability between the two sites across the arid interval (Figure 4.9, upper). Furthermore, the  $TEX_{86}$ -based zonal gradient reflects a negative difference in SSTs from ~1.8-1.5 Ma, which indicates that Site 806 SSTs exceeded those at Site U1463 during this time. This negative trend in SST difference (Figure 4.9 upper and lower) supports Hypothesis 2.

The meridional SST gradient between Site 722 (Herbert et al., 2010) and Site U1463 (Figure 4.10) offers new insights into the timing of warm pool constriction relative to cooling at Site U1463. The net amplitude of SST difference in the  $TEX_{86}$ -based curve increases slightly in the Pleistocene relative to the Pliocene (Figure 4.10, upper), however an overall shift in SST difference is more pronounced in the LDI-based curve by 1.7 Ma (Figure 4.10, lower). Results differ significantly from those of Brierley et al. (2006), who identified a distinct shift in SST gradient culminating at 2 Ma. Therefore, LDI-based differences in SSTs may be reflecting the cooling signal at Site U1463 rather than a constriction of an Indian Ocean equatorial warm pool, which addresses Hypothesis 3.

The Pacific Ocean meridional SST gradient findings of Brierley et al. (2009) and Brierley and Fedorov (2010), when compared to the cooling record at Site U1463, offers an alternate explanation for cooling at 1.7 Ma near the outlet of the ITF different from Hypothesis 1. The temperature difference between Sites 846 and 1012 stabilized by 2 Ma according to Brierley et al. (2009), just before the onset of

sharp cooling at 1.7 Ma at Site U1463. Interestingly, the zonal SST gradient between Site 806 and Site 847 (Wara et al., 2005) also increased at 1.7 Ma, potentially in response to this constriction of the WPWP at 2 Ma (Brierley et al., 2009). An amplified meridional SST gradient at 2 Ma (Figure 1.7) would cause North Pacific Ocean waters to cool. That cooling signal caused by constriction of the meridional SST gradient at 2 Ma may explain the strong cooling observed at Site U1463 at 1.7 Ma.

It is difficult to determine exactly which hypothesis correctly explains the cooling signal observed at Site U1463 at 1.7 Ma. The revision to Hypothesis 1 argues that the final switch from South Pacific to North Pacific source waters occurred near 1.7 Ma rather than at 3.3 Ma as suggested by Karas et al. (2011a) (Explanation 1). Conversely, the constriction of the WPWP pool at 2 Ma suggests an alternative explanation (Explanation 2) for cooling at 1.7 Ma at Site U1463 via an increased cooling of North Pacific source surface waters entering the ITF. In order to determine which of these scenarios is more likely, variability around other ocean gateways across the Plio-Pleistocene must be considered, and SST data from Site U1463 must be compared to global records at various latitudes from 3.5-1.5 Ma.

#### **4.4 Central American Seaway and Bering Strait Variability**

Variability of other ocean gateways in addition to the ITF likely contributed to shifts in global thermohaline circulation across the Plio-Pleistocene, and therefore must be considered when interpreting SST data from Site U1463. Several studies have constrained the timing of the constriction of the Central American Seaway (CAS) across the Pliocene, and have correlated the formation of the Isthmus

of Panama land bridge to shifts in global climate. Both model and faunal exchange studies suggest that the CAS was closed by 4-3 Ma (Coates & Stallard, 2013; Marshall et al., 1982; Marshall, 1988), however considerable changes in thermohaline circulation associated with the progressive constriction of this gateway occurred prior to final closure (Haug & Tiedemann, 1998). Haug and Tiedemann (1998) examined  $\delta^{13}\text{C}$  of epifaunal benthic foraminiferal species *Cibicidoides wuellerstorfi* from ODP Site 999 (12°44'N, 78°44'W)(Figure 1.6), located in the Colombian Basin between 5.3-2.0 Ma, and identified increasing values from 4.6-3.6 Ma, which they attribute to a strengthening of deep water ventilation at this time (McCorkle & Keigwin, 2010; Kroopnick, 1985). By 3.6 Ma,  $\delta^{13}\text{C}$  values at Site 999 were comparable to  $\delta^{13}\text{C}$  values measured at east Atlantic Site 659 (18°05'N, 21°2'W; Tiedemann et al., 1994)(Figure 1.6). Their results point to an increase in deep-water ventilation via NADW in the Caribbean Sea, a strengthening of the Gulf Stream and an increase in moisture transport to high latitudes from 4.6-3.6 Ma due to the constriction and shoaling of the CAS (Haug & Tiedemann, 1998). Previous studies have correlated the emergence of the Isthmus of Panama to the onset of Northern Hemisphere Glaciation (NHG)(Hay, 1996) at 2.82 Ma (Bartoli et al., 2005), however, Haug and Tiedemann (1998) argue that the closing of the CAS was not the primary cause for NHG, but it was a key factor involved in providing moisture to high latitudes required for the onset of glaciation at a later time.

In support of these conclusions, SST analyses from Site 1241 near the outlet of the CAS (5°5'N, 86°27'W)(Figure 1.6) indicate a correlation between decreasing SSTs and an increase in AMOC from 4.8-4.0 Ma (Steph et al., 2006; Steph et al.,

2010). Furthermore, Karas et al. (2017) identify a reduced meridional SST gradient between 4.8-3.8 Ma in response to warming at North Atlantic Site 552A (56°02'N; 23°13'W)(Figure 1.6) and cooling at southern high latitude site 516A (30°17'S; 35°17'W) (Figure 1.6). The authors attribute this reduced SST gradient to a strengthened AMOC signal associated with the constriction of the CAS (Karas et al., 2017). These studies indicate that significant shifts in global thermohaline circulation associated with the constriction of the CAS likely occurred in the early Pliocene.

Therefore in summary, the closure of the CAS likely occurred between 4-3 Ma (Coates & Stallard, 2013; Marshall et al., 1982; Marshall, 1988), however, the main changes in ocean circulation associated with the constriction of the CAS most likely occurred earlier in the record during the early Pliocene (Haug & Tiedemann, 1998; Steph et al., 2006; Steph et al., 2010; Karas et al., 2017). Therefore, the constriction of the CAS is not likely a dominant forcing mechanism influencing SSTs at Site U1463 from 3.5-1.5 Ma.

Similar to the constriction of the CAS, the geologic timing of the opening of the Bering Strait is important to consider in order to constrain shifts in thermohaline circulation across the Plio-Pleistocene. Despite significant debate, the first opening of the Bering Strait likely occurred in the latest Miocene possibly between 5.5-4.8 Ma (Marincovich Jr. & Gladenkov, 1999; Forte & Mitrovica, 2016). Marincovich Jr. and Gladenkov (1999) propose that water flowed from the Arctic into the Bering Sea during initial stages of opening, and switched current direction upon closure of the CAS and intensification of AMOC (Haug & Tiedemann, 1998).

The Bering Strait was likely open during the entire study interval from 3.5-1.5 Ma, and the direction of flow through this ocean gateway possibly flipped in response to changes in the CAS as previously discussed. Therefore, SST variability observed at Site U1463 is likely not a response to shifts in either Bering Strait or Panama Seaway behavior.

#### **4.5 Site U1463 vs. Global SST Records**

While the constriction of the CAS and the opening of the Bering Strait may not have forced SST changes at Site U1463 from 3.5-1.5 Ma, it is important to identify other relevant climate forcing mechanisms that may have influenced SSTs. The following discussion will compare SSTs from Site U1463 to those from sites at both high-latitude and low-latitudes, in order to identify any similarities between records that will help elucidate climate forcing changes at Site U1463. In particular, comparisons will focus on the cooling event identified in the TEX<sub>86</sub> record at 1.7 Ma, as well as the cooling observed during MIS Stages G18, G20, G22 and MIS M2 (Figure 4.4b).

##### **4.5.1 Cooling at 1.7 Ma**

As previously discussed, the TEX<sub>86</sub> and LDI SST records indicate significant cooling at 1.7 Ma, which may be a reflection of either (Explanation 1) the final transition to cold North Pacific source waters entering the ITF or (Explanation 2) an increase in the meridional SST gradient by 2 Ma and subsequent cooling of ITF source waters (Brierley et al., 2009). In order to better constrain which explanation is more probable, cooling at Site U1463 is compared to that observed at ODP Sites 882 and 1090 (Figure 1.6; Martínez-García et al., 2010), Site 847 (Figure 1.6; Wara

et al., 2005), and Site 593 (Figure 1.6; McClymont et al., 2008)(Figure 1.6) across the Plio-Pleistocene (Figure 4.11).

Martínez et al. (2010) utilized the  $U_{37}^{k'}$  index to reconstruct SSTs from both ODP Site 882 in the North Pacific and ODP Site 1090 in the South Atlantic over the past 3.5 Ma (Figure 1.6; Martínez-García et al., 2010)(Figure 4.11). Notably, the authors identified distinct cooling (4-5°C) at both Sites 882 and 1090 (i.e., at both southern and northern sub-polar latitudes) from ~1.8-1.2 Ma. The authors suggest that this cooling reflects an increase in polar sea ice extent across this interval, and a cooling of subpolar waters overall. Their findings indicate a net increase in meridional SST gradient (Brierley et al., 2009) due to pronounced cooling of subpolar waters at 1.8 Ma. Furthermore, Martínez-García (2010) point out the remarkable timing between the marked decrease in subpolar temperatures at Site 882 and 1090, the distinct drop in temperatures observed at Site 847 at 1.8 Ma (Figure 4.11), and the corresponding increase in zonal SST gradients across the Pacific (Wara et al., 2005). These lines of evidence suggest that cooling at Site U1463 at ~1.7 Ma could likely be in response to pronounced cooling by up 4-5°C to of North Pacific source waters entering the ITF (i.e. from Site 882) and a net increase in meridional SST gradients globally (Figure 1.7).

Evidence for SST cooling at 1.8 Ma is also recorded at Site 593 (Figure 1.6 and Figure 4.11), located in the Tasman Sea off the coast of Southeast Australia, close in latitude to the Subtropical Front (STF) at the edge of the Antarctic Circumpolar Current (ACC)(McClymont et al., 2016). SSTs were reconstructed at Site 593 by applying the  $U_{37}^{k'}$  Index to sediments spanning the last 3.5 Ma, and

indicate high latitude (comparable to Site 1090) climate changes across this interval. Similar to Site 1090, Site 593 is in contact with Antarctic polar waters via the STF, and is therefore sensitive to expansions of polar water extent across the Plio-Pleistocene during periods of expanded sea-ice extent (Woodard et al., 2014). McClaymont et al. (2016) find that at 1.8 Ma, cooling at Site 593 relative to warming at Site 806 (Wara et al., 2005; Figure 4.8) produces an increase in meridional SST gradient in the South Pacific (McClymont et al., 2016). The timing of this increase in meridional SST gradient between Sites 806 and Site 593 at ~1.8 Ma corresponds closely to the increase in the North Pacific meridional SST gradient between Sites 846 and 1012 (Brierley et al., 2009), and to the increase in the zonal SST gradients between Site 806 and Site 847 (Wara et al., 2005).

Overall, SST records from Sites 593, 882, 1090, and 847 all indicate a drop in SSTs and a corresponding increase in a meridional SST gradient at 1.8 Ma, which aligns closely with cooling at Site U1463 from 1.7-1.5 Ma in both  $TEX_{86}$  and LDI SST records. This strong agreement between records provides compelling evidence for Explanation 2, i.e. that source waters entering the ITF cooled in response to an increase in meridional SSTs from 1.8 Ma onward.

The alternate explanation, i.e., Explanation 1 that cooling at 1.7 Ma corresponds instead to the final tectonic constriction and shallowing of the ITF, is supported by the SST warming signal identified at Site 806 from 1.7-1.5 Ma (Figure 4.8). As previously discussed, Site 806 is located in the western equatorial Pacific Ocean near the inlet of the ITF (Figure 1.2). Notably, at this site, the South Equatorial Current (SEC) is diverted from the entrance to the ITF back into the Pacific via the

Halmahera Eddy (Figure 1.2A). Therefore, warming at Site 806 (Figure 4.8) suggests that South Pacific waters traveling to the ITF were diverted back into the Pacific due to a final switch in source waters entering the ITF at 1.7 Ma. While compelling, this hypothesis contradicts prior hypotheses made by Karas et al. (2009) and Karas et al. (2011a) that the final switch in source waters occurred much earlier in the record, i.e., by 3.3 Ma (Karas et al., 2011a) or sometime between 3.5-2.95 Ma (Karas et al., 2009). The conclusions of these two studies are also supported by a temperature record from DSDP Site 590B in the South Pacific. Karas et al. (2011b) produced a Mg/Ca based SST record from DSDP Site 590B (Figure 1.6), in order to track shifts in the Tasman Front (TF) and intensity of the East Australian Current (EAC) system across the Plio-Pleistocene. From 3.5 to ~2.6 Ma, the authors identify slight cooling by ~1°C at Site 590B, preceded by a warming signal from 3.8-3.5 Ma. The authors hypothesize that this earlier warming signal may reflect an increase in EAC intensity and southward migration of the TF caused in part by the constriction of the ITF from 5-2 Ma (Karas et al., 2011b; Godfrey, 1996). While the authors did not identify a large shift in SST from 3.5-3.0 Ma, their subT record from Mg/Ca of *G. crassaformis* analyses does indicate significant subsurface cooling from ~14-10°C across this interval. The authors suggest that the subsurface cooling at Site 590B could reflect a change in intensity, geographic extent or overall temperature of Subantarctic Mode Water (SAMW) reaching the study site. They argue that shifts in SAMW water extent and cooling of southern latitude ocean water may correspond to the constriction of the ITF and the switch from South Pacific warm waters to North Pacific cold waters entering the Indian Ocean and distributing to other ocean basins. Together, these

three studies do strongly refute Explanation 1, and suggest an early switch in ITF source waters long before 1.7 Ma. Explanation 2 therefore seems most convincing, that a global shift in meridional SST gradients caused pronounced cooling at Site U1463 at 1.7 Ma, in agreement with cooling in other records at both high and low latitudes.

#### **4.5.2 MIS M2 and Pronounced Cooling During MIS G18, G20 and G22**

While LDI and TEX<sub>86</sub> records from Site U1463 seem to record regional shifts in climate associated with ITF variability, they also reflect global climate signals of glacial/interglacial cyclicality. From 2.5-1.5 Ma, LDI captures MIS Stages 52, 55, 58, 63, 66, 82, 84, 89, and 92 (Figure 4.3a). Notably temperatures remain relatively constant at ~25°C from 2.10-1.87 Ma, between MIS Stages 80-68. This temperature plateau may indicate that reconstructed values approach the calibration limit of the proxy (27°C). The plateau most likely does not reflect an actual climate signal, because glacial/interglacial cyclicality is captured by the TEX<sub>86</sub> SST record across this same interval (Figure 4.4a). However, no significant changes in fractional abundance of diols are evident from 2.10-1.87 Ma, corresponding to the depth interval between 207-225 mCCFS-A (Figure 3.2). Future lab work will increase the temporal resolution of the LDI record and hopefully provide answers as to the lack of glacial-interglacial cyclicality observed across this interval. The TEX<sub>86</sub> record shows pronounced cooling during glacial cycles at MIS 64, 78, 82, 84, 88, and 92 from 2.5-1.5 Ma, and overall a higher variability in SSTs associated with glacial-interglacial cyclicality.

From 3.5-2.5 Ma, the LDI record captures MIS Stages G6, G7, K1, M2, and MG5 (Figure 4.3b). LDI-based SSTs indicate that the lowest temperatures across this interval occur at 3.3 Ma and 2.7 Ma, in line with MIS Stages M2 and G6, respectively. MIS G6 has been identified as the onset period for Northern Hemisphere Glaciation (NHG) at ~2.7 Ma, due to a rise in amplitude of obliquity cycles every 41-ka (Ruggieri et al., 2009; Maslin et al., 1998) and an increase in number of ice-rafted debris deposits from the Greenland, North American, and Scandinavian ice sheets (Flesche Kleiven et al., 2002; Maslin et al., 1998). Slightly older in the record, MIS M2 is the most prominent glacial cycle recorded prior to the onset of NHG at 2.7 Ma (Lisiecki & Raymo, 2005), and is considered to be a first “failed attempt” at NHG at ~3.3 Ma (Haug & Tiedemann, 1998). A review paper by Schepper et al. (2014) asserts that growth of the Antarctic ice sheet during MIS M2 (McKay et al., 2012) could have been in part due to the constriction of the ITF and the corresponding decrease in warm water input to both the Indian Ocean and higher latitude Subantarctic Mode Waters (SAMW) (Karas et al., 2011b). Indian Ocean subsurface cooling from 3.5-2.95 Ma at Site 214 (Karas et al., 2009) and surface cooling by 3.3 Ma at Site 763A (Karas et al., 2011a) seems to align with the timing of MIS M2 at 3.3 Ma, and this agreement suggests that the primary switch in source waters entering the ITF occurred around this time and influenced high latitude temperatures. These conclusions provide further evidence against Explanation 1, that the primary switch in source waters entering the ITF occurred far later in the Site U1463 record at 1.7 Ma.

$\delta^{18}\text{O}$  data from the LRO4 global benthic stack indicates that MIS Stages G18, G20, and G22 were smaller glacial events relative to MIS M2 (Lisiecki & Raymo, 2005). However, from 3.5-2.5 Ma, the  $\text{TEX}_{86}$  SST record shows increased cooling during these three glacial periods relative to MIS M2 (Figure 4.4b). Conversely, and as previously mentioned, the LDI record exhibits the most pronounced cooling signal during MIS M2 prior to onset of iNHG at MIS G6 (Figure 4.3b). It remains unclear why the  $\text{TEX}_{86}$  record reflects more intense cooling after MIS M2, and it is difficult to conclusively associate more pronounced MIS Stages G18, G20, and G22 to a climate signal at Site U1463 because the LDI record does not show the same results. No significant change in iGDGT concentration is detected between ~3.02-2.97 Ma (G20- G18) (Figure 3.3), however, perhaps these cooler temperatures could be explained by a series of upwelling events that brought deeper dwelling Thaumarchaeota to the surface at Site U1463.

Overall, both  $\text{TEX}_{86}$  and LDI records closely track glacial-interglacial variability, thereby in part addressing Hypothesis 7 of this study. In order to fully test this hypothesis, SST records must be compared to the  $\text{MBT}'_{5\text{ME}}$  continental mean annual air temperature (MAAT) record from Site U1463. Furthermore, analyses of both SST and continental MAAT records from this study can test the hypotheses proposed by Christensen et al. (2017) that continental hydrology shifted through three critical intervals (arid, transition and humid) in response to the constriction of the ITF from 5-2 Ma (Cane & Molnar, 2001).

#### 4.6 Continental Air Temperatures and Offshore Cooling

According to the Australian Government Bureau of Meteorology, mean temperatures in Northwest Australia from March 2017 through February 2018 range from ~27-30°C, maximum temperatures range from ~33-36°C and minimum temperatures range from ~18-24°C. At Site U1463, average MAATs reconstructed from the MBT'<sub>5ME</sub> proxy spanning 3.5-1.5 Ma vary between 20.5-22.0°C. These paleotemperatures fall within the range of modern NW Australian minimum average air temperatures. Without considering calibration error, NW Australian air temperatures may have only varied by ~1.5°C from 3.5-1.5 Ma. Calibration error for the MBT'<sub>5ME</sub> proxy is relatively high at ± 4.6°C (Figure 3.6; C. De Jonge et al., 2014a). While calibration error overall seems significant, reconstructed MAATs exhibit very low overall variability (~1.5°C) across the study interval, making it unlikely that a shift in calibration would significantly alter these values. Notably, samples from Site U1463 are unique because they lack Group II brGDGTs. Therefore, caution must be exercised when interpreting absolute values of reconstructed MAATs from this study site, however absolute trends produced in this record are robust.

MAAT values are relatively high and stable for most of the Pliocene and into the early Pleistocene, and pronounced cooling begins at ~1.7 Ma, in agreement with cooling observed in both LDI and TEX<sub>86</sub> records [Hypothesis 5]. A cross plot between TEX<sub>86</sub> and MBT'<sub>5ME</sub> reveals a very weak correlation of 0.12 (Figure 4.12), however a cross plot with LDI reveals a slightly stronger correlation of 0.37 (Figure 4.13). Similar to both LDI and TEX<sub>86</sub> records, the MBT'<sub>5ME</sub> proxy seems to capture glacial/interglacial cyclicity, although with several notable exceptions [Hypothesis

7]. Low air temperatures correspond to increased LRO4  $\delta^{18}\text{O}$  values during MIS Stages 54, 64, 100, G3, G6, G10, G20, K2, KM2, and M2 (Figure 4.14). However, elevated air temperatures between ~2.4-2.0 Ma seem to closely compare to  $\delta^{18}\text{O}$  values measured by Christensen et al. (2017) across this interval (Figure 4.15). This strong agreement between records suggests that a spike in humidity at ~2.1 Ma corresponds to an increase in continental MAAT. Despite this humid excursion at 2.1 Ma, overall cooling in the MAAT record falls within the arid interval identified by Christensen et al. (2017). Therefore, decreases in NW Australian continental air temperatures may contribute to an increased continental aridity signal from 2.4-1.0 Ma [Hypothesis 6].

The SST and MAAT findings from this study are used to test the hypothesis proposed by Christensen et al. (2017), which argues that the constriction of the ITF and the switch from warm South Pacific to cool North Pacific source waters caused a shift from humid to arid conditions in Northwest Australia. Interestingly and as previously discussed, the sharp cooling event observed at ~1.7 Ma in all three temperature records from Site U1463 most likely reflects an overall increase in meridional SST gradients, as observed in numerous other SST records (Figure 4.11). Therefore, the final transition in source waters due to ITF constriction and shallowing probably occurred earlier in the record between 3.5-2.95 Ma in accordance with the findings of Karas et al. (2009) and Karas et al. (2011a). This switch in source waters seems to coincide with the three hydrologic intervals identified by Christensen et al. (2017)(Figure 1.4). Notably however, aridity values

from 1.7-1.5 Ma may partially reflect an increase in meridional SST gradients across this interval and a resulting drop in ITF source water temperatures.

A study by Snidermen et al. (2016) analyzed pollen records from speleothems preserved in several caves across Nullarbor Plain in southern Australia, in order to constrain shifts in mean annual precipitation from the late Miocene through the Pliocene. The authors detect high levels of precipitation during the late Miocene, however from ~3.45-3.00 Ma, they identify no pollen records in their speleothem samples (Sniderman et al., 2016). They suggest that this drop in pollen records could be a result of a sampling effect, however, they also tentatively suggest a correlation between absence of pollen data and SST cooling observed by Karas et al. (2011a) from 3.5-2.95 Ma (Figure 1.4). Perhaps precipitation declined significantly in response to SST cooling at Site 763A in other regions of continental Australia, but this explanation does not seem as probable given that Northwest Australia was still relatively humid by 3.45Ma (Figure 1.8). Without direct mean annual precipitation data from NW Australia spanning this period or  $\delta D$  isotopic data of leaf waxes preserved at Site U1463, it is difficult to determine the exact shifts in hydrology associated with nearshore cooling.

Monthly Means of Global Sea Surface Temperature

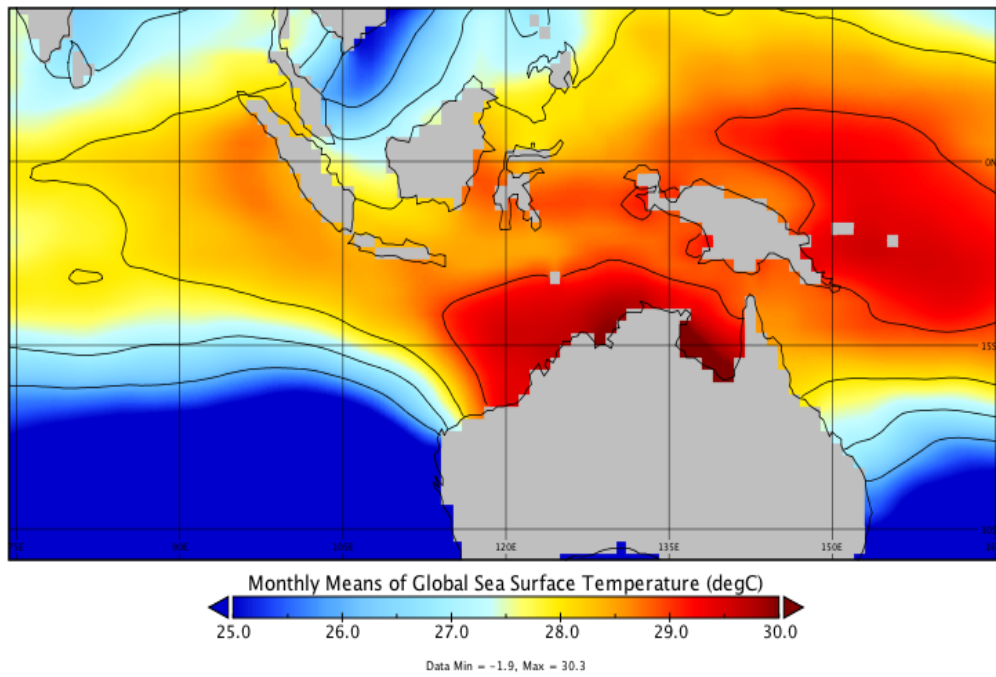


Figure 4.1: Modern Indo-Pacific SST map. Produced with Panoply using data from: COBE-SST2 data (Hirahara et al., 2013) provided by the NOAA/OAR/ESRL PSD, Boulder, Colorado, USA, from their Website at <https://www.esrl.noaa.gov/psd/> <https://www.esrl.noaa.gov/psd/data/gridded/data.cobe2.html>

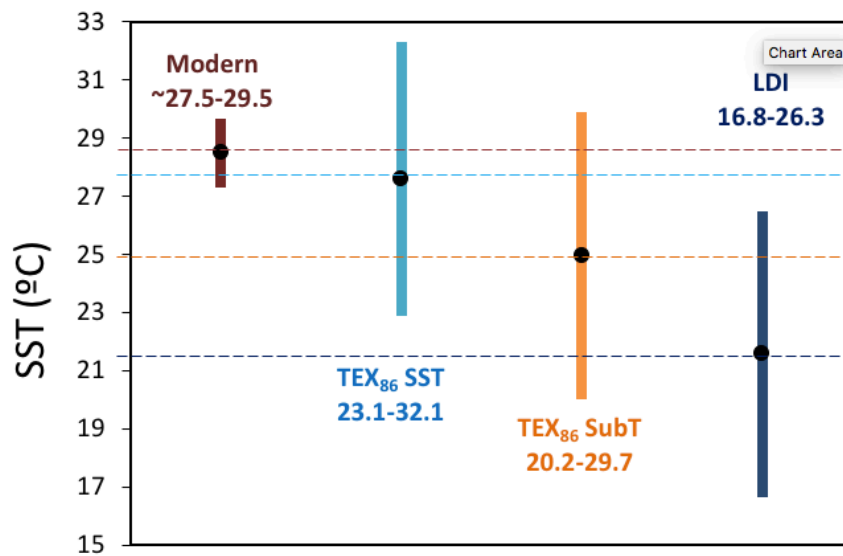


Figure 4.2: Modern SSTs (red) relative to Site U1463 LDI (dark blue) and TEX<sub>86</sub> SST and subT paleodata (light blue and orange, respectively).

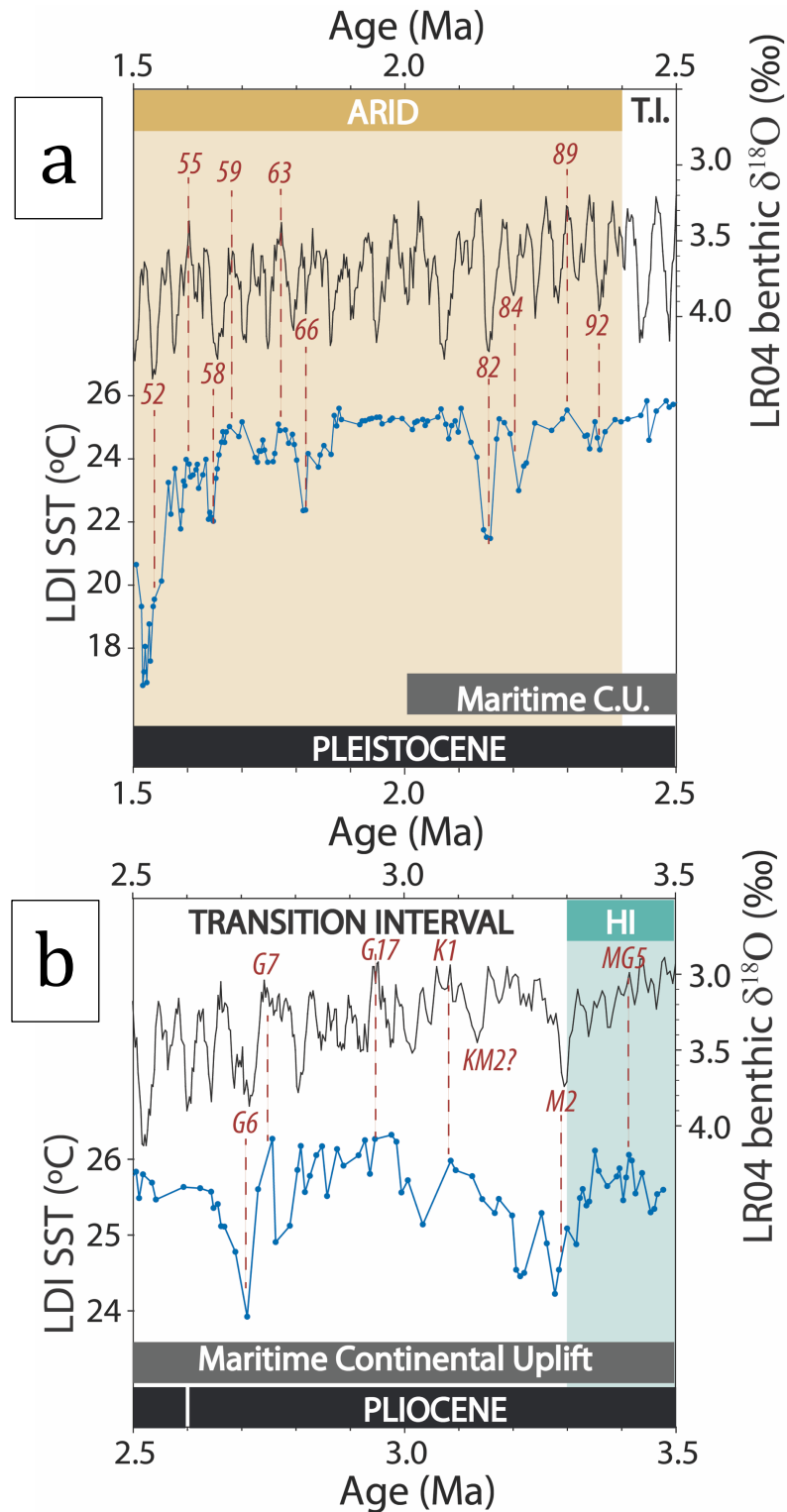


Figure 4.3: LDI SSTs ( $^{\circ}\text{C}$ ) versus the LR04 global benthic  $\delta^{18}\text{O}$  stack from **a)** 2.5-1.5 Ma and **b)** 3.5-2.5 Ma. Superimposed over data are the three hydrologic (brown for arid, white for transition, and teal for humid) intervals identified by Christensen et al. (2017).

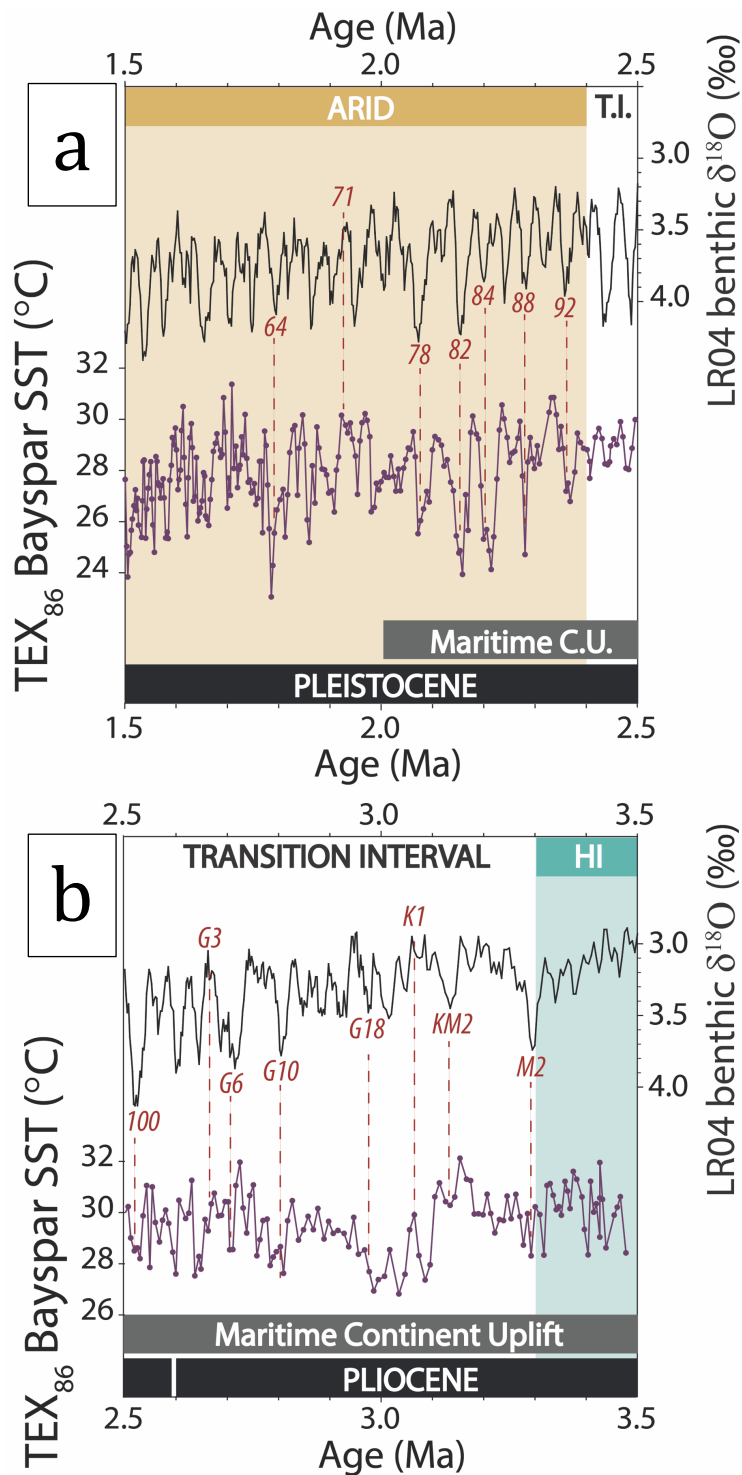


Figure 4.4: TEX<sub>86</sub> SSTs (°C) versus the LR04 global benthic δ<sup>18</sup>O stack from **a)** 2.5-1.5 Ma and **b)** 3.5-2.5 Ma. Superimposed over data are the three hydrologic (brown for arid, white for transition, and teal for humid) intervals identified by Christensen et al. (2017).

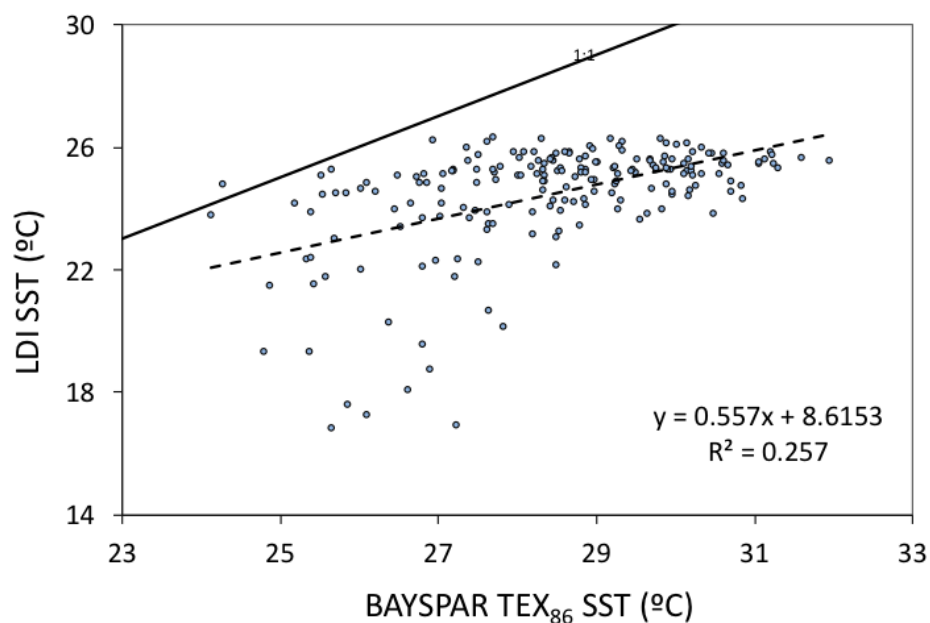


Figure 4.5: Cross-plot of LDI SSTs (°C) versus BAYSPAR TEX<sub>86</sub> SSTs (°C). The solid black line indicates a 1:1 cross-plot ratio, and the black dashed line indicates the linear best fit of the data.

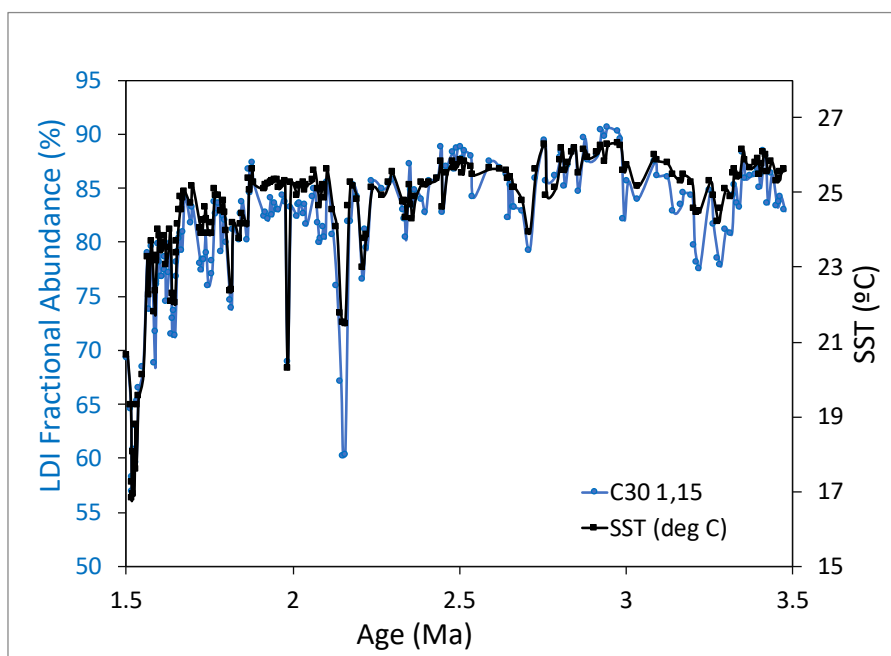


Figure 4.6: % fractional abundance of the C<sub>30</sub> 1,15 diol (blue) and LDI-SST (°C)(black) from 3.5-1.5 Ma.

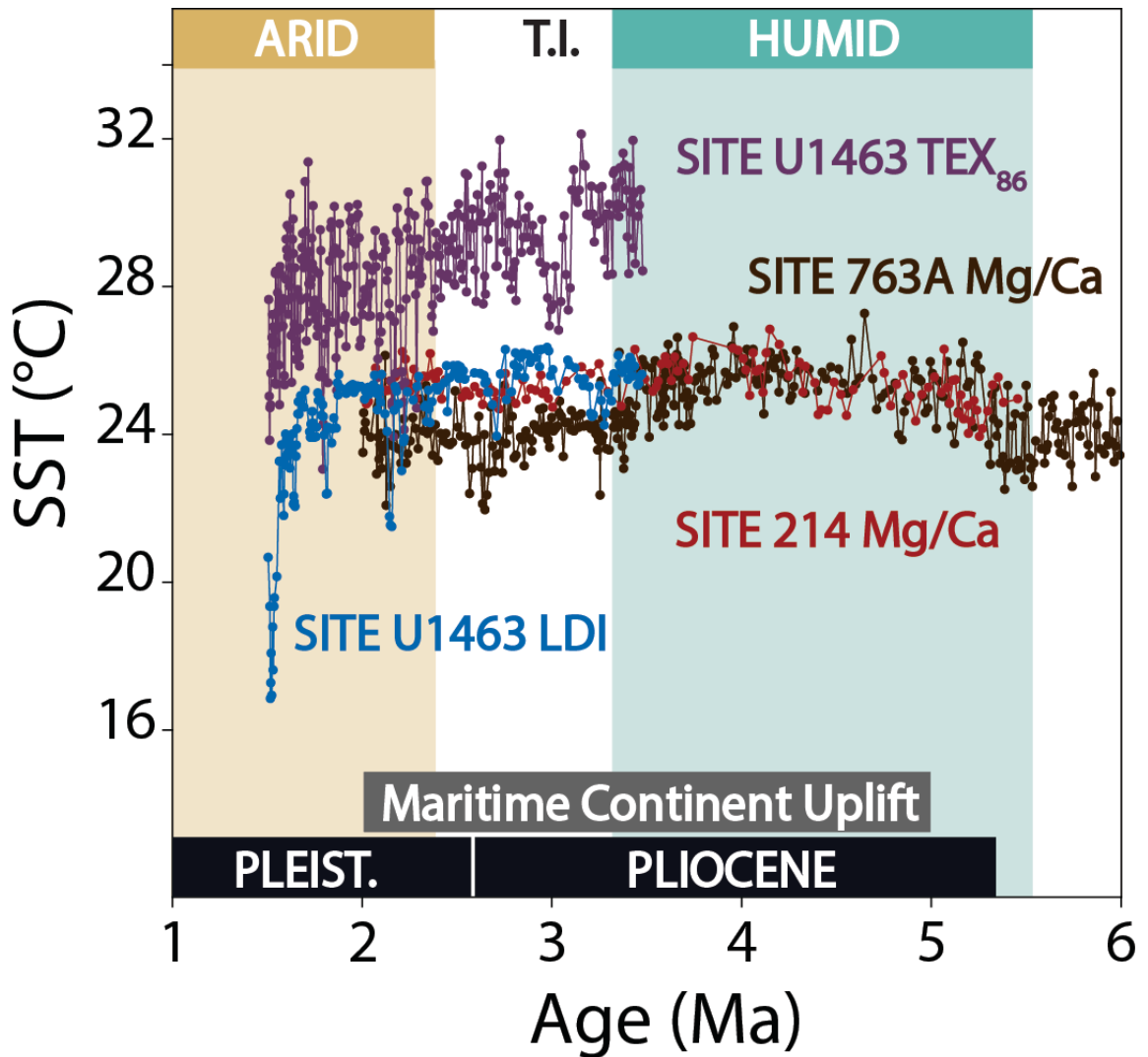


Figure 4.7: Summary of ITF SST records. SST records ( $^{\circ}\text{C}$ ) from Site U1463 LDI (blue), Site U1463  $\text{TEX}_{86}$  (purple), Site 214 Mg/Ca (red)(Karas et al., 2009), and Site 763A Mg/Ca (brown)(Karas et al., 2011a) across the interval from 6-1 Ma. Superimposed over data are the three hydrologic (brown for arid, white for transition, and teal for humid) intervals identified by Christensen et al. (2017).

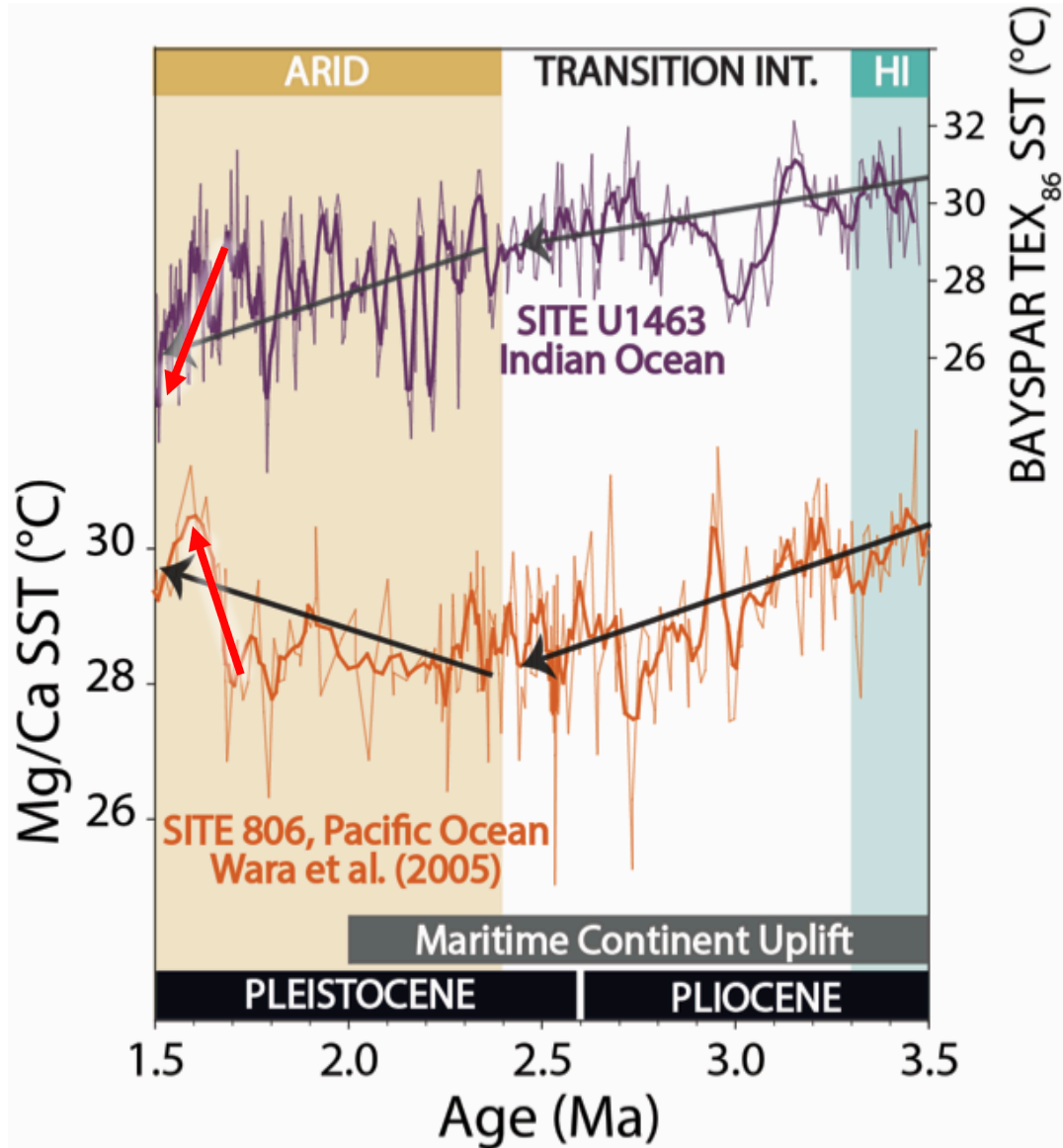


Figure 4.8: Comparison of ITF inflow and outflow SST records. From 3.5-1.5 Ma, depicting **UPPER**) BAYSPAR TEX<sub>86</sub> SSTs (°C) in purple from Site U1463, and **LOWER**) Mg/Ca SSTs (°C) in orange from Site 806 in the western equatorial Pacific Ocean (Wara et al., 2005). The dark orange and purple lines reflect smoothed 5 point running averages of SST data. Arrows indicate net trends in temperature and overlay all three hydrologic intervals (brown for arid, white for transition, and teal for humid) identified by Christensen et al. (2017). Steep cooling at Site U1463 and warming at Site 806 beginning at 1.7 Ma is shown in red arrows.

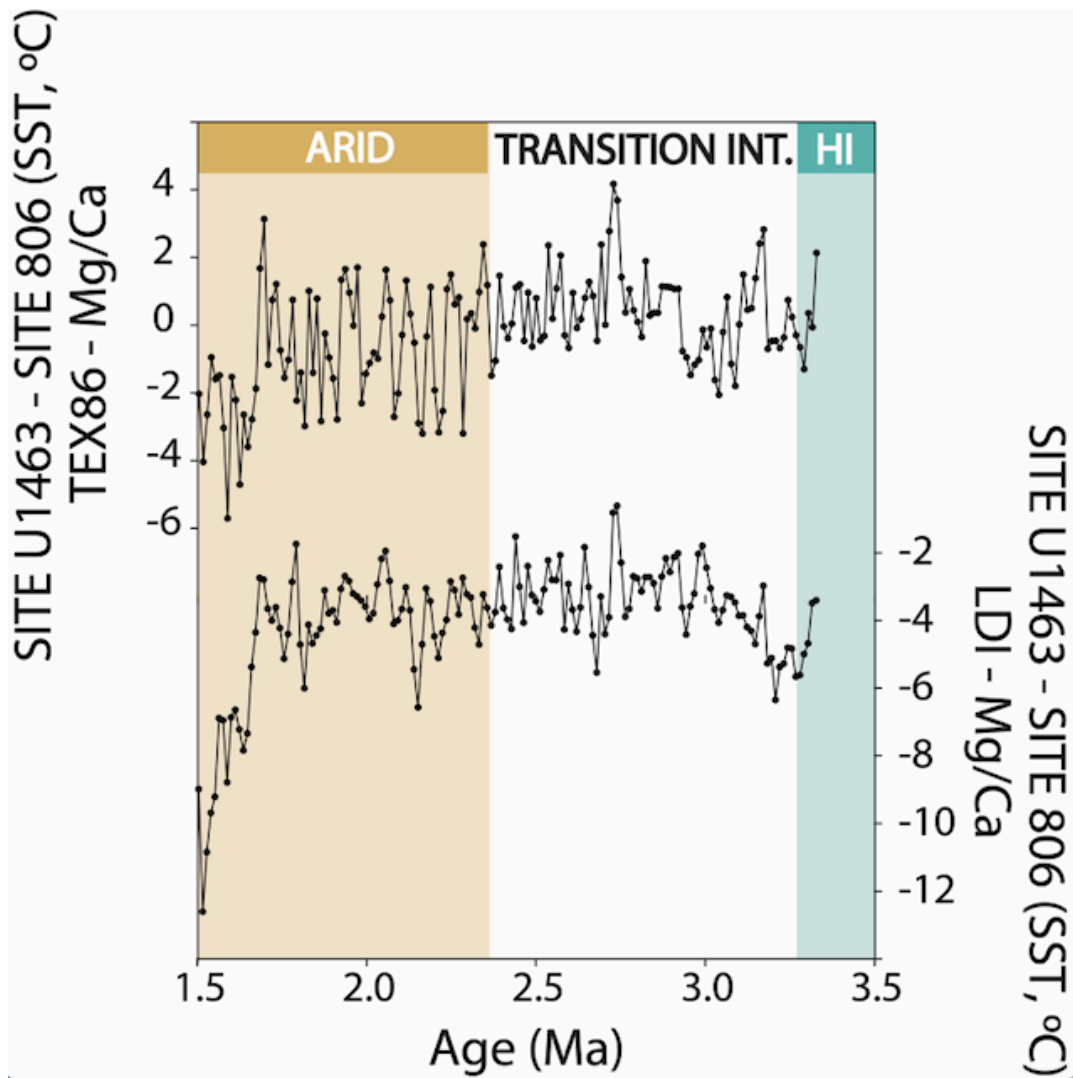


Figure 4.9: Zonal SST gradients from Site U1463 to Site 806. The upper curve shows the difference in SSTs between Site U1463 (TEX<sub>86</sub>) and Site 806 (Mg/Ca) from 3.5-1.5 Ma. The lower curve shows the same difference in SSTs, however LDI SSTs are applied at Site U1463 to calculate the SST difference. Superimposed over data are the three hydrologic (brown for arid, white for transition, and teal for humid) intervals identified by Christensen et al. (2017). The east-to-west zonal SST gradient was calculated by subtracting Mg/Ca-based SSTs at Site 806 from both TEX<sub>86</sub> and LDI-based SSTs at Site U1463 after re-sampling the records and placing them on a common timescale using the program Arand.

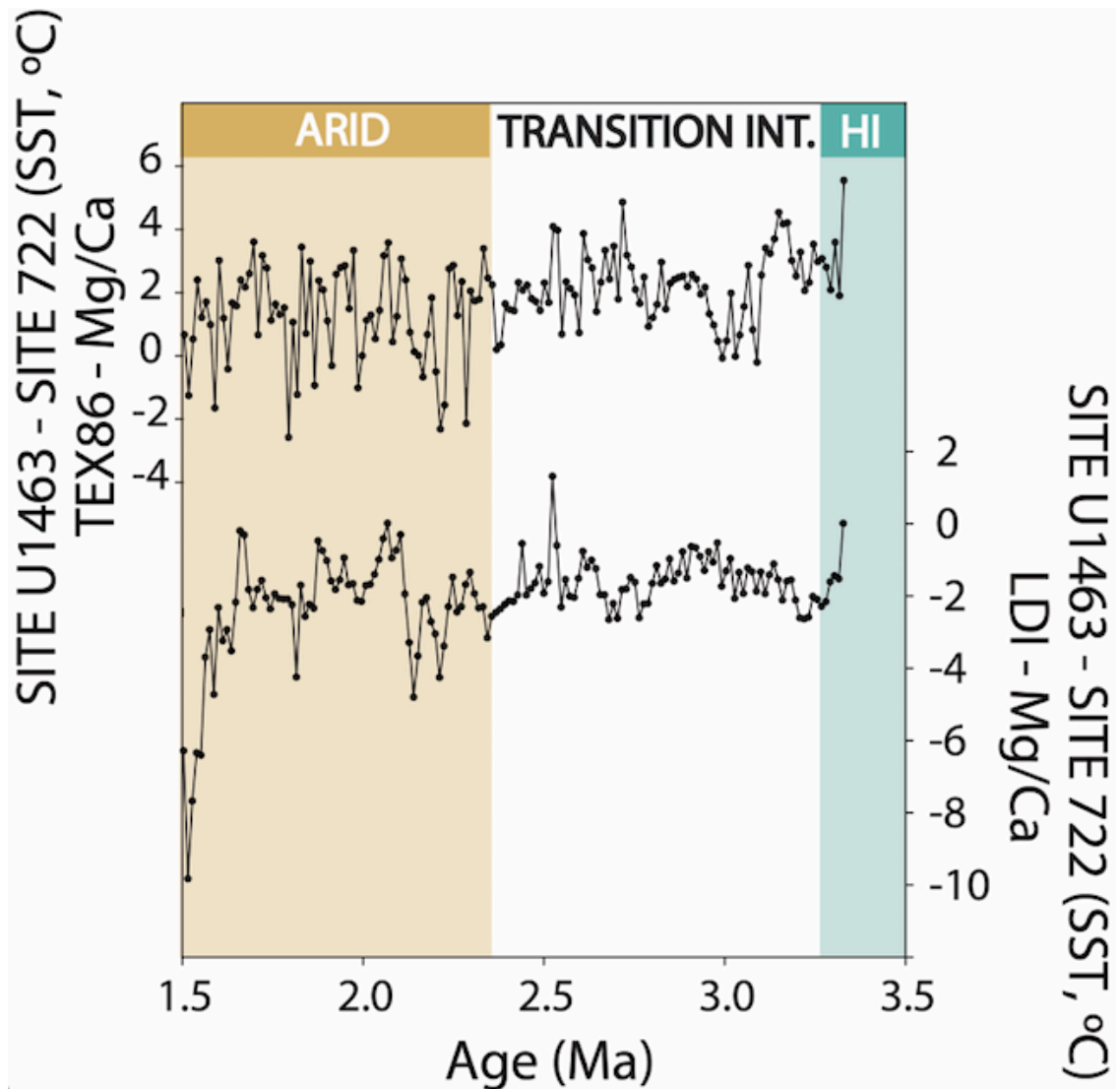


Figure 4.10: Meridional SST gradients from Site U1463 to Site 722. The upper curve shows the difference in SSTs between Site U1463 (TEX<sub>86</sub>) and Site 722 (Mg/Ca) from 3.5-1.5 Ma. The lower curve shows the same difference in SSTs, however LDI based SSTs are applied at Site U1463 to calculate the SST difference. Superimposed over data are the three hydrologic (brown for arid, white for transition, and teal for humid) intervals identified by Christensen et al. (2017). The meridional SST gradient was produced by subtracting Mg/Ca based SSTs at Site 722 (Herbert et al., 2010) from both TEX<sub>86</sub> and LDI-based SSTs at Site U1463 after placing them on a common timescale using the program Arand.

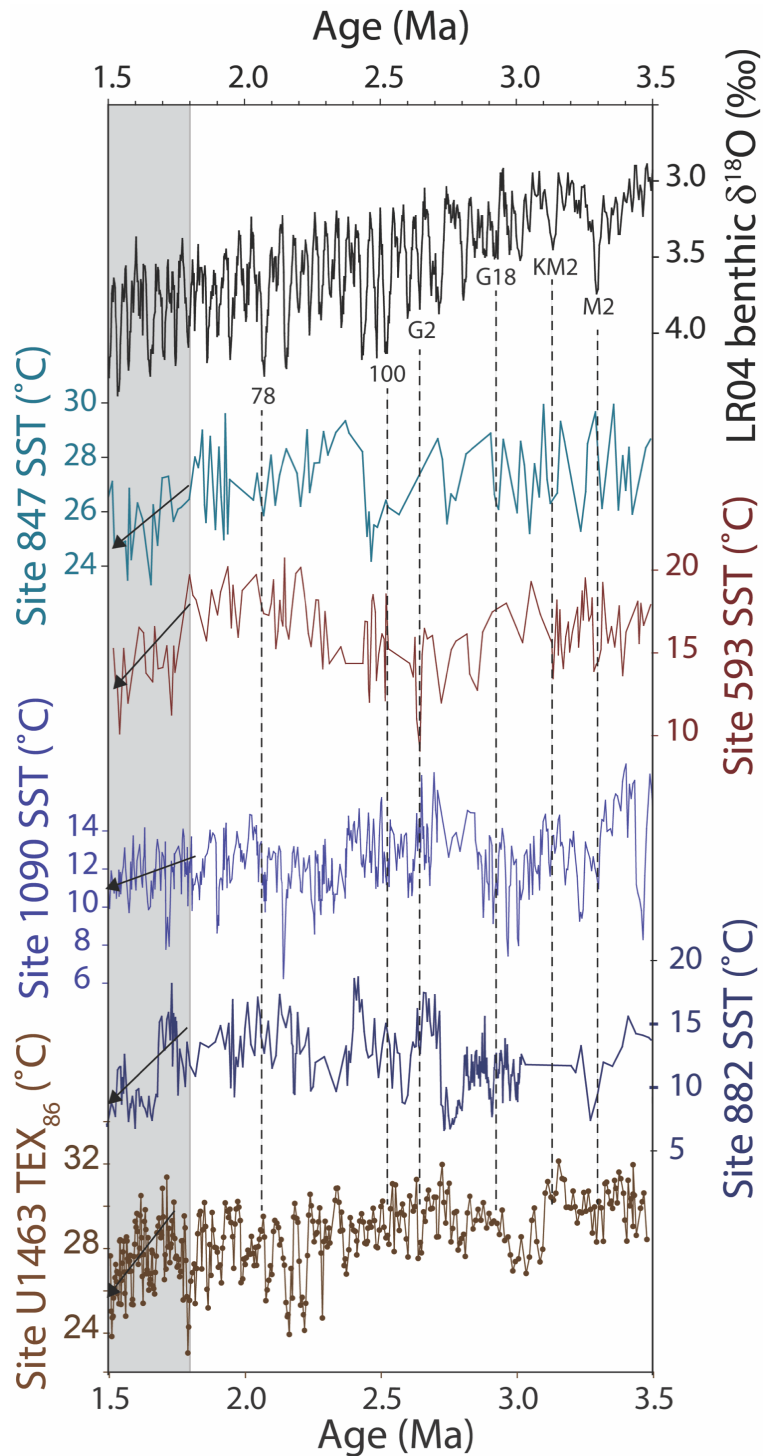
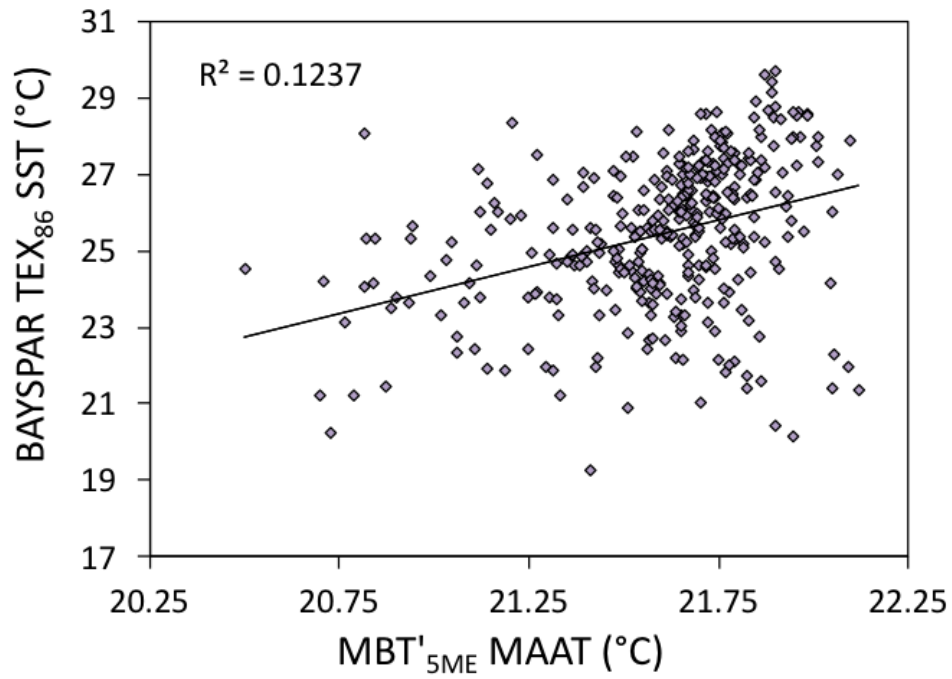
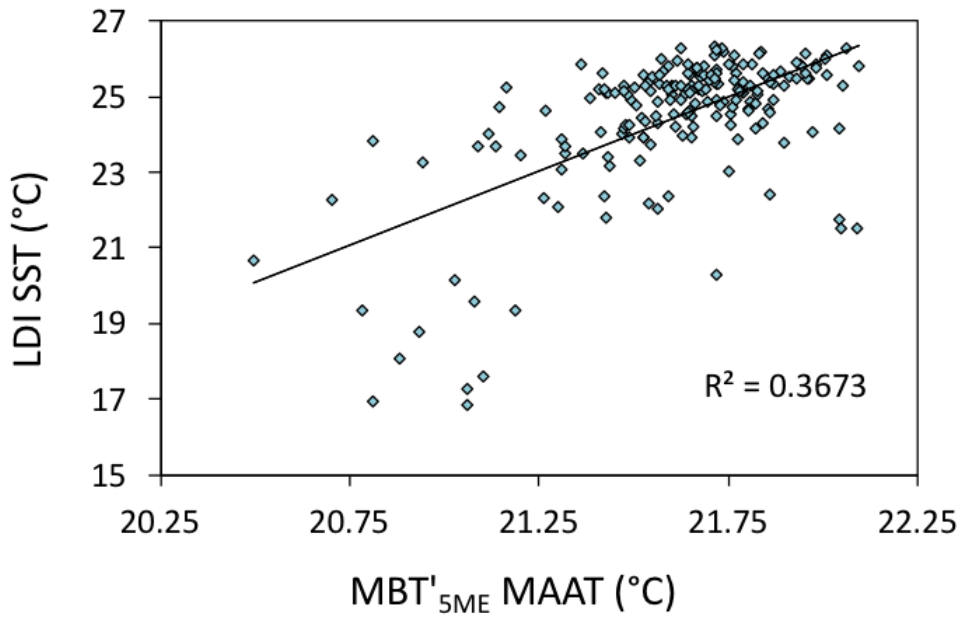


Figure 4.11: Global SST comparison from 3.5-1.5 Ma. The LR04 global benthic  $\delta^{18}\text{O}$  stack (black; Lisiecki & Raymo, 2005) is plotted vs. SSTs from Site U1463 (brown), Site 882 (navy; Martínez-García et al., 2010), Site 1090 (purple; Martínez-García et al., 2010), Site 593 (red; McClymont et al., 2008), and Site 847 (teal; Wara et al., 2005). Dashed lines indicate notable MIS Stages, black arrows indicate cooling, and the gray bar indicates the time interval from 1.8-1.5 Ma.



4.12: Cross-plot of MBT'<sub>5ME</sub> MAATs (°C) vs. BAYSPAR TEX<sub>86</sub> SSTs (°C). The solid black line indicates the linear best fit of the data.



4.13: Cross-plot of MBT'<sub>5ME</sub> MAATs (°C) vs. LDI SSTs (°C). The solid black line indicates the linear best fit of the data.

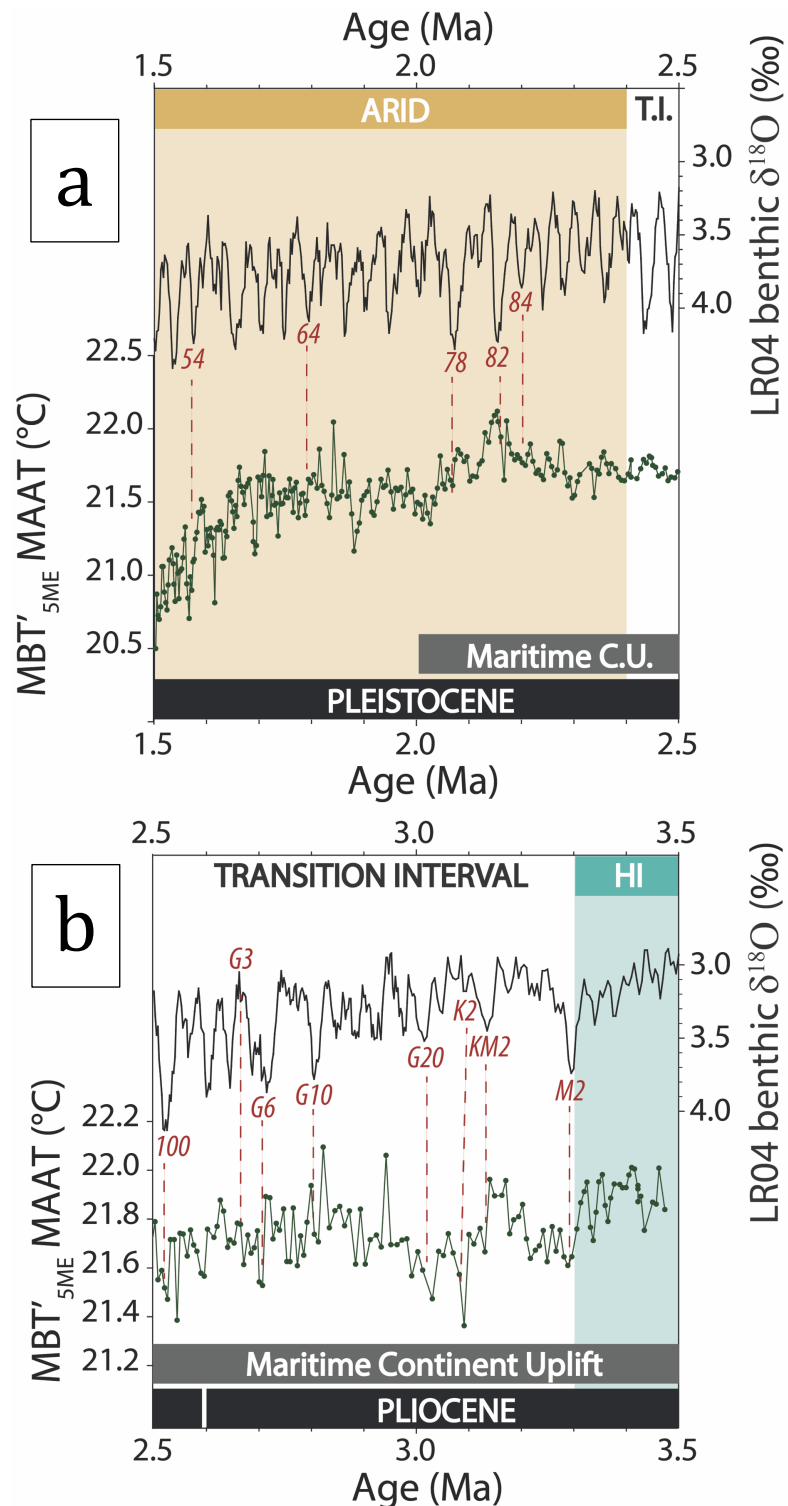


Figure 4.14: MBT' <sub>5ME</sub> (°C) versus the LR04 global benthic δ<sup>18</sup>O stack from **a**) 2.5-1.5 Ma and **b**) 3.5-2.5 Ma. Superimposed over data are the three hydrologic (brown for arid, white for transition, and teal for humid) intervals identified by Christensen et al. (2017).

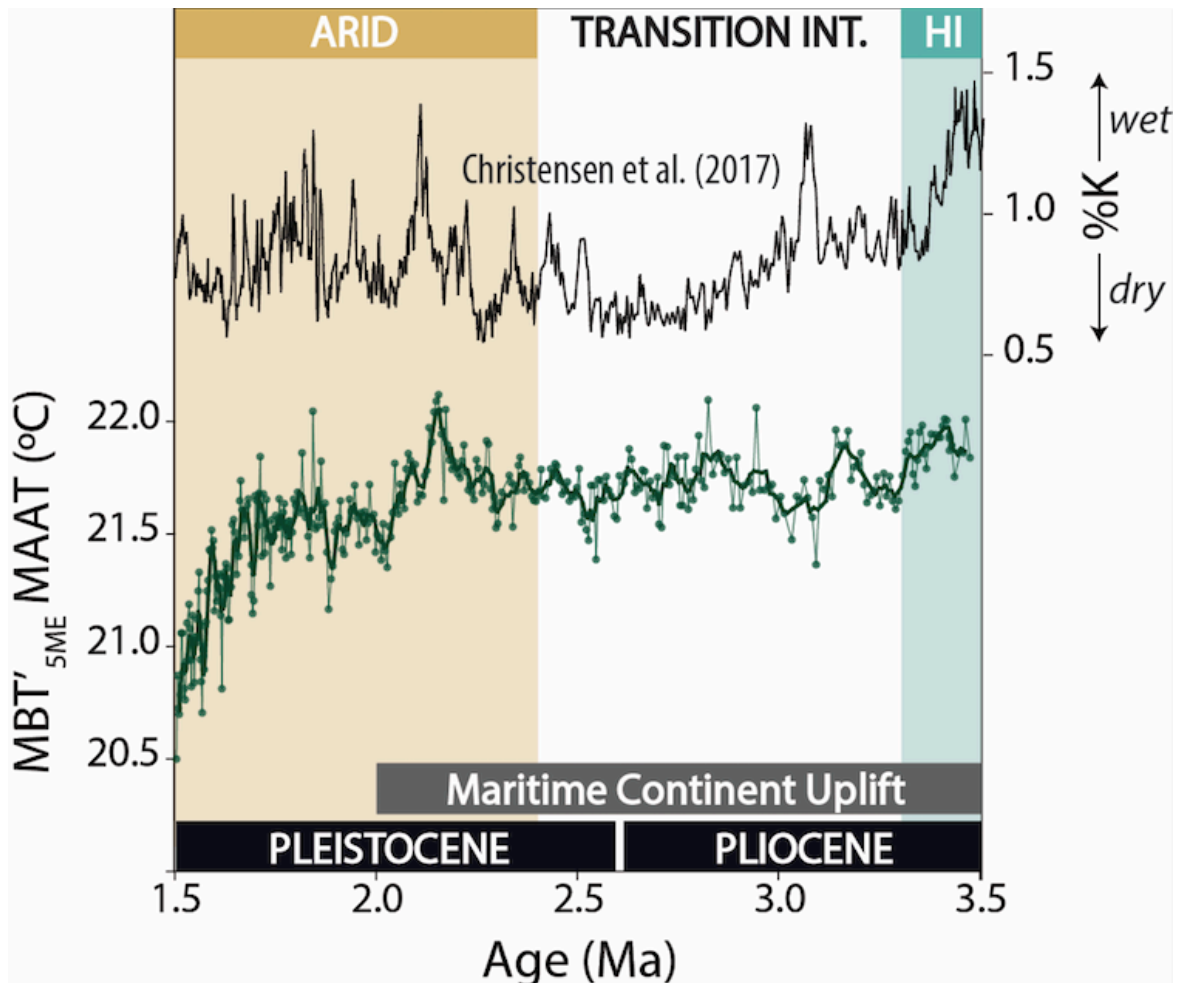


Fig 4.15: Continental air temperature and humidity reconstructions from Site U1463 from 3.5-1.5 Ma. MBT'5ME MAAT (°C) versus %K (Christensen et al. 2017). Superimposed over data are the three hydrologic (brown for arid, white for transition, and teal for humid) intervals identified by Christensen et al. (2017).

## CHAPTER 5

### CONCLUSIONS AND FUTURE WORK

#### 5.1 Summary of Interpretations

This project has applied three organic biomarker proxies (TEX<sub>86</sub>, LDI, and MBT'<sub>5ME</sub>) to sediments from Site U1463 in order to constrain shifts in ITF variability across the Plio-Pleistocene from 3.5-1.5 Ma. The U<sup>k</sup><sub>37</sub> index could not be applied to sediments in this study due to the presence of interfering coastal alkenone producing species. TEX<sub>86</sub>, LDI, and MBT'<sub>5ME</sub> records all show increased cooling at approximately 1.7 Ma, coincident with the onset of arid conditions in continental NW Australia identified by Christensen et al. (2017).

The onset of cooling observed at Site U1463 occurs later in the geologic record than previous studies have detected in the Indian Ocean. At Site 214, Karas et al. (2009) identify subsurface cooling from 3.5-2.95 Ma by 4°C, and at Site 763A, Karas et al. (2011a) identify surface cooling from ~4-3.3 Ma by 2-3°C. Both studies attribute these cooling events to a constriction of the ITF and a switch from South Pacific to North Pacific source waters. I offer two new hypotheses to explain the later cooling signal observed at Site U1463 at 1.7 Ma.

One possible explanation is that constriction of the ITF and emergence of the Maritime Continent did not finalize until after 2 Ma, at which point the final transition in source waters from the South Pacific to the North Pacific occurred. The cooling at 1.7 Ma would therefore reflect that final signal of uplift and ITF constriction. Cooling detected earlier in the geologic record at Sites 763A and 214 may in this case reflect a step-wise cooling associated with ITF constriction, rather

than a final switch in ITF source waters. SSTs from Site 806 show warming at 1.7 Ma, coincident with a final deflection of warm South Pacific warm waters towards Site 806 via the island of Halmahera (Figure 2A).

Another possible explanation for later cooling at Site U1463 is that the primary switch in source waters entering the ITF occurred between 4-3 Ma (Karas et al. 2009; Karas et al., 2011a), and that the cooling signal observed at Site U1463 instead reflects the constriction of the WPWP at 2 Ma (Brierley et al. 2006; Brierley et al., 2010) and a subsequent cooling of North Pacific ITF source waters. This explanation interprets the 1.7 Ma cooling event as a global climate signal, however the TEX<sub>86</sub> record does not seem to capture the magnitude of MIS M2 observed in other studies, which in turn suggests that Site U1463 may be capturing a more local climate signal. A more extensive record from 5.5-1 Ma at Site U1463 may help to constrain changes in SST before, during and after ITF constriction, as well as elucidate the local vs. global climate signals at Site U1463.

## **5.2 Extending the SST Record**

During my PhD at UMass Amherst, I will analyze the remaining sediments from Site U1463 that span the intervals from 1.5-1.0 Ma, and from 3.5-5.5 Ma. In order to maintain the sample resolution of ~5 kyr applied in this study, I will need to analyze 440 samples from 5.5-3.5 Ma, and 100 samples from 1.5-1.0 Ma. Analyzing this number of analyses will require extensive funding; therefore, I will initially only analyze 250 samples in order to produce a lower resolution reconstruction of 10ka across the entire core. Ideally, a full SST record spanning 5.5-1 Ma from Site U1463 will provide more information on the ITF before, during and

after constriction and Maritime Continent uplift. All future samples will be measured for  $\text{TEX}_{86}$ , LDI and  $\text{MBT}'_{5\text{Me}}$ . Future studies will also aim to improve the accuracy of  $\text{TEX}_{86}$ -based SST reconstructions at Site U1463 by producing a NW Australian core-top  $\text{TEX}_{86}$  record.

### **5.3 Core-Top $\text{TEX}_{86}$ Calibration**

Currently no NW Australian surface sediments have been analyzed as part of the spatially-varying BAYSPAR  $\text{TEX}_{86}$  calibration (Tierney and Tingley, 2014). Core-top samples from Sites U1459-U1464 (Figure 1) were shipped to the UMass Amherst Biogeochemistry Laboratory earlier this year, and are currently being analyzed by Kathryn Turner as part of her Honors Undergraduate Thesis aiming to fill this gap in data and improve the BAYSPAR calibration to include NW Australia  $\text{TEX}_{86}$  measurements. Results from her project will be used to improve the accuracy of  $\text{TEX}_{86}$  SST measurements from Site U1463.

### **5.4 Leaf Wax Isotope and Time Series Analysis**

Finally, I plan to conduct time series analysis on the records produced in this study and on future records produced as part of my PhD. Furthermore, in order to better constrain shifts in continental hydrology and the timing of the humid, transition and arid intervals, I will measure  $\delta\text{D}$  of leaf waxes preserved in sediments from Site U1463.

## BIBLIOGRAPHY

- Bartoli, G., Sarnthein, M., Weinelt, M., Erlenkeuser, H., Garbe-Schönberg, D., & Lea, D. W. (2005). Final closure of Panama and the onset of northern hemisphere glaciation. *Earth and Planetary Science Letters*, 237(1), 33–44. <https://doi.org/10.1016/j.epsl.2005.06.020>
- Bartoli, G., Hönisch, B., & Zeebe, R. E. (2011). Atmospheric CO<sub>2</sub> decline during the Pliocene intensification of Northern Hemisphere glaciations. *Paleoceanography*, 26(4), PA4213. <https://doi.org/10.1029/2010PA002055>
- Beman, J. M., Popp, B. N., & Francis, C. A. (2008). Molecular and biogeochemical evidence for ammonia oxidation by marine Crenarchaeota in the Gulf of California. *The ISME Journal*, 2(4), 429–441. <https://doi.org/10.1038/ismej.2007.118>
- Brassell, S. C. (1993). Applications of Biomarkers for Delineating Marine Paleoclimatic Fluctuations during the Pleistocene. In *Organic Geochemistry* (pp. 699–738). Springer, Boston, MA. [https://doi.org/10.1007/978-1-4615-2890-6\\_34](https://doi.org/10.1007/978-1-4615-2890-6_34)
- Brassell, S. C., Eglinton, G., Marlowe, I. T., Pflaumann, U., & Sarnthein, M. (1986). Molecular stratigraphy: a new tool for climatic assessment. *Nature*, 320(6058), 129–133. <https://doi.org/10.1038/320129a0>
- Brierley, C. M., & Fedorov, A. V. (2010). Relative importance of meridional and zonal sea surface temperature gradients for the onset of the ice ages and Pliocene-Pleistocene climate evolution. *Paleoceanography*, 25(2). <https://doi.org/10.1029/2009PA001809>
- Brierley, C. M., Fedorov, A. V., Liu, Z., Herbert, T. D., Lawrence, K. T., & LaRiviere, J. P. (2009). Greatly Expanded Tropical Warm Pool and Weakened Hadley Circulation in the Early Pliocene. *Science*, 323(5922), 1714–1718. <https://doi.org/10.1126/science.1167625>
- Brochier-Armanet, C., Boussau, B., Gribaldo, S., & Forterre, P. (2008). Mesophilic crenarchaeota: proposal for a third archaeal phylum, the Thaumarchaeota. *Nature Reviews Microbiology*, 6(3), 245–252. <https://doi.org/10.1038/nrmicro1852>
- Cane, M. A., & Molnar, P. (2001). Closing of the Indonesian seaway as a precursor to east African aridification around 3–4 million years ago. *Nature*, 411(6834), 157–162. <https://doi.org/10.1038/35075500>

- Castañeda, I. S., & Schouten, S. (2011). A review of molecular organic proxies for examining modern and ancient lacustrine environments. *Quaternary Science Reviews*, 30(21), 2851–2891. <https://doi.org/10.1016/j.quascirev.2011.07.009>
- Castañeda, I. S., Schefuß, E., Pätzold, J., Damsté, J. S. S., Weldeab, S., & Schouten, S. (2010). Millennial-scale sea surface temperature changes in the eastern Mediterranean (Nile River Delta region) over the last 27,000 years. *Paleoceanography*, 25(1). <https://doi.org/10.1029/2009PA001740>
- Christensen, B. A., Renema, W., Henderiks, J., De Vleeschouwer, D., Groeneveld, J., Castañeda, I. S., et al. (2017). Indonesian Throughflow drove Australian climate from humid Pliocene to arid Pleistocene. *Geophysical Research Letters*, 44(13), 2017GL072977. <https://doi.org/10.1002/2017GL072977>
- Coates, A. G., & Stallard, R. F. (2013). How old is the Isthmus of Panama? *Bulletin of Marine Science*, 89(4), 801–813. <https://doi.org/info:doi/10.5343/bms.2012.1076>
- De Jonge, C., Hopmans, E. C., Stadnitskaia, A., Rijpstra, W. I. C., Hofland, R., Tegelaar, E., & Sinninghe Damsté, J. S. (2013). Identification of novel penta- and hexamethylated branched glycerol dialkyl glycerol tetraethers in peat using HPLC–MS2, GC–MS and GC–SMB–MS. *Organic Geochemistry*, 54, 78–82. <https://doi.org/10.1016/j.orggeochem.2012.10.004>
- De Jonge, C., Hopmans, E. C., Zell, C. I., Kim, J.-H., Schouten, S., & Sinninghe Damsté, J. S. (2014a). Occurrence and abundance of 6-methyl branched glycerol dialkyl glycerol tetraethers in soils: Implications for palaeoclimate reconstruction. *Geochimica et Cosmochimica Acta*, 141, 97–112. <https://doi.org/10.1016/j.gca.2014.06.013>
- De Jonge, C., Stadnitskaia, A., Hopmans, E. C., Cherkashov, G., Fedotov, A., & Sinninghe Damsté, J. S. (2014b). In situ produced branched glycerol dialkyl glycerol tetraethers in suspended particulate matter from the Yenisei River, Eastern Siberia. *Geochimica et Cosmochimica Acta*, 125, 476–491. <https://doi.org/10.1016/j.gca.2013.10.031>
- Dowsett, H. J., Cronin, T. M., Poore, R. Z., Thompson, R. S., Whatley, R. C., & Wood, A. M. (1992). Micropaleontological Evidence for Increased Meridional Heat Transport in the North Atlantic Ocean During the Pliocene. *Science*, 258(5085), 1133–1135. <https://doi.org/10.1126/science.258.5085.1133>
- Dowsett, H. J., Robinson, M. M., & Foley, K. M. (2009). Pliocene three-dimensional global ocean temperature reconstruction. *Clim. Past*, 5(4), 769–783. <https://doi.org/10.5194/cp-5-769-2009>

- Epstein, B. L., D'Hondt, S., Quinn, J. G., Zhang, J., & Hargraves, P. E. (2010). An effect of dissolved nutrient concentrations on alkenone-based temperature estimates. *Paleoceanography*, 13(2), 122–126. <https://doi.org/10.1029/97PA03358>
- Esri. "Ocean." [Basemap]. 1:591,657,528 down to 1:9,028. "World Ocean Base". Created February 24, 2014. Updated March 29, 2018. <https://www.arcgis.com/home/item.html?id=1e126e7520f9466c9ca28b8f28b5e500>. (June 14<sup>th</sup>, 2018).
- Esri. "Ocean Reference." [Basemap]. 1:591,657,528 down to 1:9,028. "World Ocean Reference". Created February 24, 2014. Updated March 29, 2018. <https://www.arcgis.com/home/item.html?id=0fd0c5b7a647404d8934516aa997e6d9>. (June 14<sup>th</sup>, 2018).
- Flesche Kleiven, H., Jansen, E., Fronval, T., & Smith, T. M. (2002). Intensification of Northern Hemisphere glaciations in the circum Atlantic region (3.5–2.4 Ma) – ice-rafted detritus evidence. *Palaeogeography, Palaeoclimatology, Palaeoecology*, 184(3), 213–223. [https://doi.org/10.1016/S0031-0182\(01\)00407-2](https://doi.org/10.1016/S0031-0182(01)00407-2)
- Forte, A. M., & Mitrovica, J. X. (2016). The PRISM4 (mid-Piacenzian) paleoenvironmental reconstruction. *Climate of the Past; Katlenburg-Lindau*, 12(7), 1519–1538. <http://dx.doi.org/10.5194/cp-12-1519-2016>
- Frank, M. (2002). Radiogenic Isotopes: Tracers of Past Ocean Circulation and Erosional Input. *Reviews of Geophysics*, 40(1), 1–1. <https://doi.org/10.1029/2000RG000094>
- Gallagher, S. J., Fulthorpe, C. S., & Bogus, K. A. (2014). Reefs, oceans, and climate: a 5 million year history of the Indonesian Throughflow, Australian monsoon, and subsidence on the northwest shelf of Australia. (International Ocean Discovery Program Scientific Prospectus, 356). Retrieved from <http://dx.doi.org/10.14379/iodp.sp.356.2014>
- Gallagher, S. J., Fulthorpe, C. S., Bogus, K. A., & Expedition 356 Scientistis. (2017). Expedition 356 Preliminary Report: Indonesian Throughflow (International Ocean Discovery Program). Retrieved from <http://dx.doi.org/10.14379/iodp.pr.356.2017>
- Gattinger A., Günthner A., Schloter M., & Munch J.C. (2003). Characterisation of Archaea in Soils by Polar Lipid Analysis. *Acta Biotechnologica*, 23(1), 21–28. <https://doi.org/10.1002/abio.200390003>

- Godfrey, J. S. (1996). The effect of the Indonesian throughflow on ocean circulation and heat exchange with the atmosphere: A review. *Journal of Geophysical Research: Oceans*, 101(C5), 12217–12237.  
<https://doi.org/10.1029/95JC03860>
- Gordon, A. L. (2005). Oceanography of the Indonesian Seas and Their Throughflow. *Oceanography*, 18(4), 14–27.
- Gordon, A. L., & Fine, R. A. (1996). Pathways of water between the Pacific and Indian oceans in the Indonesian seas. *Nature*, 379(6561), 146–149.  
<https://doi.org/10.1038/379146a0>
- Gordon, A. L., Susanto, R. D., & Field, A. (1999). Throughflow within Makassar Strait. *Geophysical Research Letters*, 26(21), 3325–3328.  
<https://doi.org/10.1029/1999GL002340>
- Haug, G. H., & Tiedemann, R. (1998). Effect of the formation of the Isthmus of Panama on Atlantic Ocean thermohaline circulation. *Nature*, 393(6686), 673–676. <https://doi.org/10.1038/31447>
- Hay, W. W. (1996). Tectonics and climate. *Geologische Rundschau*, 85(3), 409–437.  
<https://doi.org/10.1007/BF02369000>
- Herbert, T. D. (2006). Alkenone Paleotemperature Determinations in the Oceans and Marine Geochemistry (pp. 391–416). Elsevier.
- Herbert, T. D., & Schuffert, J. D. (1998). Alkenone unsaturation estimates of late miocene through late pliocene sea-surface temperatures at Site 958. *Proceedings of the Ocean Drilling Program, Scientific Results*, 159, 159–17.  
<https://doi.org/10.2973/odp.proc.sr.159T.063.1998>
- Herbert, T. D., Peterson, L. C., Lawrence, K. T., & Liu, Z. (2010). Tropical Ocean Temperatures Over the Past 3.5 Million Years. *Science*, 328(5985), 1530–1534. <https://doi.org/10.1126/science.1185435>
- Herfort, L., Schouten, S., Boon, J. P., & Sinninghe Damsté, J. S. (2006). Application of the TEX<sub>86</sub> temperature proxy to the southern North Sea. *Organic Geochemistry*, 37(12), 1715–1726.  
<https://doi.org/10.1016/j.orggeochem.2006.07.021>
- Hershberger, K. L., Barns, S. M., Reysenbach, A.-L., Dawson, S. C., & Pace, N. R. (1996). Wide diversity of Crenarchaeota. *Nature*; London, 384(6608), 420.  
<http://dx.doi.org/10.1038/384420a0>

- Hirahara, S., Ishii, M., & Fukuda, Y. (2013). Centennial-Scale Sea Surface Temperature Analysis and Its Uncertainty. *Journal of Climate*, 27(1), 57–75. <https://doi.org/10.1175/JCLI-D-12-00837.1>
- Hönisch, B., Hemming, N. G., Archer, D., Siddall, M., & McManus, J. F. (2009). Atmospheric Carbon Dioxide Concentration Across the Mid-Pleistocene Transition. *Science*, 324(5934), 1551–1554. <https://doi.org/10.1126/science.1171477>
- Hopmans, E. C., Weijers, J. W. H., Schefuß, E., Herfort, L., Sinninghe Damsté, J. S., & Schouten, S. (2004). A novel proxy for terrestrial organic matter in sediments based on branched and isoprenoid tetraether lipids. *Earth and Planetary Science Letters*, 224(1), 107–116. <https://doi.org/10.1016/j.epsl.2004.05.012>
- Hopmans, E. C., Schouten, S., & Sinninghe Damsté, J. S. (2016). The effect of improved chromatography on GDGT-based palaeoproxies. *Organic Geochemistry*, 93, 1–6. <https://doi.org/10.1016/j.orggeochem.2015.12.006>
- Huguet, C., Schimmelmann, A., Thunell, R., Lourens, L. J., Sinninghe Damsté, J. S., & Schouten, S. (2007). A study of the TEX<sub>86</sub> paleothermometer in the water column and sediments of the Santa Barbara Basin, California. *Paleoceanography*, 22(3). <https://doi.org/10.1029/2006PA001310>
- Huguet, C., Martrat, B., Grimalt, J. O., Sinninghe Damsté, J. S., & Schouten, S. (2011). Coherent millennial-scale patterns in U<sup>37</sup><sub>K'</sub> and TEX<sub>86</sub><sup>H</sup> temperature records during the penultimate interglacial-to-glacial cycle in the western Mediterranean. *Paleoceanography*, 26(2). <https://doi.org/10.1029/2010PA002048>
- Hurley, S. J., Elling, F. J., Könneke, M., Buchwald, C., Wankel, S. D., Santoro, A. E., et al. (2016). Influence of ammonia oxidation rate on thaumarchaeal lipid composition and the TEX<sub>86</sub> temperature proxy. *Proceedings of the National Academy of Sciences*, 113(28), 7762–7767. <https://doi.org/10.1073/pnas.1518534113>
- Karas, C., Nürnberg, D., Gupta, A. K., Tiedemann, R., Mohan, K., & Bickert, T. (2009). Mid-Pliocene climate change amplified by a switch in Indonesian subsurface throughflow. *Nature Geoscience*, 2(6), 434–438. <https://doi.org/10.1038/ngeo520>
- Karas, C., Nürnberg, D., Tiedemann, R., & Garbe-Schönberg, D. (2011a). Pliocene Indonesian Throughflow and Leeuwin Current dynamics: Implications for Indian Ocean polar heat flux. *Paleoceanography*, 26(2). <https://doi.org/10.1029/2010PA001949>

- Karas, C., Nürnberg, D., Tiedemann, R., & Garbe-Schönberg, D. (2011b). Pliocene climate change of the Southwest Pacific and the impact of ocean gateways. *Earth and Planetary Science Letters*, 301(1), 117–124. <https://doi.org/10.1016/j.epsl.2010.10.028>
- Karas, C., Nürnberg, D., Bahr, A., Groeneveld, J., Herrle, J. O., Tiedemann, R., & deMenocal, P. B. (2017). Pliocene oceanic seaways and global climate. *Scientific Reports*, 7, 39842. <https://doi.org/10.1038/srep39842>
- Karner, M. B., DeLong, E. F., & Karl, D. M. (2001). Archaeal dominance in the mesopelagic zone of the Pacific Ocean. *Nature*, 409(6819), 507–510. <https://doi.org/10.1038/35054051>
- Kim, J.-H., Schouten, S., Hopmans, E. C., Donner, B., & Sinninghe Damsté, J. S. (2008). Global sediment core-top calibration of the TEX<sub>86</sub> paleothermometer in the ocean. *Geochimica et Cosmochimica Acta*, 72(4), 1154–1173. <https://doi.org/10.1016/j.gca.2007.12.010>
- Kim, J.-H., van der Meer, J., Schouten, S., Helmke, P., Willmott, V., Sangiorgi, F., et al. (2010). New indices and calibrations derived from the distribution of crenarchaeal isoprenoid tetraether lipids: Implications for past sea surface temperature reconstructions. *Geochimica et Cosmochimica Acta*, 74(16), 4639–4654. <https://doi.org/10.1016/j.gca.2010.05.027>
- King, A. D., Donat, M. G., Alexander, L. V., & Karoly, D. J. (2015). The ENSO-Australian rainfall teleconnection in reanalysis and CMIP5. *Climate Dynamics*, 44(9–10), 2623–2635. <https://doi.org/10.1007/s00382-014-2159-8>
- Kominz, M. A., Gurnis, M., Gallagher, S. J., & Expedition 356 Scientists, I. (2017). Australian Northwest Shelf: A Late Neogene Reversible Tectonic Event. *AGU Fall Meeting Abstracts*, 54. Retrieved from <http://adsabs.harvard.edu/abs/2017AGUFMOS54B..06K>
- Könneke, M., Bernhard, A. E., Torre, J. R. de la, Walker, C. B., Waterbury, J. B., & Stahl, D. A. (2005). Isolation of an autotrophic ammonia-oxidizing marine archaeon. *Nature*, 437(7058), 543–546. <https://doi.org/10.1038/nature03911>
- Kroopnick, P. M. (1985). The distribution of <sup>13</sup>C of ΣCO<sub>2</sub> in the world oceans. *Deep Sea Research Part A. Oceanographic Research Papers*, 32(1), 57–84. [https://doi.org/10.1016/0198-0149\(85\)90017-2](https://doi.org/10.1016/0198-0149(85)90017-2)
- Lattaud, J., Kim, J.-H., De Jonge, C., Zell, C., Sinninghe Damsté, J. S., & Schouten, S. (2017). The C<sub>32</sub> alkane-1,15-diol as a tracer for riverine input in coastal seas. *Geochimica et Cosmochimica Acta*, 202, 146–158. <https://doi.org/10.1016/j.gca.2016.12.030>

- Lawrence K. T., Sigman D. M., Herbert T. D., Riihimaki C. A., Bolton C. T., Martinez-Garcia A., et al. (2013). Time-transgressive North Atlantic productivity changes upon Northern Hemisphere glaciation. *Paleoceanography*, 28(4), 740–751. <https://doi.org/10.1002/2013PA002546>
- Lee, K. E., Kim, J.-H., Wilke, I., Helmke, P., & Schouten, S. (2008). A study of the alkenone, TEX<sub>86</sub>, and planktonic foraminifera in the Benguela Upwelling System: Implications for past sea surface temperature estimates. *Geochemistry, Geophysics, Geosystems*, 9(10). <https://doi.org/10.1029/2008GC002056>
- de Leeuw, J. W., v.d. Meer, F. W., Rijpstra, W. I. C., & Schenck, P. A. (1980). On the occurrence and structural identification of long chain unsaturated ketones and hydrocarbons in sediments. *Physics and Chemistry of the Earth*, 12(Supplement C), 211–217. [https://doi.org/10.1016/0079-1946\(79\)90105-8](https://doi.org/10.1016/0079-1946(79)90105-8)
- Leider, A., Hinrichs, K.-U., Mollenhauer, G., & Versteegh, G. J. M. (2010). Core-top calibration of the lipid-based U<sub>37<sup>K'</sup></sub> and TEX<sub>86</sub> temperature proxies on the southern Italian shelf (SW Adriatic Sea, Gulf of Taranto). *Earth and Planetary Science Letters*, 300(1), 112–124. <https://doi.org/10.1016/j.epsl.2010.09.042>
- Lisiecki, L. E., & Raymo, M. E. (2005). A Pliocene-Pleistocene stack of 57 globally distributed benthic δ<sup>18</sup>O records: Pliocene-Pleistocene benthic stack. *Paleoceanography*, 20(1), n/a-n/a. <https://doi.org/10.1029/2004PA001071>
- Lopes dos Santos, R. A., Spooner, M. I., Barrows, T. T., De Deckker, P., Sinninghe Damsté, J. S., & Schouten, S. (2013). Comparison of organic (U<sup>K</sup><sub>37</sub>, TEX<sub>86</sub><sup>H</sup>, LDI) and faunal proxies (foraminiferal assemblages) for reconstruction of late Quaternary sea surface temperature variability from offshore southeastern Australia. *Paleoceanography*, 28(3), 377–387. <https://doi.org/10.1002/palo.20035>
- Marincovich Jr, L., & Gladenkov, A. Y. (1999). Evidence for an early opening of the Bering Strait. *Nature*, 397(6715), 149–151. <https://doi.org/10.1038/16446>
- Marshall, L. G. (1988). Land Mammals and the Great American Interchange. *American Scientist*, 76(4), 380–388.
- Marshall, L. G., Webb, S. D., Sepkoski, J. J., & Raup, D. M. (1982). Mammalian Evolution and the Great American Interchange. *Science*, 215(4538), 1351–1357. <https://doi.org/10.1126/science.215.4538.1351>

- Martin, E. E., & Scher, H. (2006). A Nd isotopic study of southern sourced waters and Indonesian Throughflow at intermediate depths in the Cenozoic Indian Ocean. *Geochemistry, Geophysics, Geosystems*, 7(9), Q09N02. <https://doi.org/10.1029/2006GC001302>
- Martínez-García, A., Rosell-Melé, A., McClymont, E. L., Gersonde, R., & Haug, G. H. (2010). Subpolar Link to the Emergence of the Modern Equatorial Pacific Cold Tongue. *Science*, 328(5985), 1550–1553. <https://doi.org/10.1126/science.1184480>
- Maslin, M. A., Li, X. S., Loutre, M.-F., & Berger, A. (1998). The contribution of orbital forcing to the progressive intensification of Northern Hemisphere Glaciation. *Quaternary Science Reviews*, 17(4), 411–426. [https://doi.org/10.1016/S0277-3791\(97\)00047-4](https://doi.org/10.1016/S0277-3791(97)00047-4)
- McClymont, E. L., Rosell-Melé, A., Haug, G. H., & Lloyd, J. M. (2008). Expansion of subarctic water masses in the North Atlantic and Pacific oceans and implications for mid-Pleistocene ice sheet growth. *Paleoceanography and Paleoclimatology*, 23(4). <https://doi.org/10.1029/2008PA001622>
- McClymont, E. L., Elmore, A. C., Kender, S., Leng, M. J., Greaves, M., & Elderfield, H. (2016). Pliocene-Pleistocene evolution of sea surface and intermediate water temperatures from the southwest Pacific. *Paleoceanography*, 31(6), 895–913. <http://doi.org/10.1002/2016PA002954>
- McCorkle, D. C., & Keigwin, L. D. (2010). Depth profiles of  $\delta^{13}\text{C}$  in bottom water and core top *C. wuellerstorfi* on the Ontong Java Plateau and Emperor Seamounts. *Paleoceanography*, 9(2), 197–208. <http://doi.org/10.1029/93PA03271>
- McKay, R., Naish, T., Carter, L., Riesselman, C., Dunbar, R., Sjunneskog, C., et al. (2012). Antarctic and Southern Ocean influences on Late Pliocene global cooling. *Proceedings of the National Academy of Sciences*, 109(17), 6423–6428. <https://doi.org/10.1073/pnas.1112248109>
- Menzel, D., Hopmans, E. C., Schouten, S., & Sinninghe Damsté, J. S. (2006). Membrane tetraether lipids of planktonic Crenarchaeota in Pliocene sapropels of the eastern Mediterranean Sea. *Palaeogeography, Palaeoclimatology, Palaeoecology*, 239(1), 1–15. <https://doi.org/10.1016/j.palaeo.2006.01.002>
- Molnar, P., & Cronin, T. W. (2015). Growth of the Maritime Continent and its possible contribution to recurring Ice Ages. *Paleoceanography*, 30(3), 196–225. <https://doi.org/10.1002/2014PA002752>
- Morey, S. L., Shriver, J. F., & O'Brien, J. J. (1999). The effects of Halmahera on the Indonesian throughflow. *Journal of Geophysical Research: Oceans*, 104(C10), 23281–23296. <https://doi.org/10.1029/1999JC900195>

- Müller, P. J., Kirst, G., Ruhland, G., von Storch, I., & Rosell-Melé, A. (1998). Calibration of the alkenone paleotemperature index  $U_{37}^{K'}$  based on core-tops from the eastern South Atlantic and the global ocean (60°N-60°S). *Geochimica et Cosmochimica Acta*, 62(10), 1757–1772. [https://doi.org/10.1016/S0016-7037\(98\)00097-0](https://doi.org/10.1016/S0016-7037(98)00097-0)
- Naafs, B. D. A., Hefter, J., & Stein, R. (2012). Application of the long chain diol index (LDI) paleothermometer to the early Pleistocene (MIS 96). *Organic Geochemistry*, 49, 83–85. <https://doi.org/10.1016/j.orggeochem.2012.05.011>
- Newell, S. E., Fawcett, S. E., & Ward, B. B. (2013). Depth distribution of ammonia oxidation rates and ammonia-oxidizer community composition in the Sargasso Sea. *Limnology and Oceanography*, 58(4), 1491–1500. <https://doi.org/10.4319/lo.2013.58.4.1491>
- Pagani, M., Liu, Z., LaRiviere, J., & Ravelo, A. C. (2010). High Earth-system climate sensitivity determined from Pliocene carbon dioxide concentrations. *Nature Geoscience*, 3(1), 27–30. <https://doi.org/10.1038/ngeo724>
- Pelejero, C., & Calvo, E. (2003). The upper end of the  $U_{37}^{K'}$  temperature calibration revisited. *Geochemistry, Geophysics, Geosystems*, 4(2), 1014. <https://doi.org/10.1029/2002GC000431>
- Peters, K. E., Walters, C. C., & Moldowan, J. M. (2005). *The Biomarker Guide*. Cambridge University Press.
- Placencia, J. A., Garcés-Vargas, J., Lange, C. B., & Hebbeln, D. (2010). Alkenone-based temperature patterns along the eastern South Pacific Coastal Ocean: the effect of upwelling and advection on the sedimentary alkenone unsaturation index ( $U_{37}^{K'}$ ). *Copernicus Publications*, (7), 545–564.
- Prahl, F. G., & Muehlhausen, L. A. (1989). Lipid biomarkers as geochemical tools for paleoceanographic study. *Productivity of the Ocean: Present and Past*, 27, 1–289.
- Prahl, F. G., & Wakeham, S. G. (1987). Calibration of unsaturation patterns in long-chain ketone compositions for palaeotemperature assessment. *Nature*, 330(6146), 367–369. <https://doi.org/10.1038/330367a0>
- Prahl, F. G., Popp, B. N., Karl, D. M., & Sparrow, M. A. (2005). Ecology and biogeochemistry of alkenone production at Station ALOHA. *Deep Sea Research Part I: Oceanographic Research Papers*, 52(5), 699–719. <https://doi.org/10.1016/j.dsr.2004.12.001>

- Rampen, S. W., Willmott, V., Kim, J.-H., Uliana, E., Mollenhauer, G., Schefuß, E., et al. (2012). Long chain 1,13- and 1,15-diols as a potential proxy for palaeotemperature reconstruction. *Geochimica et Cosmochimica Acta*, 84, 204–216. <https://doi.org/10.1016/j.gca.2012.01.024>
- Rampen, S. W., Datema, M., Rodrigo-Gámiz, M., Schouten, S., Reichart, G.-J., & Sinninghe Damsté, J. S. (2014). Sources and proxy potential of long chain alkyl diols in lacustrine environments. *Geochimica et Cosmochimica Acta*, 144, 59–71. <https://doi.org/10.1016/j.gca.2014.08.033>
- Raymo, M. E., Grant, B., Horowitz, M., & Rau, G. H. (1996). Mid-Pliocene warmth: stronger greenhouse and stronger conveyor. *Marine Micropaleontology*, 27(1–4), 313–326. [https://doi.org/10.1016/0377-8398\(95\)00048-8](https://doi.org/10.1016/0377-8398(95)00048-8)
- Rodrigo-Gámiz, M., Rampen, S. W., Schouten, S., & Sinninghe Damsté, J. S. (2016). The impact of oxic degradation on long chain alkyl diol distributions in Arabian Sea surface sediments. *Organic Geochemistry*, 100, 1–9. <https://doi.org/10.1016/j.orggeochem.2016.07.003>
- Ruggieri, E., Herbert, T. D., Lawrence, K. T., & Lawrence, C. E. (2009). Change point method for detecting regime shifts in paleoclimatic time series: Application to  $\delta^{18}\text{O}$  time series of the Plio-Pleistocene. *Paleoceanography*, 24(1). <https://doi.org/10.1029/2007PA001568>
- Schouten, S., Hopmans, E. C., Schefuß, E., & Sinninghe Damsté, J. S. (2002). Distributional variations in marine crenarchaeotal membrane lipids: a new tool for reconstructing ancient sea water temperatures? *Earth and Planetary Science Letters*, 204(1), 265–274. [https://doi.org/10.1016/S0012-821X\(02\)00979-2](https://doi.org/10.1016/S0012-821X(02)00979-2)
- Schouten, S., Hopmans, E. C., & Damsté, J. S. S. (2004). The effect of maturity and depositional redox conditions on archaeal tetraether lipid palaeothermometry. *Organic Geochemistry*, 35(5), 567–571. <https://doi.org/10.1016/j.orggeochem.2004.01.012>
- Schouten, S., Hopmans, E. C., Van der Meer, J., Mets, A., Bard, E., Bianchi, T. S., et al. (2009). An interlaboratory study of TEX<sub>86</sub> and BIT analysis using high-performance liquid chromatography–mass spectrometry. *Geochemistry, Geophysics, Geosystems*, 10(3). <https://doi.org/10.1029/2008GC002221>
- Schouten, S., Hopmans, E. C., Pancost, R. D., & Sinninghe Damsté, J. S. (2000). Widespread occurrence of structurally diverse tetraether membrane lipids: Evidence for the ubiquitous presence of low-temperature relatives of hyperthermophiles. *Proceedings of the National Academy of Sciences*, 97(26), 14421–14426. <https://doi.org/10.1073/pnas.97.26.14421>

- Sikes, E. L., O'Leary, T., Nodder, S. D., & Volkman, J. K. (2005). Alkenone temperature records and biomarker flux at the subtropical front on the chatham rise, SW Pacific Ocean. *Deep Sea Research Part I: Oceanographic Research Papers*, 52(5), 721–748. <https://doi.org/10.1016/j.dsr.2004.12.003>
- Sinninghe Damsté, J. S. (2016). Spatial heterogeneity of sources of branched tetraethers in shelf systems: The geochemistry of tetraethers in the Berau River delta (Kalimantan, Indonesia). *Geochimica et Cosmochimica Acta*, 186, 13–31. <https://doi.org/10.1016/j.gca.2016.04.033>
- Sinninghe Damsté, J. S., Hopmans, E. C., Pancost, R. D., Schouten, S., & Geenevasen, J. A. J. (2000). Newly discovered non-isoprenoid glycerol dialkyl glycerol tetraether lipids in sediments. *Chemical Communications*, 0(17), 1683–1684. <https://doi.org/10.1039/B004517I>
- Sinninghe Damsté, J. S., Schouten, S., Hopmans, E. C., van Duin, A. C. T., & Geenevasen, J. A. J. (2002). Crenarchaeol the characteristic core glycerol dibiphytanyl glycerol tetraether membrane lipid of cosmopolitan pelagic crenarchaeota. *Journal of Lipid Research*, 43(10), 1641–1651. <https://doi.org/10.1194/jlr.M200148-JLR200>
- Sinninghe Damsté, J. S., Ossebaar, J., Abbas, B., Schouten, S., & Verschuren, D. (2009). Fluxes and distribution of tetraether lipids in an equatorial African lake: Constraints on the application of the TEX<sub>86</sub> palaeothermometer and BIT index in lacustrine settings. *Geochimica et Cosmochimica Acta*, 73(14), 4232–4249. <https://doi.org/10.1016/j.gca.2009.04.022>
- Sinninghe Damsté, J. S., Rijpstra, W. I. C., Hopmans, E. C., Weijers, J. W. H., Foesel, B. U., Overmann, J., & Dedysh, S. N. (2011). 13,16-Dimethyl Octacosanedioic Acid (iso-Diabolic Acid), a Common Membrane-Spanning Lipid of Acidobacteria Subdivisions 1 and 3. *Applied and Environmental Microbiology*, 77(12), 4147–4154. <https://doi.org/10.1128/AEM.00466-11>
- Sinninghe Damsté, J. S., Rijpstra, W. I. C., Hopmans, E. C., Foesel, B. U., Wüst, P. K., Overmann, J., et al. (2014). Ether- and Ester-Bound iso-Diabolic Acid and Other Lipids in Members of Acidobacteria Subdivision 4. *Applied and Environmental Microbiology*, 80(17), 5207–5218. <https://doi.org/10.1128/AEM.01066-14>
- Sniderman, J. M. K., Woodhead, J. D., Hellstrom, J., Jordan, G. J., Drysdale, R. N., Tyler, J. J., & Porch, N. (2016). Pliocene reversal of late Neogene aridification. *Proceedings of the National Academy of Sciences*, 113(8), 1999–2004. <https://doi.org/10.1073/pnas.1520188113>

- Spang, A., Hatzenpichler, R., Brochier-Armanet, C., Rattei, T., Tischler, P., Spieck, E., et al. (2010). Distinct gene set in two different lineages of ammonia-oxidizing archaea supports the phylum Thaumarchaeota. *Trends in Microbiology*, 18(8), 331–340. <https://doi.org/10.1016/j.tim.2010.06.003>
- Steph, S., Tiedemann, R., Groeneveld, J., Sturm, A., & Nürnberg, D. (2006). Pliocene changes in tropical east Pacific upper ocean stratification: response to tropical gateways? *Proceedings of the Ocean Drilling Program: Scientific Results*, 202, 1–51.
- Steph, S., Tiedemann, R., Prange, M., Groeneveld, J., Schulz, M., Timmermann, A., et al. (2010). Early Pliocene increase in thermohaline overturning: A precondition for the development of the modern equatorial Pacific cold tongue. *Paleoceanography*, 25(2). <https://doi.org/10.1029/2008PA001645>
- Thierstein, H. R., Geitzenauer, K. R., Molino, B., & Shackleton, N. J. (1977). Global synchronicity of late Quaternary coccolith datum levels Validation by oxygen isotopes. *Geology*, 5(7), 400–404. [https://doi.org/10.1130/0091-7613\(1977\)5<400:GSOLQC>2.0.CO;2](https://doi.org/10.1130/0091-7613(1977)5<400:GSOLQC>2.0.CO;2)
- Thunell, R., Tappa, E., Pride, C., & Kincaid, E. (1999). Sea-surface temperature anomalies associated with the 1997–1998 El Niño recorded in the oxygen isotope composition of planktonic foraminifera. *Geology*, 27(9), 843–846. [https://doi.org/10.1130/0091-7613\(1999\)027<0843:SSTAAW>2.3.CO;2](https://doi.org/10.1130/0091-7613(1999)027<0843:SSTAAW>2.3.CO;2)
- Tiedemann, R., Sarnthein, M., & Shackleton, N. J. (1994). Astronomic timescale for the Pliocene Atlantic  $\delta^{18}\text{O}$  and dust flux records of Ocean Drilling Program Site 659. *Paleoceanography*, 9(4), 619–638. <https://doi.org/10.1029/94PA00208>
- Tierney, J. E., & Tingley, M. P. (2014). A Bayesian, spatially-varying calibration model for the TEX<sub>86</sub> proxy. *Geochimica et Cosmochimica Acta*, 127(Supplement C), 83–106. <https://doi.org/10.1016/j.gca.2013.11.026>
- Tierney, J. E., & Tingley, M. P. (2015). A TEX<sub>86</sub> surface sediment database and extended Bayesian calibration. *Scientific Data*, 2, 150029. <https://doi.org/10.1038/sdata.2015.29>
- Tolar, B. B., King, G. M., & Hollibaugh, J. T. (2013). An Analysis of Thaumarchaeota Populations from the Northern Gulf of Mexico. *Frontiers in Microbiology*, 4. <https://doi.org/10.3389/fmicb.2013.00072>
- Uda, I., Sugai, A., Itoh, Y. H., & Itoh, T. (2001). Variation in molecular species of polar lipids from *Thermoplasma acidophilum* depends on growth temperature. *Lipids; Heidelberg*, 36(1), 103–5. <http://dx.doi.org.silk.library.umass.edu/10.1007/s11745-001-0914-2>

- Volkman, J. K., Eglinton, G., Corner, E. D. S., & Forsberg, T. E. V. (1980a). Long-chain alkenes and alkenones in the marine coccolithophorid *Emiliana huxleyi*. *Phytochemistry*, 19(12), 2619–2622. [https://doi.org/10.1016/S0031-9422\(00\)83930-8](https://doi.org/10.1016/S0031-9422(00)83930-8)
- Volkman, J. K., Eglinton, G., Corner, E. D. S., & Sargent, J. R. (1980b). Novel unsaturated straight-chain C<sub>37</sub>-C<sub>39</sub> methyl and ethyl ketones in marine sediments and a coccolithophore *Emiliana huxleyi*. *Physics and Chemistry of the Earth*, 12, 219–227. [https://doi.org/10.1016/0079-1946\(79\)90106-X](https://doi.org/10.1016/0079-1946(79)90106-X)
- Volkman, J. K., Barrett, S. M., Dunstan, G. A., & Jeffrey, S. W. (1992). C<sub>30</sub>–C<sub>32</sub> alkyl diols and unsaturated alcohols in microalgae of the class Eustigmatophyceae. *Organic Geochemistry*, 18(1), 131–138. [https://doi.org/10.1016/0146-6380\(92\)90150-V](https://doi.org/10.1016/0146-6380(92)90150-V)
- Volkman, J. K., Barrerr, S. M., Blackburn, S. I., & Sikes, E. L. (1995). Alkenones in *Gephyrocapsa oceanica*: Implications for studies of paleoclimate. *Geochimica et Cosmochimica Acta*, 59(3), 513–520. [https://doi.org/10.1016/0016-7037\(95\)00325-T](https://doi.org/10.1016/0016-7037(95)00325-T)
- Volkman, J. K., Barrett, S. M., & Blackburn, S. I. (1999). Eustigmatophyte microalgae are potential sources of C<sub>29</sub> sterols, C<sub>22</sub>–C<sub>28</sub> n-alcohols and C<sub>28</sub>–C<sub>32</sub> n-alkyl diols in freshwater environments. *Organic Geochemistry*, 30(5), 307–318. [https://doi.org/10.1016/S0146-6380\(99\)00009-1](https://doi.org/10.1016/S0146-6380(99)00009-1)
- Wara, M. W., Ravelo, A. C., & Delaney, M. L. (2005). Permanent El Niño-Like Conditions During the Pliocene Warm Period. *Science*, 309(5735), 758–761. <https://doi.org/10.1126/science.1112596>
- Weijers, J. W. H., Schouten, S., van den Donker, J. C., Hopmans, E. C., & Sinninghe Damsté, J. S. (2007a). Environmental controls on bacterial tetraether membrane lipid distribution in soils. *Geochimica et Cosmochimica Acta*, 71(3), 703–713. <https://doi.org/10.1016/j.gca.2006.10.003>
- Weijers, J. W. H., Schefuß, E., Schouten, S., & Damsté, J. S. S. (2007b). Coupled Thermal and Hydrological Evolution of Tropical Africa over the Last Deglaciation. *Science*, 315(5819), 1701–1704. <https://doi.org/10.1126/science.1138131>
- Weijers, J. W. H., Schouten, S., van der Linden, M., van Geel, B., & Sinninghe Damsté, J. S. (2004). Water table related variations in the abundance of intact archaeal membrane lipids in a Swedish peat bog. *FEMS Microbiology Letters*, 239(1), 51–56. <https://doi.org/10.1016/j.femsle.2004.08.012>

- Weijers, J. W. H., Schouten, S., Hopmans, E. C., Geenevasen, J. A. J., David, O. R. P., Coleman, J. M., et al. (2006). Membrane lipids of mesophilic anaerobic bacteria thriving in peats have typical archaeal traits. *Environmental Microbiology*, 8(4), 648–657. <https://doi.org/10.1111/j.1462-2920.2005.00941.x>
- Weijers, J. W. H., Schouten, S., Spaargaren, O. C., & Sinninghe Damsté, J. S. (2006). Occurrence and distribution of tetraether membrane lipids in soils: Implications for the use of the TEX<sub>86</sub> proxy and the BIT index. *Organic Geochemistry*, 37(12), 1680–1693. <https://doi.org/10.1016/j.orggeochem.2006.07.018>
- Woodard, S. C., Rosenthal, Y., Miller, K. G., Wright, J. D., Chiu, B. K., & Lawrence, K. T. (2014). Antarctic role in Northern Hemisphere glaciation. *Science*, 346(6211), 847–851. <https://doi.org/10.1126/science.1255586>
- Wuchter, C., Abbas, B., Coolen, M. J. L., Herfort, L., Van Bleijswijk, J., Timmers, P., et al. (2006). Archaeal nitrification in the ocean. *Proceedings of the National Academy of Sciences*, 103(33), 12317–12322. <https://doi.org/10.1073/pnas.0600756103>
- Wuchter, C., Schouten, S., Wakeham, S. G., & Damsté, J. S. S. (2006). Archaeal tetraether membrane lipid fluxes in the northeastern Pacific and the Arabian Sea: Implications for TEX<sub>86</sub> paleothermometry. *Paleoceanography*, 21(4). <https://doi.org/10.1029/2006PA001279>